N O T I C E

THIS DOCUMENT HAS BEEN REPRODUCED FROM
MICROFICHE. ALTHOUGH IT IS RECOGNIZED THAT
CERTAIN PORTIONS ARE ILLEGIBLE, IT IS BEING RELEASED
IN THE INTEREST OF MAKING AVAILABLE AS MUCH
INFORMATION AS POSSIBLE

The Pennsylvania State University

The Graduate School

Department of Aerospace Engineering

Application of an Airfoil Stall Flutter Computer Prediction
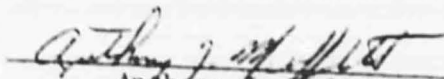Program to a Three-Dimensional Wing: Prediction vs. Experiment

A Thesis in

Aerospace Engineering

by

Anthony J. Muffoletto

Submitted in Partial Fulfillment
of the Requirements
for the Degree of

Master of Science

March 1982

Anthony O. Muffoletto

We approve the thesis of Anthony J. Muffoletto.

Date of Signature:

/6/82   *Barnes W. McCormick*

Barnes W. McCormick, Jr., Professor and Head,
Department of Aerospace Engineering, Thesis
Adviser

1-7-82   *Blaine R. Parkin*

Blaine R. Parkin, Professor of Aerospace
Engineering

1-7-82   *Joseph J. Eisenhuth*

Joseph J. Eisenhuth, Associate Professor of
Aerospace Engineering

ABSTRACT

An aerodynamic computer code, capable of predicting unsteady C_n and C_m values for an airfoil undergoing dynamic stall, is used to predict the amplitudes and frequencies of a wing undergoing torsional stall flutter. The code, developed at United Technologies Research Corporation (UTRC), is an empirical prediction method designed to yield unsteady values of normal force and moment, given the airfoil's static coefficient characteristics and the unsteady aerodynamic values, α, A and B. In this study, the aforementioned method is incorporated into a dynamics program which, when coupled with these unsteady forces and moments, is able to calculate the airfoil's aeroelastic response. Here, this aeroelastic program is applied to a three-dimensional, NACA 0012 wing. The predicted response of this wing is then compared to the response of the wing as recorded in a wind tunnel experiment.

In this experiment, conducted in the PSU 4´ x 5´ subsonic wind tunnel, the wing's elastic axis, torsional spring constant and initial angle of attack are varied, and the oscillation amplitudes and frequencies of the wing, while undergoing torsional stall flutter, are recorded ($1.0 \times 10^5 \leq Re \leq 2.5 \times 10^5$). These experimental values show only fair comparisons with the predicted responses. Predictions tend to be good at low velocities and rather poor at higher velocities.

These less-than-accurate comparisons are believed to be due to differences between ambient, aerodynamic conditions present during the collection of the UTRC program's data base and those present during the

aforementioned experiment. The major differences are between Reynold's Numbers, Mach Numbers and three-dimensional flow effects. It is believed that eliminating these differences would greatly increase the aeroelastic program's prediction accuracy. Thus, this program can be expected to yield fair predictions for any given set of ambient, aerodynamic conditions and probably much better predictions for ambient conditions which closely approximate those of the UTRC program's data base.

TABLE OF CONTENTS

List of Figures

List of Photographs

List of Tables

Nomenclature

A — Dimensionless angular velocity, $=c\dot{\alpha}/2V_\infty$

a_{o_N} — Linear normal force coefficient curve slope with respect to α

a_{o_M} — Linear moment coefficient curve slope with respect to α

AC — Dimensionless distance, in units of chord length, of airfoil aerodynamic center from airfoil leading edge

B — Dimensionless angular acceleration, $=c^2\ddot{\alpha}/4V_\infty$

C_N, C_n — Normal force coefficient for wing and airfoil, respectively, $=N/\frac{1}{2}\rho V_\infty^2 S$

C_M, C_m — Moment coefficient for wing and airfoil, respectively, $=M/\frac{1}{2}\rho V_\infty^2 Sc$

C_{n-max} — Maximum normal force coefficient

C_{m-min} — Minimum moment coefficient

C_{N_α} — Linear normal force coefficient curve slope with respect to α

C_{M_α} — Linear moment coefficient curve slope with respect to α

c — Airfoil chord length

EA — Dimensionless distance, in units of chord length, of airfoil elastic axis from airfoil leading edge

I — Airfoil moment of inertia about elastic axis

k — Reduced frequency, $=\omega c/2V_\infty$

K_T — Translational spring constant

K_Θ — Torsional spring constant

M — Moment or Mach Number

P_i, Q_i — Synthesization function coefficients for $\Delta\alpha$ and ΔC, respectively

Re — Reynold's Number, based on chord length

T — Torque or time

V_∞ — Free-stream velocity

x	Distance, from airfoil leading edge, along airfoil chord
y	Linear acceleration of point P as graphed in Figure B-1

Greek

α	Airfoil angle of attack with respect to free-stream velocity
α_{max}	Maximum angle of attack
α_{min}	Minimum angle of attack
α_i	Initial angle of attack
α_M	Mean angle of attack
α_{sd}	Airfoil dynamic-stall angle
α_{ss}	Airfoil static-stall angle
	Amplitude of torsional stall flutter oscillation
$\Delta\alpha_N, \Delta\alpha_M$	Stall delay angle of attack correction
β	Airfoil torsional displacement angle about elastic axis
β_{i-e}	Minimum torsional displacement angle to which experimental wing had to be tapped in order to excite self-sustained stall flutter
β_{i-p}	Torsional displacement angle to which computer-model wing was initially set
ζ	Damping ratio
ρ	Fluid density
ω	Frequency of torsional stall flutter oscillation, Hz
ω_n	Natural torsional frequency of airfoil, Hz

Superscript

.	Indicates time derivative of superscripted variable

ACKNOWLEDGEMENTS

CHAPTER I

INTRODUCTION

The purpose of this study is to determine the ability of a
computer code, capable of calculating unsteady normal force and moment
coefficients on an airfoil undergoing dynamic stall, to calculate the
aeroelastic response of a wing undergoing torsional stall flutter.
Airfoil stall flutter is a periodic oscillation of the airfoil, caused
by negative aerodynamic pitch damping, which may occur when an airfoil
experiences incidence angles which vary above and below its static stall
angle. This phenomenon, observed as long ago as World War I on
monoplanes, is of great concern in the helicopter and turbomachinery
industries. It often places operational limits on helicopters and
turbines by decreasing the efficiency of rotor and compressor blades
and, in extreme cases, by causing structural failure of these
components. Recently, stall flutter related problems have been
encountered on the NASA Advanced Turboprop, a thin, swept propeller
capable of cruising efficiently at high subsonic Mach Numbers (26). The
presence of such problems has created the need to predict stall flutter
onset and subsequent motion of two-dimensional airfoils and three-
dimensional wings of varied and complex geometries.

Successful methods of stall flutter prediction have, to this
date, been restricted to two-dimensional airfoils, and, in particular,
to the NACA 0012 airfoil or other airfoils of similar geometry. This
restriction is due mainly to the highly non-linear normal force and

pitching moment coefficient behavior characteristic of an airfoil experiencing dynamic stall. This characteristic does not allow for simplifying linearizing assumptions in numerical model formulations and is further complicated by the fact that a quasi-static approach is inaccurate, comparable to classical, unsteady aerodynamics.

A number of dynamic stall prediction methods have been devised and, as mentioned earlier, have met with limited success. These methods fall into two broad categories, theoretical and empirical. To date, empirical methods have given better results than theoretical ones and will continue to do so until computer capabilities and numerical methods improve enough to allow theoretical predictions to become more reliable.

The program tested in this study is an empirical one. It was incorporated into an aeroelastic code and was then used to calculate dynamic, steady-state amplitude and frequency values for a NACA 0012 wing undergoing torsional stall flutter. These predictions were then compared to experimental values obtained from wind tunnel tests done with this same wing. The ability of this program to actually predict such an aeroelastic response was then determined.

The main purpose of this paper, then, is to give the reader a detailed description and analysis of the outcome of this comparison. In addition, the reader will find a description of both the experiment and the aforementioned program in Chapters IV and III, respectively, and a detailed, but concise, overview of stall flutter and dynamic stall in Chapter II.

CHAPTER II

AIRFOIL TORSIONAL STALL FLUTTER AND DYNAMIC STALL

Stall Flutter Characteristics

Airfoil stall flutter is a predominantly torsional, dynamic, aeroelastic instability caused by negative aerodynamic pitch damping which can occur as the airfoil passes in and out of its static stall region (10). It differs from classical flutter in that classical flutter is dependent upon either elastic and/or aerodynamic mode coupling or upon a linear phase lag between the airfoil displacement and aerodynamic reaction. It differs from buffet in that the presence of buffet forces is solely dependent upon the presence of stall over part or all of the airfoil and not upon any subsequent airfoil motion (2). In contrast, the negative aerodynamic damping which causes stall flutter is a result of the non-linear, unsteady, aerodynamic reaction to airfoil motion.

One of the features peculiar to an airfoil undergoing purely torsional stall flutter[*] is that it oscillates sinusoidally in a limit cycle, that is, it oscillates according to the equation

$$\alpha = \alpha_M + \Delta\alpha \sin \omega t$$

----

[*]For the remainder of this paper, the term "stall flutter" refers to "torsional stall flutter" only, unless otherwise stated.

where α=angle of attack

α_M=mean angle of oscillation

$\Delta\alpha$=oscillation amplitude

ω=oscillation frequency.

This happens when the airfoil reaches a dynamic equilibrium
where the negative aerodynamic damping from the airstream equals the
positive structural damping of the airfoil. Thus, stall flutter can
occur at virtually any free-stream velocity, V_∞, where this condition is
met. Again, this is in contradistinction to classical flutter where,
when the flutter velocity is reached, the airfoil reacts as though being
forced at a resonant frequency.

The cause of this limit cycle motion is illustrated in Figures 1
and 2. Notice, in Figure 1, that classical, unsteady, potential C_n and
C_m values exist when the airfoil is oscillated through angles of attack
below its static stall angle, α_{ss}, and that motion along the C_m
hysteresis curve as time increases is counterclockwise. The exact shape
of these hysteresis curves is determined by variables such as reduced
frequency, k, and oscillation amplitude, $\Delta\alpha$ (2). The same holds true
for angle of attack variations which are strictly above the static stall
angle. However, Figure 2 illustrates that as the airfoil crosses the
stall angle, the hysteresis loop begins to distort even to the point of
crossing over itself. When this happens, an area is enclosed which is
surrounded by a "clockwise" C_m vs α hysteresis curve. This clockwise
area minus the counterclockwise area equals the net work being done on
the airfoil by the airstream and thus represents negative aerodynamic
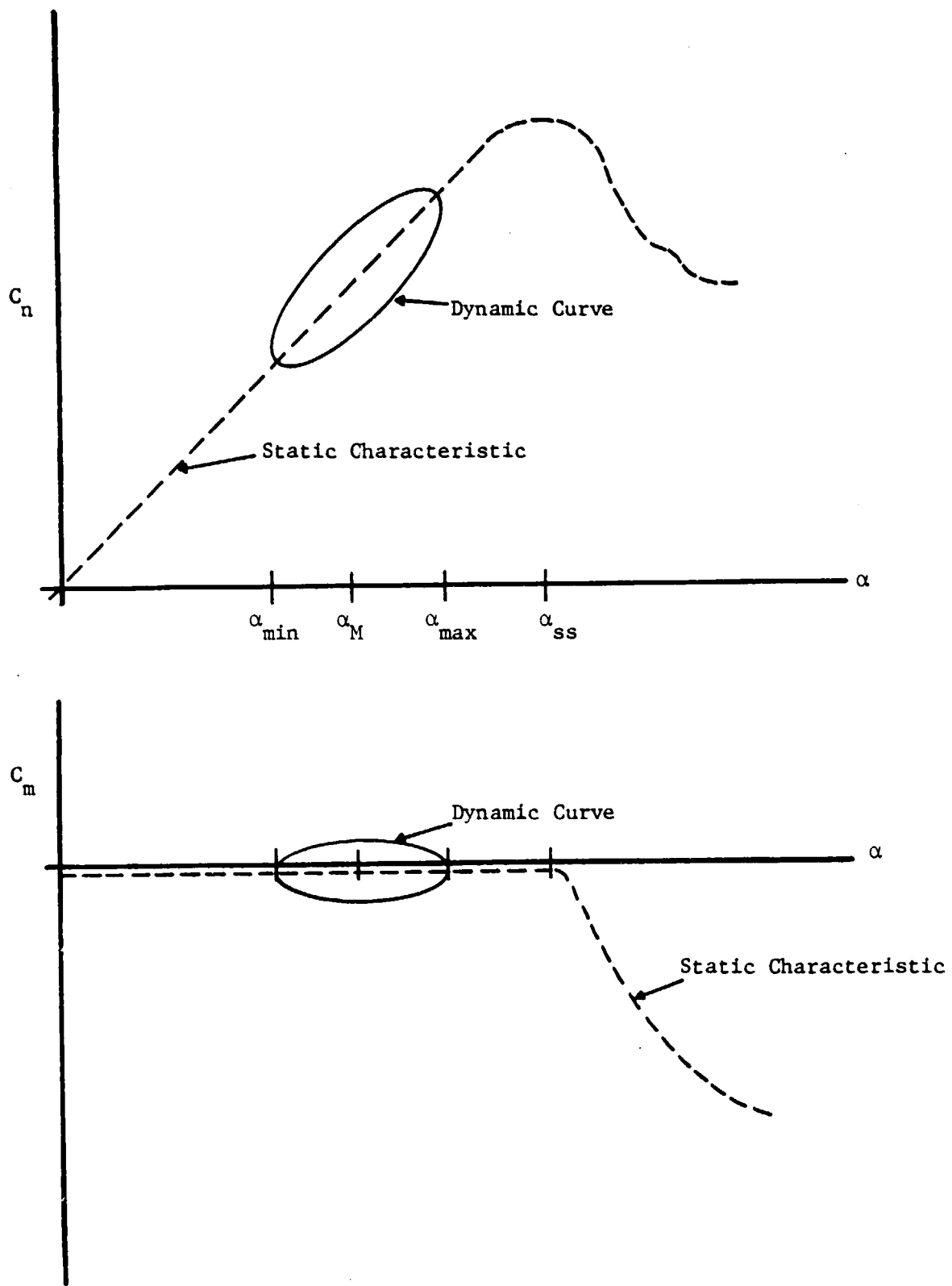
FIGURE 1: Classical, unsteady hysteresis loops for angles of attack below stall.
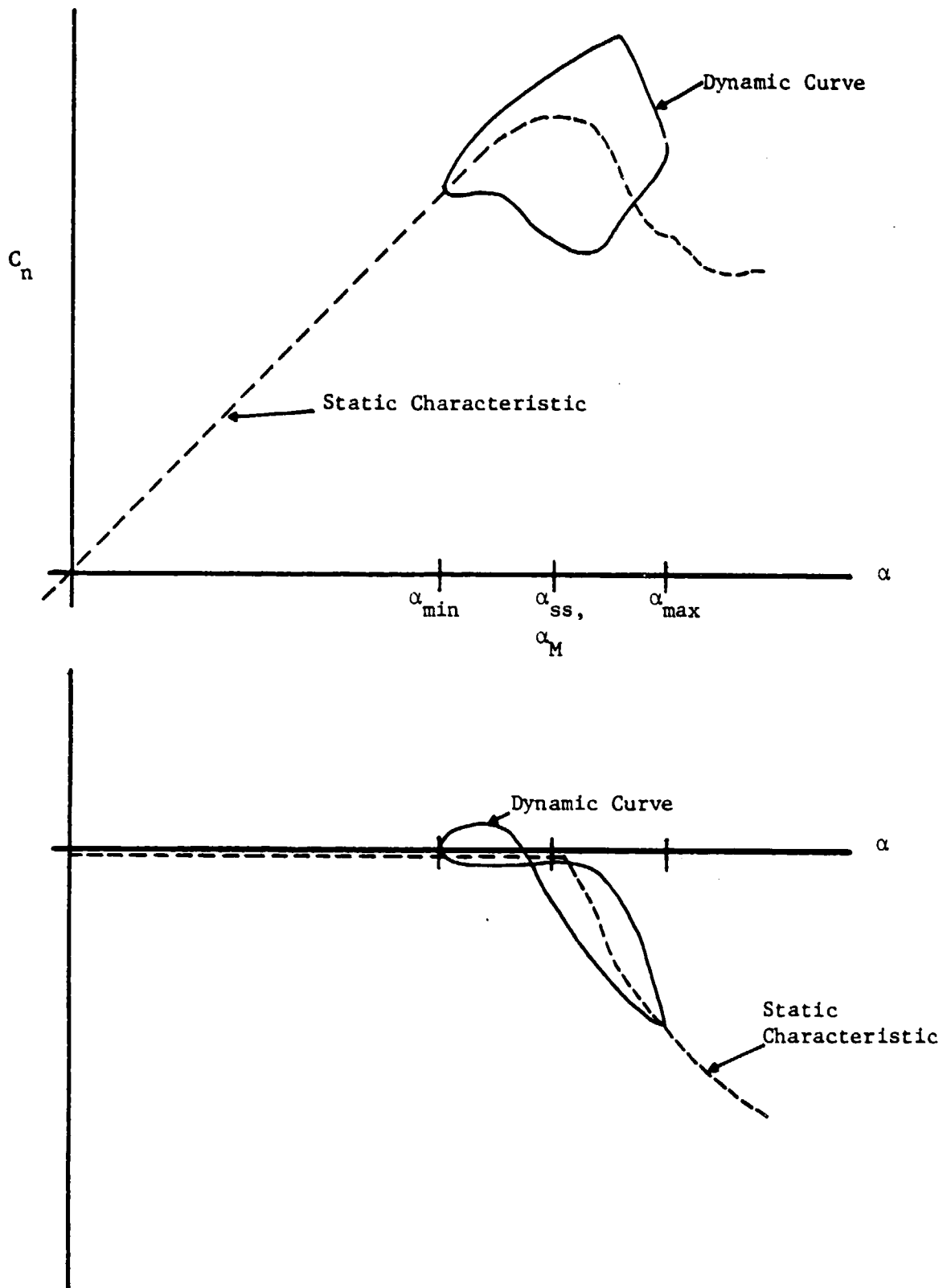
FIGURE 2: Dynamic stall hysteresis loops.

damping (6). The magnitude of this net aerodynamic damping is important
in determining the airfoil's dynamic response: the larger its value the
larger the amplitude and/or the frequency of oscillation.

It is possible for any particular airfoil to produce an infinite
number of hysteresis loop configurations. To understand why, one must
have a clear understanding of the mechanism of dynamic stall and the
factors that most affect its characteristics. This is the subject of
the following two sections.

Dynamic Stall Characteristics[*]

In this section, the major aerodynamic features of a NACA 0012
airfoil undergoing dynamic stall are first discussed in general and are
then illustrated more clearly and quantitatively in an example. All of
these features are present in varying degrees of relative importance for
almost all airfoil geometries and unsteady stalling conditions. Major
exceptions are noted in this chapter's final section.

General Characteristics

C_n and C_m phase lag $(\dot{\alpha}>0$, $\alpha<\alpha_{ss})$. This phase lag is much like
that which occurs in unsteady, classical potential airfoil theory and
has been successfully modeled that way (12).

----

[*]Information for the first subsection below is taken from references 4,
14-17, 19, 22-24, 27, 31 and 34, collectively, while that for the
second subsection is taken solely from references 4, 24 and 30.

Stall overshoot. An airfoil undergoing a positive pitch velocity will actually "overshoot" its static stall angle without stalling. That is, the boundary layer next to the airfoil surface will remain attached, and C_{n_α} and C_{m_α} will remain virtually unchanged above the stall angle.

Reattachment undershoot. This is the opposite of the stall overshoot effect. After the airfoil has gone into full dynamic stall, it often "undershoots" its static stall angle before boundary layer reattachment begins and before C_n and C_m return to unstalled values.

Flow reversal and separation. Flow reversal and boundary layer separation are not coincident on a dynamically stalling airfoil. In fact, a very large portion of an airfoil undergoing dynamic stall may experience a thin layer of flow reversal next to its surface before the boundary layer actually separates and causes gross changes in C_n and C_m values. Figure 3 illustrates the differences in boundary layer profiles between static and dynamic separation.

Vortex shedding. One of the most pronounced events occuring at, or just after, complete boundary layer separation is the shedding of a vortex which travels from the leading edge to the trailing edge of the airfoil. This vortex, which is usually shed at or very near the maximum angle of attack, is the cause for the characteristic extreme values of C_{n-max} and C_{m-min}.

TYPICAL VELOCITY PROFILE
EDGE OF BOUNDARY LAYER
SEPARATION POINT

REVERSED FLOW REGION

WAKE

a. Steady separation

EDGE OF BOUNDARY LAYER

TYPICAL VELOCITY PROFILE

REVERSED FLOW BOUNDARY

WAKE
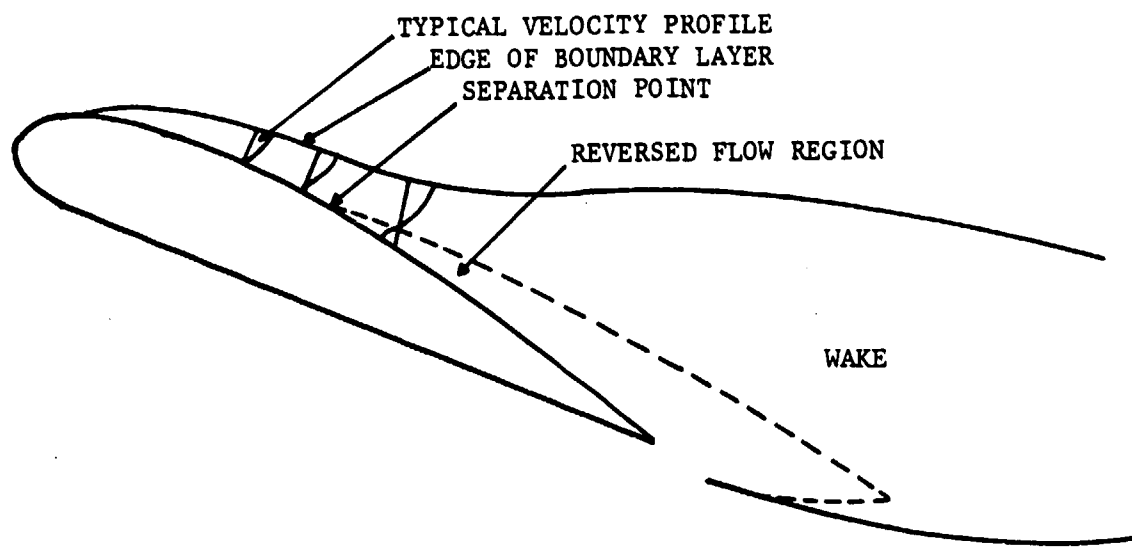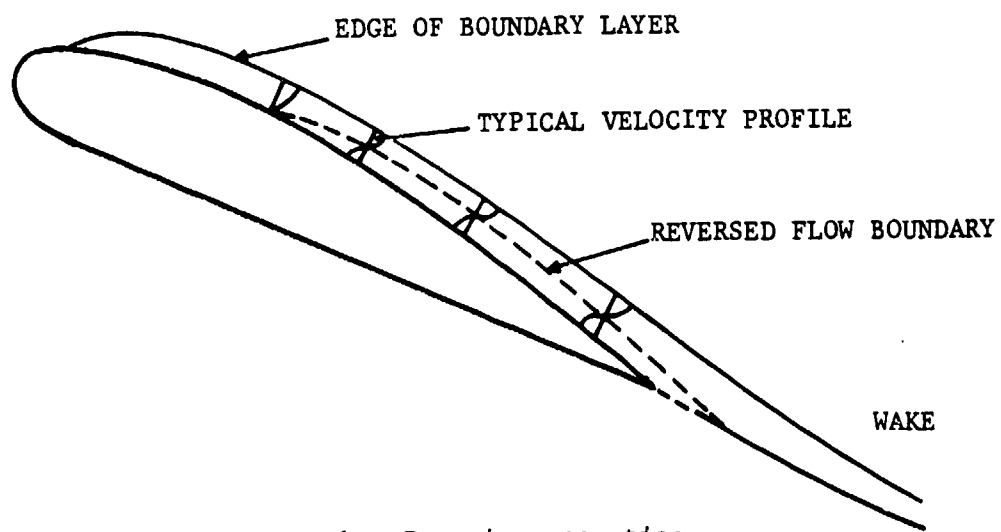
b. Dynamic separation

FIGURE 3: Boundary layer profiles for static and dynamic airfoil stall.

Separate stall events. C_m "stalls" just before C_n does, due to the effect of the shed vortex mentioned above.

Force and moment hysteresis. C_n and C_m, when graphed as a function of α, form distorted hysteresis loops (see previous section).

Typical Cycle

The following paragraphs describe a NACA 0012 airfoil undergoing sinusoidal pitch oscillations about its 1/4 chord. Pertinent data is as follows: $\alpha_{ss}=14.0^\circ$, $\alpha=15^\circ \pm 10^\circ \sin\omega t$, k=0.15, Re=2.5x10^6 and chord=4 ft.

Static stall angl: exceeded. The airfoil, pitching up, behaves as though it is still below its static stall angle. No flow reversal is present.

Flow reversal begins (Figures 4a and 4b). When the angle of attack is equal to 19 or 20 degrees, a thin layer of reversed flow appears at the trailing edge and moves up toward the leading edge. The boundary layer remains attached but is thickened and disturbed. No noticeable change in C_n or C_m occurs until the flow reversal reaches x/c=0.50.

Vortex formation. This flow reversal continues toward the leading edge until it reaches x/c=0.30 ($\alpha=23.4^\circ$), at which time the boundary layer abruptly separates all the way to the leading edge. Immediately, as shown in Figure 4c, a vortex begins to form at x/c=0.1, indicated by increased suction at this point on the airfoil, and moves downstream at approximately 35 to 40 percent of the freestream speed
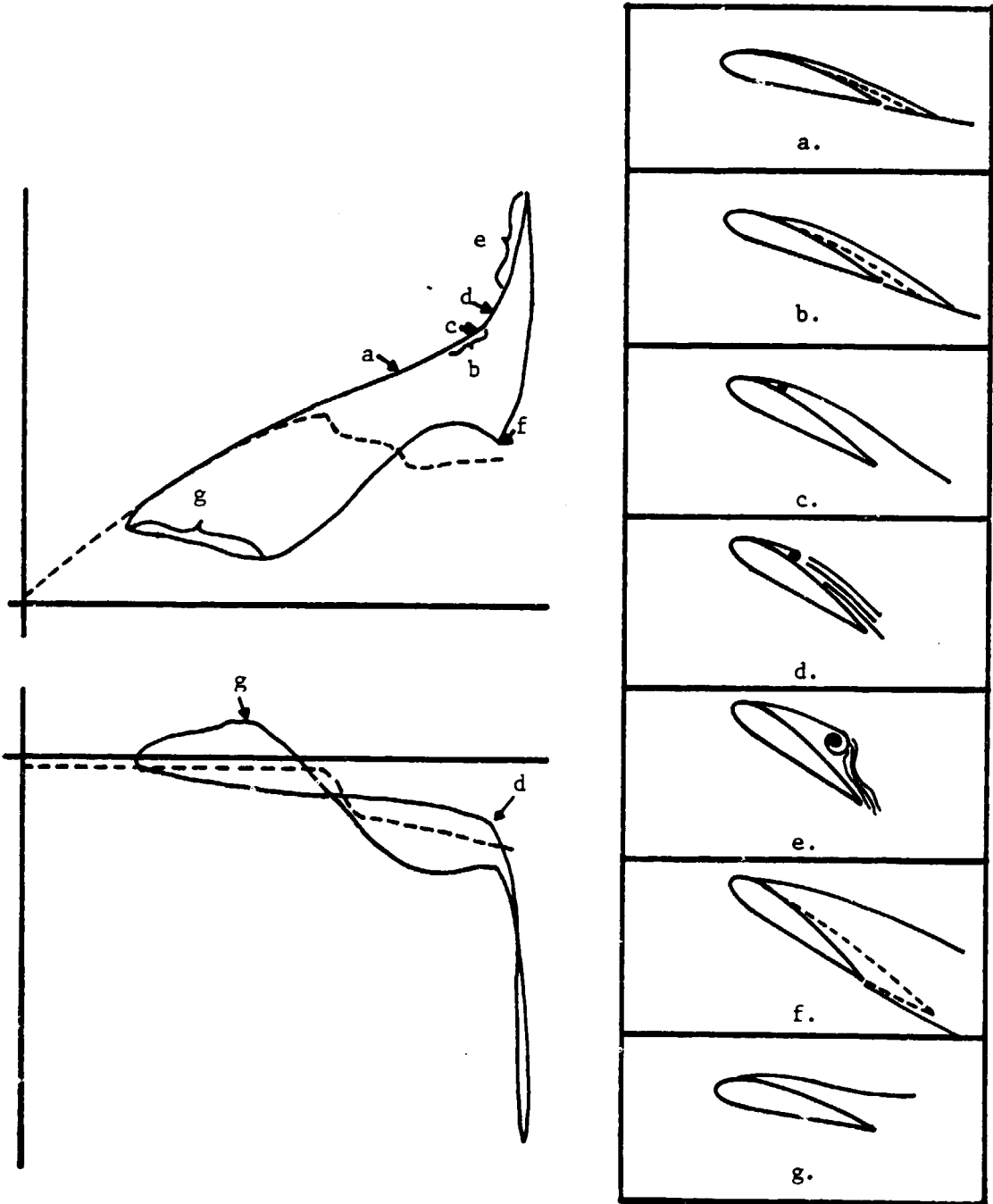
FIGURE 4: Dynamic stall events.

(Figure 4d). As this vortex travels, the magnitude of the reversed flow near the airfoil surface increases.

C_n and C_m changes. This change in velocity, and therefore pressure distribution, over the leeward side of the airfoil causes gross changes in force and moment values. For instance, the changing pressure distribution causes C_m to "stall," and vortex suction causes C_{n_α} to increase far beyond its unstalled value. C_{n-max} is reached when the vortex is at $x/c=0.50$, as shown in Figure 4e, after which C_n begins to stall. C_{m-min} is reached just before the vortex passes over the airfoil's trailing edge.

Reattachment. After the passing of the vortex, the airfoil is fully stalled (Figure 4f), i.e., the boundary layer is fully separated and C_n and C_m are in their stalled non-linear range. Clockwise C_m hysteresis is greatest at this point. Reattachment begins on the downstroke when $\alpha=16.5^o$ and progresses rearward from the leading edge at approximately 25 to 35 percent of the free-stream velocity (Figure 4g). Full reattachment does not occur until $\alpha=7.0^o$, and unstalled C_n and C_m values do not occur until $\alpha=6.0^o$ on the upstroke. The cycle is then repeated.

Factors Affecting Dynamic Stall

The above description is typical of an airfoil undergoing, what is known as, deep dynamic stall. Deep dynamic stall is roughly defined as dynamic stall in which unsteady force and moment values deviate greatly from their static counterparts. Very generally, it occurs when the maximum angle of incidence is more than just a few degrees above α_{ss} and/or when the reduced frequency is at, or above, a value of approximately 0.10. All airfoils undergoing deep dynamic stall exhibit, qualitatively, the same characteristics, which are nearly independent of airfoil shape, Reynolds Number, and type of motion. This consists of large fluctuations in C_n and C_m and a well defined and powerful, shed vortex. The other "type" of dynamic stall, known as light dynamic stall, is characterized by a relatively small deviation of unsteady force and moment values from their static counterparts but rather large hysteresis and net negative aerodynamic damping. This negative damping is usually greater than that which occurs in deep dynamic stall. Vortex activity and influence are also considerably less and static characteristics are generally much more dependent upon all of the factors listed below.

The purpose of this section is to briefly describe the major factors affecting the occurrence and relative importance of each of the aforementioned dynamic stall characteristics as they pertain to the NACA 0012 and its modifications[*].

----

[*]For details concerning more advanced airfoil sections see reference 30.

Airfoil Geometry

In the light dynamic stall region, airfoil geometry has a greater effect on dynamic stall events than any of the other factors discussed in this section. Geometrical specifications, such as leading edge radius and camber, are usually responsible for the airfoil's characteristic static boundary layer separation (eg., leading edge, trailing edge, thin airfoil etc.). The nature of the static separation greatly affects the nature of the dynamic separation and therefore, affects dynamic stall characteristics. However, once an airfoil penetrates deeply into the stall region, leading edge separation predominates, regardless of airfoil geometry.

Reduced leading edge radius. As Figure 5 demonstrates, there are almost no changes in dynamic or static stalling characteristics for this slight modification of the NACA 0012. The NACA 0012 stalls with a rather abrupt trailing edge separation.

Sharp leading edge (Figure 6). In this configuration, both static and dynamic stall begin with laminar leading edge boundary layer separation. During dynamic stall this causes flow reversal to begin earlier and more abruptly. In addition, vortex formation and movement is coincident with flow reversal incipience and spreading. In other words, they begin simultaneously at the leading edge and travel together toward the trailing edge. These differences cause significant changes in unsteady C_n and C_m curves.

0.018c

0.004c

Basic NACA 0012

C_n

—— NACA 0012
--- Reduced NACA 0012

C_m

5   15   25
α

5   15   25
α

FIGURE 5: Hysteresis loops for NACA 0012 with reduced leading edge radius
($\alpha = 10^o \sin\omega t$, k=0.15, Re=2.5x10^6).
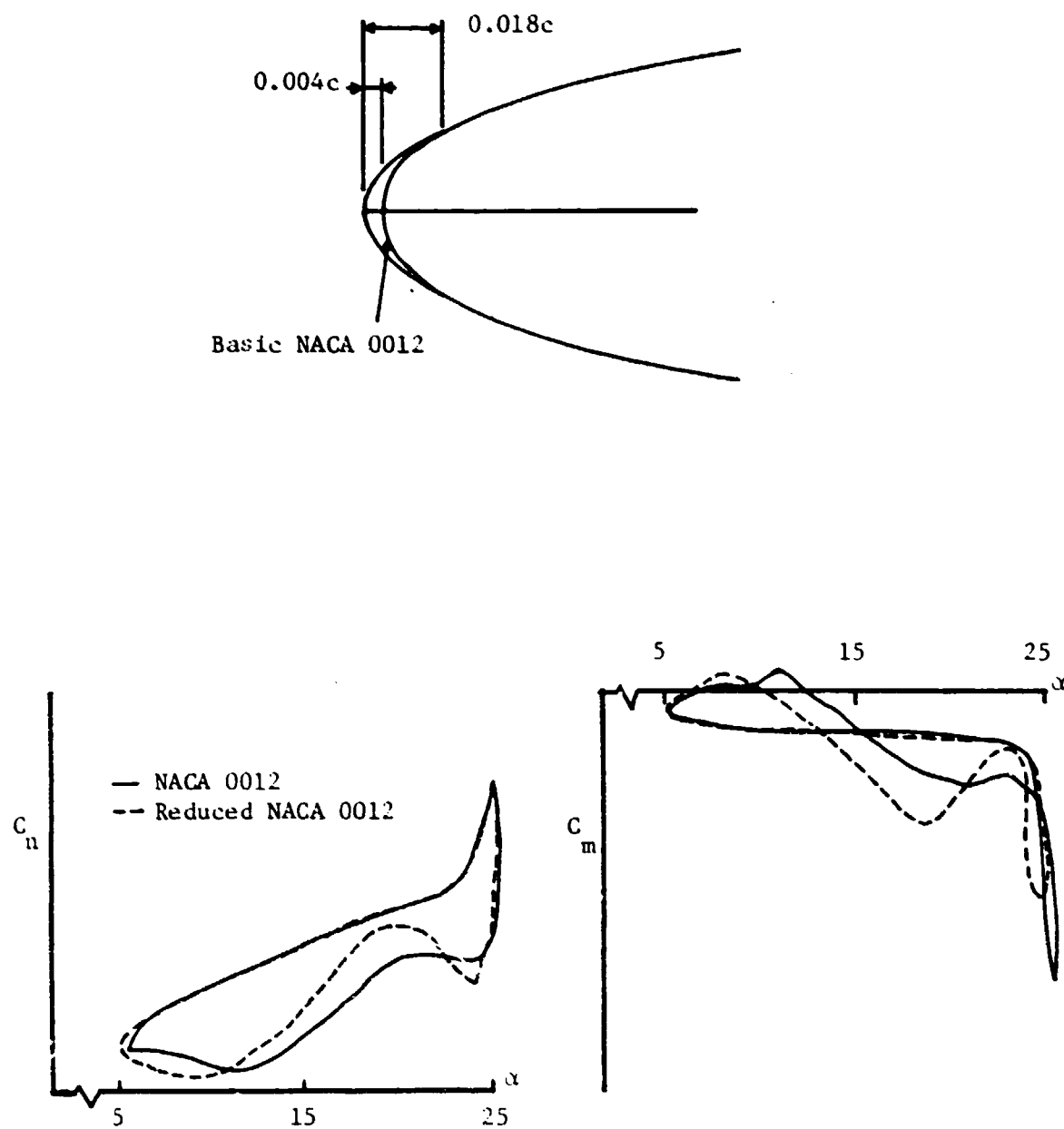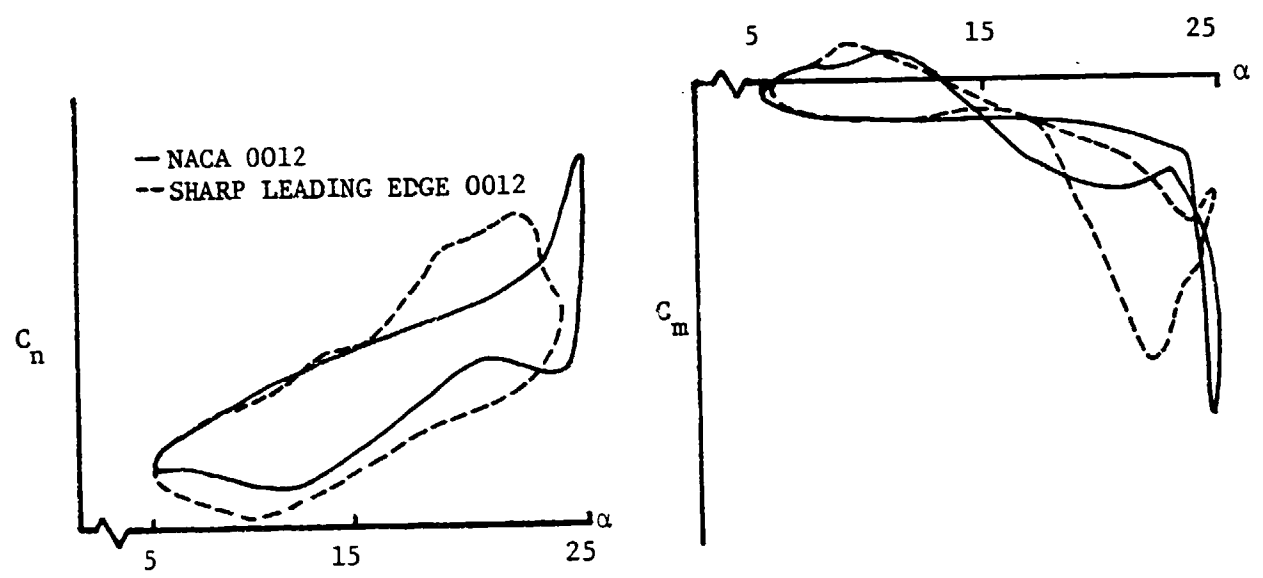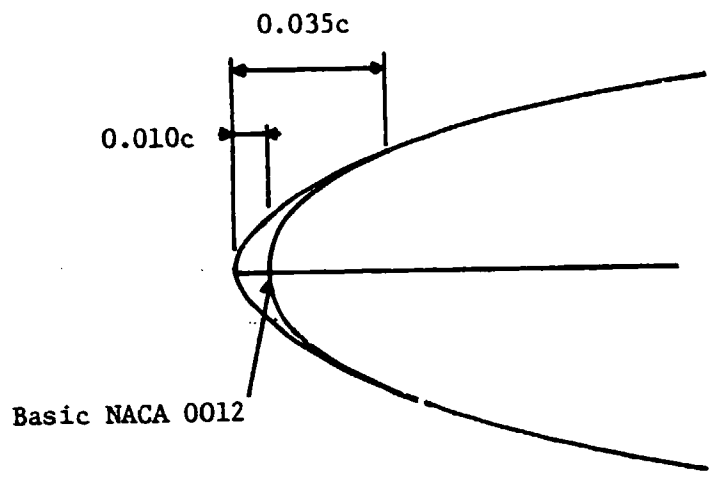
FIGURE 6: Hysteresis loops for NACA 0012 with sharp leading edge radius ($\alpha=10^\circ \sin\omega t$, $k=0.15$, $Re=2.5 \times 10^6$).

Cambered Leading Edge. Here, both static and dynamic stall remain of the trailing edge type but they become much more gradual. The shed vortex is much less powerful, and, as shown in Figure 7, this results in lower C_{n-max} and C_{m-min} values.

Reduced Frequency

Next to airfoil geometry, reduced frequency, $\omega c/2V_\infty$, has the most significant effect on dynamic stall. Generally, increases in k cause both a delay of stall events, such as flow reversal, boundary layer separation and vortex formation, and an increase in the phase angle between them. Specifically, an increase in k usually causes a delay in the occurrence of flow reversal[*]. This delay, in turn, causes separation delay and a proportionate delay in vortex shedding. A vortex which is shed later is generally more powerful due to the presence of an increased attached circulation before stall. Consequently, C_{n-max} and C_{m-min} become greater; their values can change by as much as 100 percent as k is varied from 0.004 to 0.25, where $k \leq 0.004$ is generally considered to be the quasi-static region. Figure 8 shows how these unsteady values vary with k. In addition, a similar delay in boundary layer reattachment causes larger hysteresis and, up to a point, greater net negative aerodynamic damping. As stated earlier, when conditions for deep dynamic stall are reached, net negative aerodynamic damping begins to drop off despite large C_{n-max} and C_{m-min} values. Thus, increasing k

---

[*]It has been proposed that this delay is due to the filling out of the boundary layer near the airfoil's leading edge, resulting from the positive pitch velocity (12).

0.025c

Basic NACA 0012

C_n

—NACA 0012

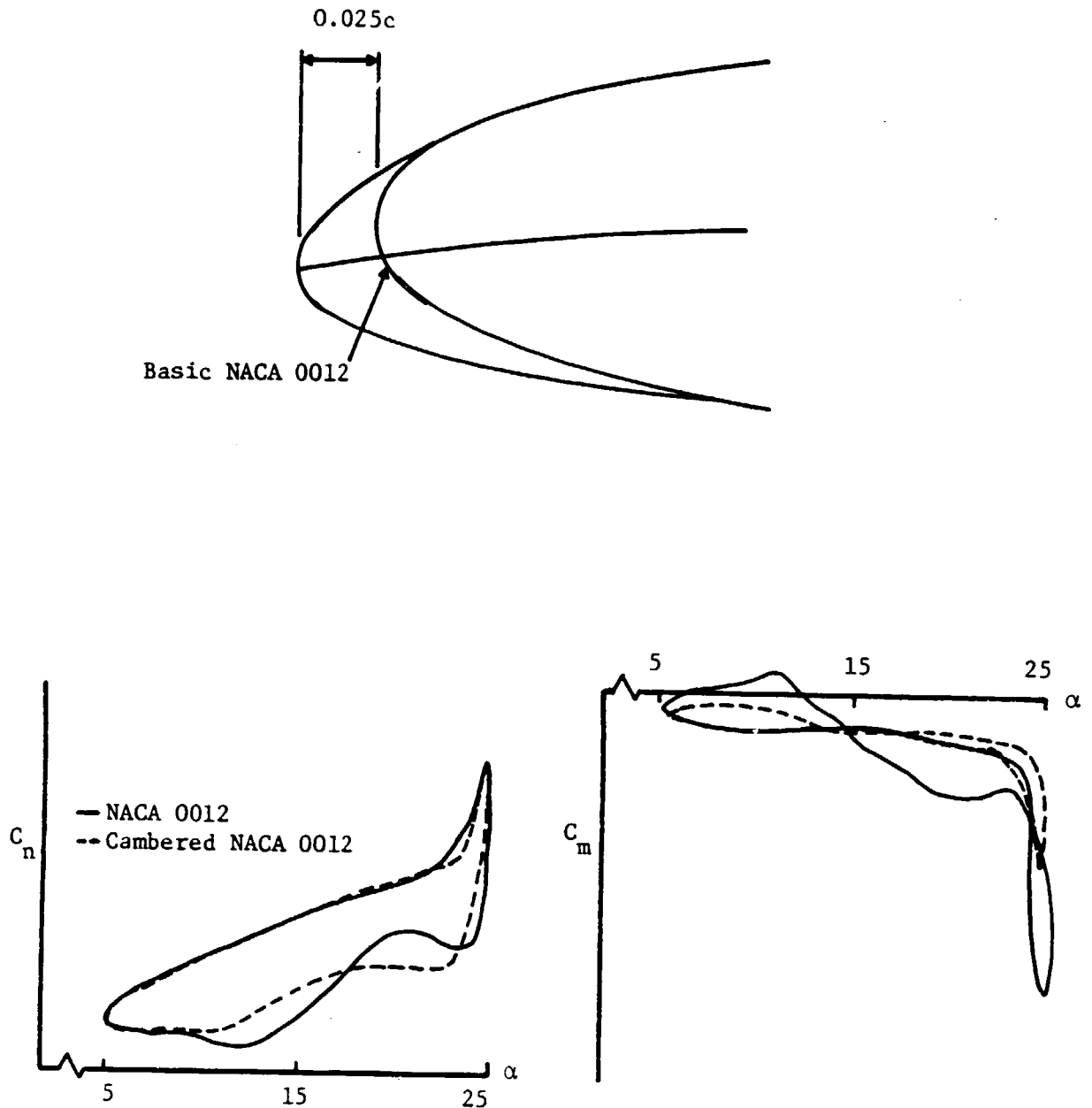-- Cambered NACA 0012

5   15   25 α

C_m

5   15   25

α

FIGURE 7: Hysteresis loops for NACA 0012 with cambered leading edge
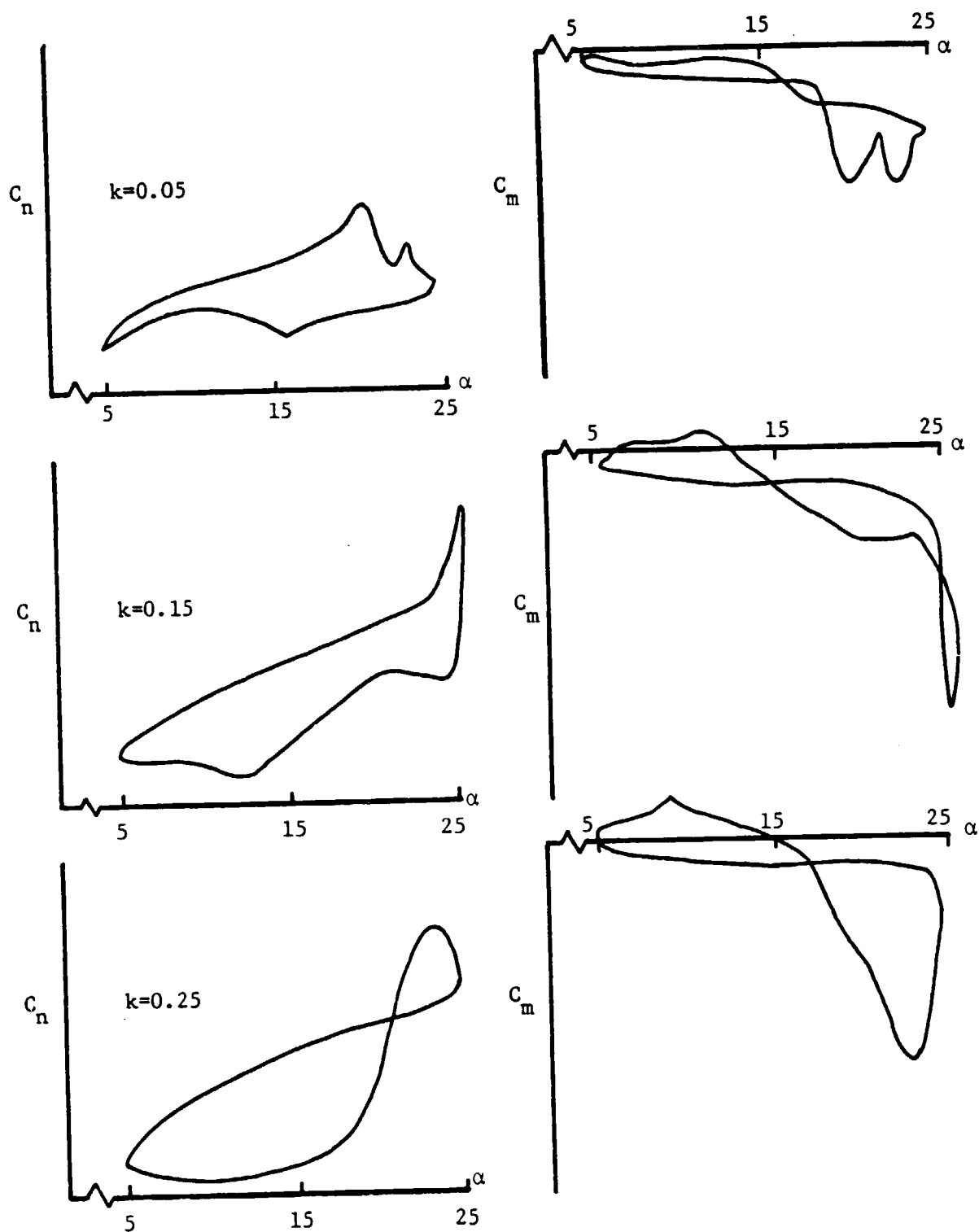($\alpha=15^{\circ}\pm10^{\circ}\sin\omega t$, k=0.15, Re=2.5x10^6).

FIGURE 8: Variation of normal force and moment coefficient values with reduced frequency for a NACA 0012 airfoil ($\alpha=15^\circ \pm 10^\circ \sin\omega t$, $Re=2.5\times10^6$).

will cause greater differences between static and dynamic stall
behavior.

Amplitude and Mean Angle

These two factors are important in that they define the
incidence angles through which the airfoil sweeps. This, in conjunction
with reduced frequency, determines whether the airfoil experiences light
or deep dynamic stall. A large α_{max} and reduced frequency will generate
a strong bound vortex, due to stall delay at high incidence angles and a
well defined and powerful shed vortex. In contrast, an α_{max} slightly
greater than α_{ss} will cause either no stall at higher values of k, as
illustrated in Figure 9, or light stall at lower values of k. Again,
amplitude and mean angle, along with reduced frequency, take on greater
importance than airfoil geometry during deep dynamic stall oscillations
due to the fact that under such conditions the boundary layer tends to
separate near the leading edge of the airfoil.

Reynolds Number and Mach Number

Reynolds Number plays a rather insignificant part in changing
dynamic stall characteristics, at least between the common test values
of 1.5×10^6 and 3.5×10^6. However, it has been found that, at higher
values of Reynolds Number, flow reversal becomes more abrupt while, at
lower values, a greater moment hysteresis results due to a delay in flow
reattachment. This can possibly cause significant increases in net
negative aerodynamic damping at very low Reynolds Numbers.
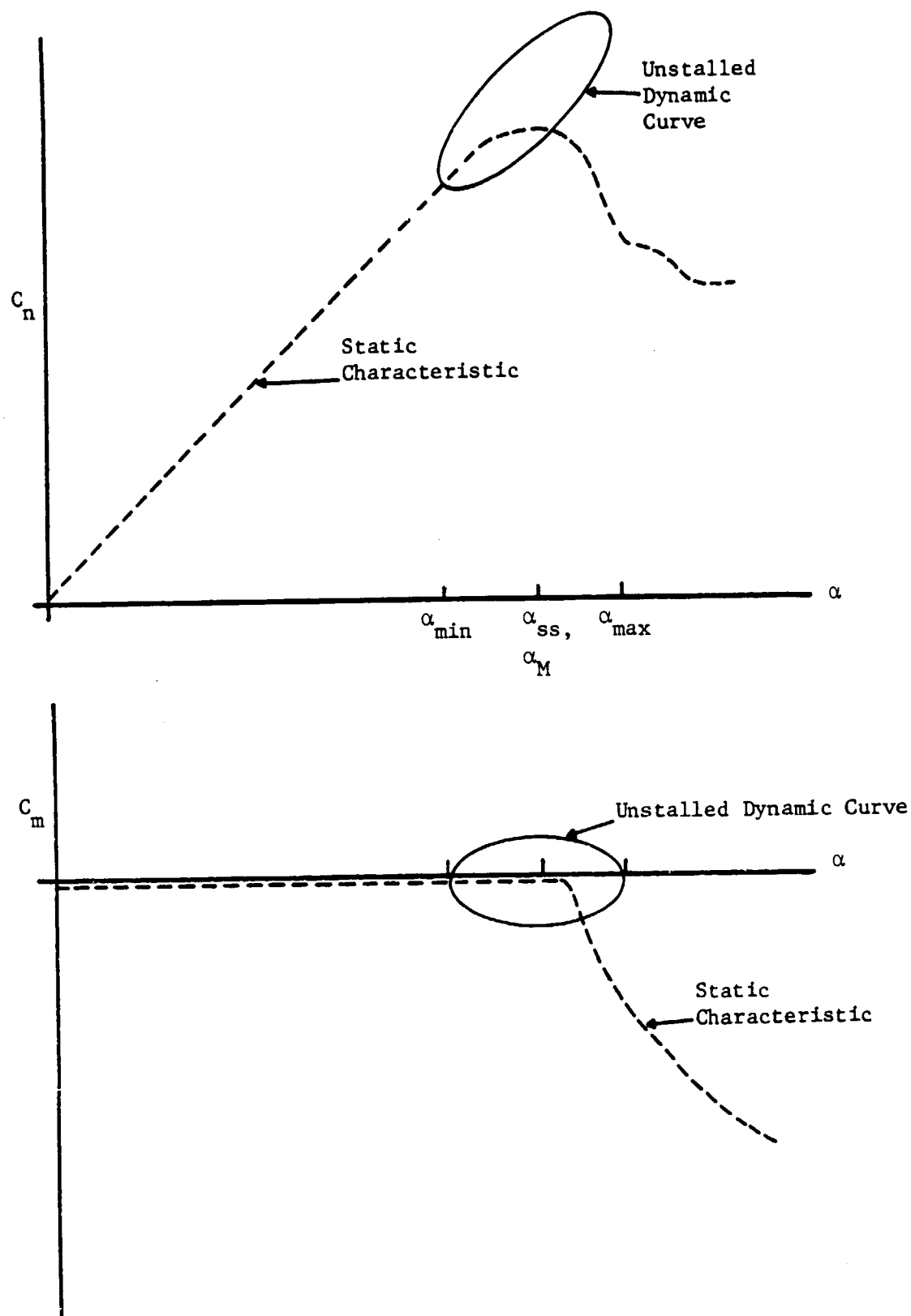
FIGURE 9: Unsteady hysteresis at high reduced frequency yielding no stall.

Mach Number generally has little or no effect on dynamic stall as long as it is kept below a value of approximately 0.2. However, above this value, but below a value of 0.6, C_{n-max} and C_{m-min} begin to decrease due to premature, shock induced separation. Above M =0.6, no overshoot of static values is seen though hysteresis still may occur. In addition, increased subsonic Mach Numbers, like deep stall conditions, cause unsteady separation to tend toward the laminar leading edge type regardless of airfoil geometry.

CHAPTER III

COMPUTER PREDICTION OF STALL FLUTTER

A program that can accurately predict unsteady C_n and C_m values for an airfoil undergoing dynamic stall, coupled with a dynamics subroutine, should be capable of doing a reliable stall flutter analysis. However, the difficulty in predicting these highly non-linear, unsteady values limits the accuracy of this type of program. Despite this difficulty, a number of programs exist which are capable of yielding fairly good results. In the sections below, the reader will find a brief description of the existing types of dynamic stall prediction methods and a detailed description of an empirical method developed at United Technologies Research Corporation (UTRC). In addition, the reader will also find a detailed description of how this UTRC dynamic stall prediction method was incorporated into the stall flutter prediction program that was used in this study for comparison with experimental data.

Theoretical Models

A detailed description of theoretical, dynamic-stall prediction programs is beyond the scope of this paper; however, their basic features, as reported in references 25 and 28, are outlined below along with a discussion of the difficulties currently being encountered in making these programs practical.

A good numerical model, short of one that solves the full non-linear Navier-Stokes Equations, should include elements of the

following: unsteady boundary layer theory, potential vortex theory and viscous-inviscid flow regime interaction. The problem with this type of approach is that the program does not "understand" the difference between unsteady flow reversal and separation and that it cannot predict the type of boundary layer separation that will occur (e.g., leading edge, trailing edge etc.). In addition, it must also be given empirical estimates of vortex incipience, strength, velocity and viscous dissipation. Add to this inaccuracies still present in complex flow-field modelling and predicted results become relatively unreliable. Probably the best way to theoretically predict dynamic stall is to solve the full Navier-Stokes Equations. Unfortunately, computers are not yet large enough or fast enough to handle this problem.

Empirical Methods[*]

Empirical programs, concerned with predicting dynamic stall, relate unsteady airfoil normal force and moment data to their static counterparts. This is usually done by using dimensionless parameters, such as $\omega c/V_\infty$, $\dot{\alpha} b/V_\infty$, $\ddot{\alpha} b^2/V_\infty^2$, coupled with empirical functions designed to take unsteady stalling characteristics into account. The data base for these types of programs is most often obtained by oscillating an airfoil sinusoidally about its 1/4 chord over a large range of values of reduced frequency, mean angle of attack and amplitude.

---

[*]For a concise overview of these methods see reference 27. Individual methods can be found in references 1, 3, 9-13, 17 and 20.

In general, such an approach has been rather successful in reproducing basic dynamic stall characteristics (eg., lift stall overshoot, loop hysteresis etc). Not only do these programs reproduce their own data base well, but they have been shown to be fairly accurate when predicting a set of independent sinusoidal data (28). This point will be discussed in greater detail later in this chapter. In addition, they are self-contained; except for static data curves, few, if any, other data need to be input into the program before execution.

However, the general applicability of an empirical method to an airfoil geometry which is different than that of the airfoil used to obtain the data base is questionable. This could be particularly important in the light stall region where airfoil geometry greatly affects stall characteristics and where, incidentally, most practical cases of stall flutter occur.

United Technologies Dynamic Stall Prediction Program

Data Base (5)

The program chosen for comparison with experimental data, in this study, is an empirical one developed at UTRC in 1975. This program uses the parameters α, A and B to calculate unsteady C_n and C_m values from their steady counterparts. The data base was collected from a NACA 0012 airfoil, having a span of 3.75 inches and a chord of 5.0 inches, in the United Aircraft Corporation's two-dimensional, high-speed, cascade wind tunnel (test section: 4" x 14" high). The airfoil was oscillated through sinusoidal, ramp and, what is called, helicopter angle of attack

variations at a free-stream Mach Number equal to 0.325 and a Reynolds Number equal to 9.6×10^5. Parrmetric variations for data collection are shown in Table I. After being collected, these unsteady C_n and C_m data were tabulated as a function of the instantaneous values of α, A and B.

Curve-Fitted Equations

In 1975 these thousands of tabulated data points were placed in a more convenient format by curve fitting them, again according to α, A and B, using a non-linear, least-squares method (1). This was done by "expanding" the static C_n and C_m (vs α) lines into the dynamic ones in the following way:

1. The linear parts of the static curves were matched to the linear parts of the dynamic curves through a horizontal and a vertical shift of the static stall point, as shown in Figure 10. The equations that affect the horizontal shift, $\Delta\alpha$, are

$$(\Delta\alpha/\alpha_{ss})_N = A(P_{N1}+P_{N5}\sigma_N)+B(P_{N2}+P_{N6}\sigma_N)$$
$$+e^{-1072.52A^2}[A(P_{N3}+P_{N7}\sigma_N)+A^2(P_{N9}+P_{N10}\sigma_N)]$$
$$+e^{-40316.42B^2}[B(P_{N4}+P_{N8}\sigma_N)].$$

and

$$(\Delta\alpha/\alpha_{ss})_M = A(P_{M1}+P_{M3}A^2+P_{M5}B^2+P_{M10}\sigma_M+P_{M7}A)$$
$$+B(P_{M2}+P_{M4}B^2+P_{M6}A^2+P_{M11}\sigma_M+P_{M8}B+P_{M9}A)$$

where $\sigma = \alpha/\alpha_{ss}$

TABLE I

TEST PROGRAM OUTLINE

Item No.	Cam Description and Angular Amplitude	Type of Coupler	Primary Drive Frequency (cps)	Mean Angle* of Attack (deg)
1	none	rigid	0 (steady state)	0,3,7,9,10, 11,12,13,14, 16,18,20,22
2	sinusoidal, ± 8	rigid	12.5,31,50,75 100	3,6,9,11,12, 14,16,18
3	sinusoidal, ± 8	rigid	120	3
4	sinusoidal, ± 8	rigid	50,75	11 (single surface meas.)
5	sinusoidal, ± 3	rigid	10,25,50,75	14
6	helicopter, ± 8	rigid	10,16.7, 33	6,11,14
7	forward ramp, #8	rigid	7.5,10,15,20	6,11,14
8	backward ramp, #8	rigid	7.5,10,15,20	6,11,14
9	sinusoidal, #8	flexible (3 springs)	7.5,10,15	6,11,16
10	none	flexible (3 springs)	0 (free vibration)	6,11,16+α for max. oscillation
11	none	flexible (3 springs)	impulsive loading, $\Delta\alpha \cong 3$	6,11,16

*Note: Each item represents test point taken at all possible combinations of frequency and angle of attack.
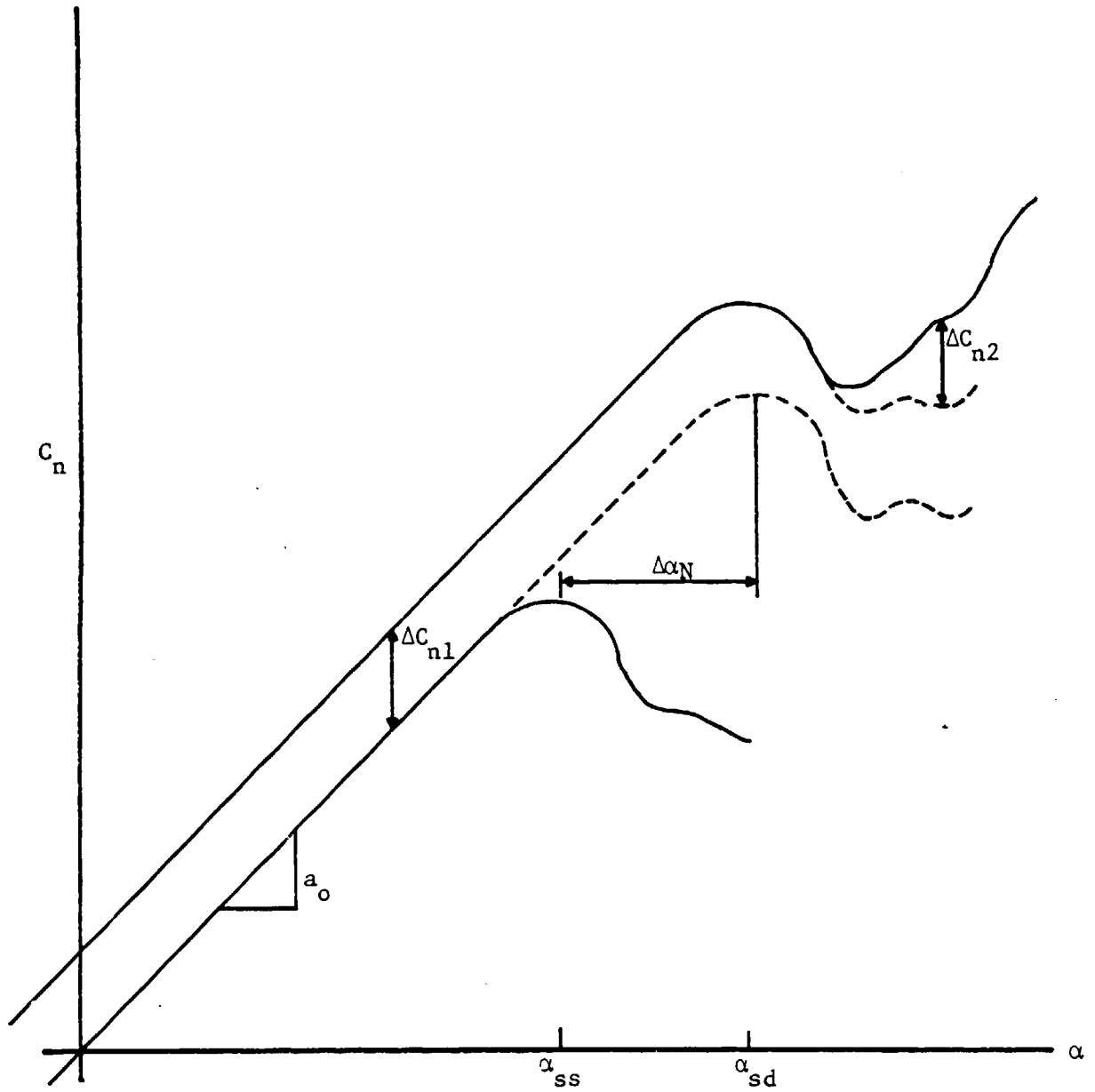
FIGURE 10: Expansion of static characteristic into dynamic characteristic for UTRC program.

i	P_{Ni}	Q_{Ni}	P_{Mi}	Q_{Mi}
		TABLE II. COEFFICIENTS for SYNTHESIZATION FUNCTION EVALUATION.		

i	P_{Ni}	Q_{Ni}	P_{Mi}	Q_{Mi}
1	-3.464003-01	1.533717+00	1.970065+01	-2.322808+00
2	-1.549076+00	6.977203+00	-6.751639+01	-1.322257+00
3	4.306330+01	1.749010+03	7.265269+02	-2.633891+00
4	-5.397529+01	1.694829+03	4.865945+04	-2.180321-01
5	5.781402+00	-1.771899+03	2.086279+04	4.580014+00
6	-3.233003+01	-3.291665+04	6.024672+03	3.125497-01
7	-2.162257+01	2.969051+00	1.446334+02	-2.828806+01
8	1.866347+01	-3.632448+01	8.586896+02	-4.396734+00
9	4.198390+01	-2.268578+03	-7.550329+02	2.565870+02
10	3.295461+02	6.601995+03	-1.021613+01	-1.204976+01
11	--	-9.654208+03	2.247664+01	-1.157802+02
12	--	8.533930+04	--	8.612138+00
13	--	-1.492624+00	--	--
14	--	1.163661+01	--	--

and where the values of P and Q are given in Table II.
The vertical shift is executed by multiplying the linear
coefficient slope by the appropriate value above.

2. Residual differences in both the linear (ΔC_1) and non-linear
(ΔC_2) range are "set to zero" with the following equations

$$\Delta C_N = A[Q_{N1} + Q_{N3} A^2 + q_N(Q_{N7} + Q_{N9} A^2 + Q_{N13} q_N) + B^2(Q_{N5} + Q_{N11} q_N)]$$

$$B[Q_{N2} + Q_{N4} A^2 + q_N(Q_{N8} + Q_{N10} A^2 + Q_{N14} q_N) + B^2(Q_{N6} + Q_{N12} q_N)].$$

and

$$C_M = A[Q_{M2} + Q_{M8}A + \sigma_M(Q_{M4} + Q_{M10}A) + \sigma_M^2(Q_{M6} + Q_{M12}A)]$$

$$+ B[Q_{M1} + Q_{M7}B + \sigma_M(Q_{M3} + Q_{M9}B) + \sigma_M^2(Q_{M5} + Q_{M11}B)].$$

3. These values are then combined into one equation to determine the final unsteady value,

$$C_{N_u}(\alpha, A, B) = C_N(\alpha - \Delta\alpha_N)_{static} + a_{o_N}\Delta\alpha_N + \Delta C_N$$

$$C_{M_u}(\alpha, A, B) = C_M(\alpha - \Delta\alpha_M)_{static} + a_{o_M}\Delta\alpha_M + \Delta C_M$$

where a_o = linear coefficient curve slope with respect to α.

4. Scaling for non-NACA 0012 airfoils and for Mach Numbers other than 0.325 is rather straightforward. Different geometries are accommodated by reading the static data (C_n and C_m vs α) for that particular airfoil into the program before execution begins. Mach Number effects are taken into account by using static data obtained at that particular Mach Number and by multiplying ΔC_n and ΔC_m by the Prandtl-Glauert Correction Factor, β, for compressible flow and by the constant 0.9457. Thus, the final equations become, with corrections,

$$C_{N_u}(\alpha, A, B, M) = C_N(\alpha, A, B, M)_{static} + a_{o_N}(M)\Delta\alpha_N + \frac{0.9457}{\sqrt{1-M^2}}\Delta C_N$$

$$C_{M_u}(\alpha, A, B, M) = C_M(\alpha, A, B, M)_{static} + a_{o_M}(M)\Delta\alpha_N + \frac{0.9457}{\sqrt{1-M^2}}\Delta C_M$$

As seen by Figures 11a through 11c, these equations do well at reproducing their own data base. Exact data points are usually not predicted but, again, basic dynamic stall characteristics are predicted.

There are definite bounds on α, A and B, defined by the data base limits, within which this program remains valid. To get a picture of how these limits are defined, imagine values of α, A and B graphed in three-dimensional space. They form an elliptic cylinder (A and B are semi-major and semi-minor axes, respectively) with irregular endplates, α. Now, instead of limiting unsteady values of A and B to those strictly defined by this ellipse, they are, instead, defined as follows:

$$(A,B) = \begin{cases} A,B & \eta \leq 1 \\ \dfrac{1}{\eta}(A,B) & \eta > 1 \end{cases}$$

$$\text{where } \eta = \sqrt{\left(\frac{A}{0.048}\right)^2 + \left(\frac{B}{0.016}\right)^2}$$

This will automatically transfer any point (A,B) outside of the ellipse to a point inside of the ellipse. Values of α are, however, restricted to their extrema: if $\sigma(\alpha/\alpha_{ss})$ becomes greater than either 1.86 or 1.839-70.33B, the program becomes invalid. This limits α to maxima and minima under various unsteady condititions.
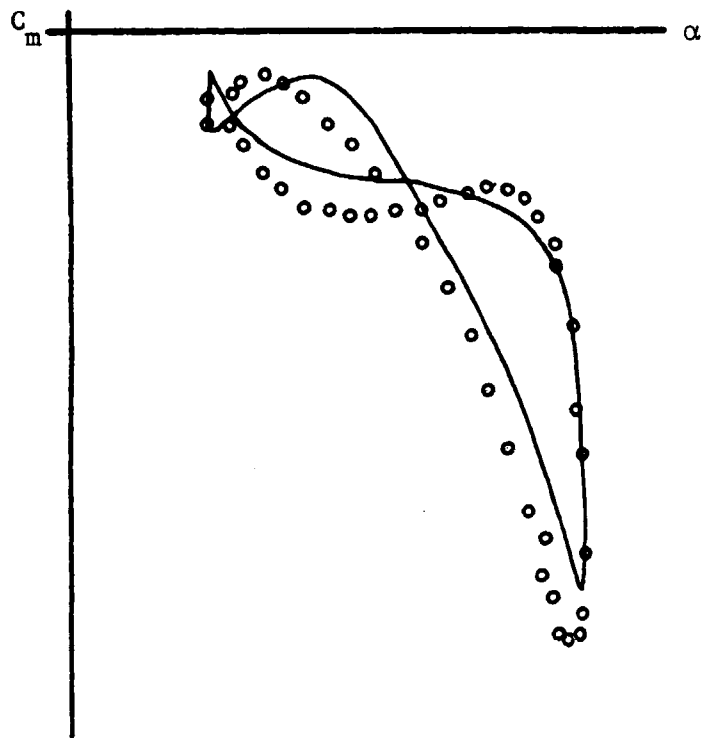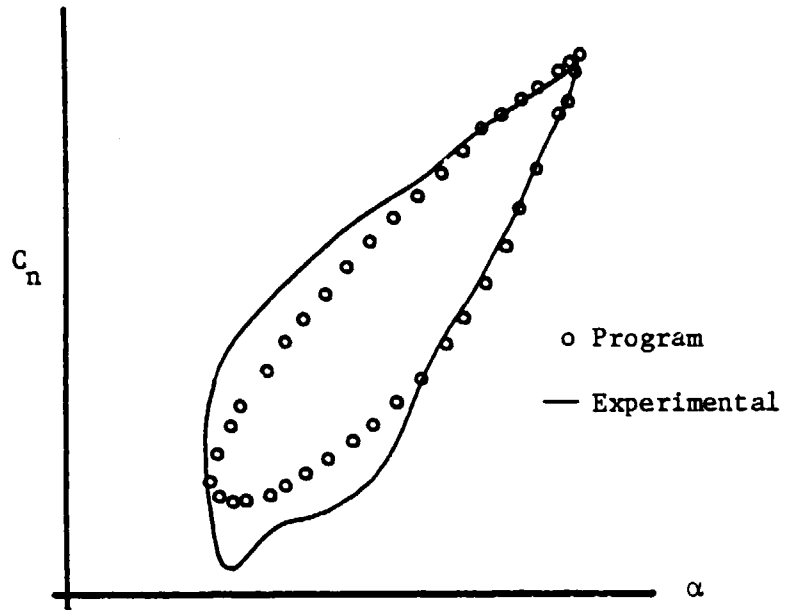
o Program

— Experimental
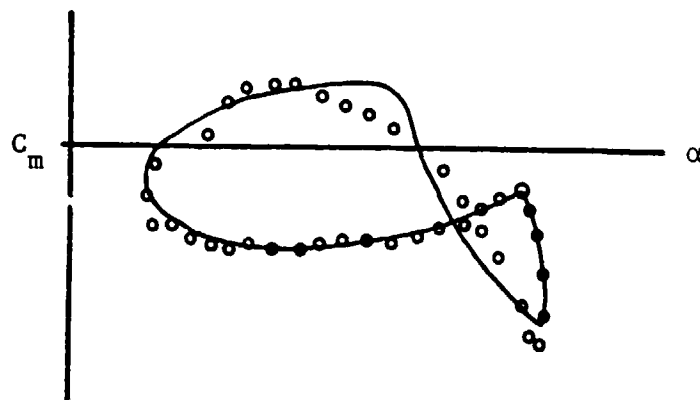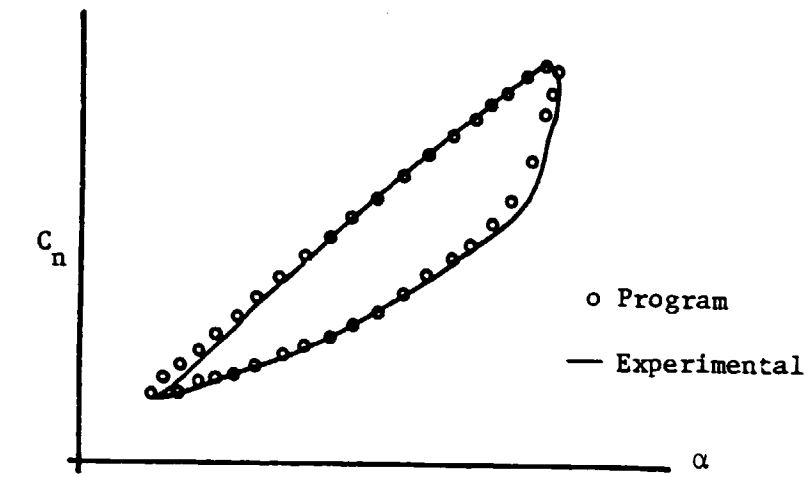
a.

FIGURE 11: Reproduction of data base by UTRC program ($\alpha_M = 11.0^o$, $\omega = 50$ Hz).

o Program

— Experimental

b.
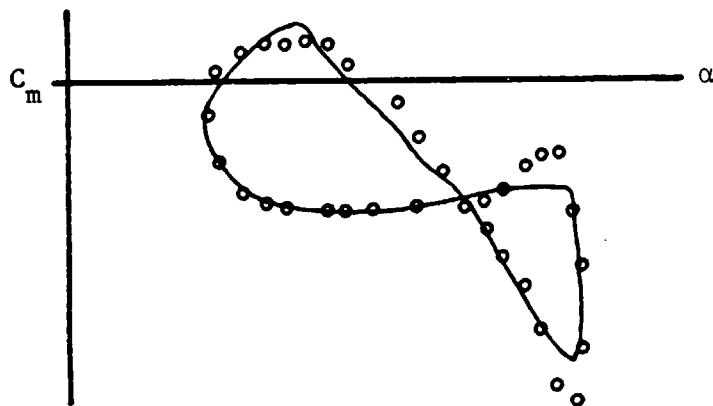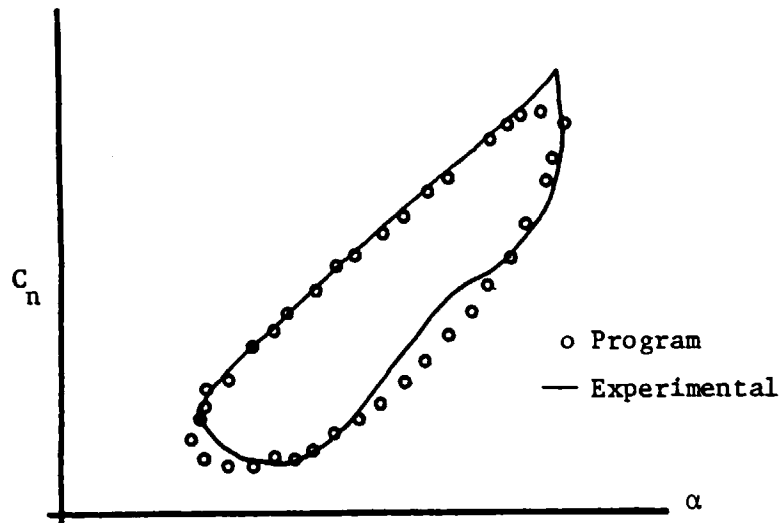
FIGURE 11(cont.): (α_M=14.0°, ω=75.17 Hz).

FIGURE 11 (cont.): ($\alpha_M = 16.0°$, $\omega = 30.99$ Hz).

Independent Evaluation of Empirical Methods

To date, there has been only one comparison between predictions obtained from empirical programs and forced sinusoidal data collected from an independent source. The outcome of this comparison is reported in references 28 and 29. This was done to check the ability of these methods to predict data from a source other than their own data base. Figures 12a and 12b, taken from reference 28, illustrate just how closely five existing empirical programs predicted values of C_{n-max} and C_{m-min}, which were taken from an independent set of NACA 0012, dynamic-stall data. Results from this comparison showed fairly good agreement for all methods tested. Notice that the UTRC program showed consistently low predictions of both C_{n-max} and C_{m-min}. This may be due to the relatively high Mach Number at which the UTRC data base was collected. Shock-induced stall may well have caused early separation and, consequently, smaller extreme values for C_n and C_m as explained in Chapter II.

Airfoil Aeroelastic Response

With a means available for calculating unsteady, non-linear normal force and moment values, the next step is to incorporate these into a dynamics program to predict the total aeroelastic response. A program with this capability has been run on the PSU IBM 370/3033 interactive computer system[*]. Details as to how this has been done are

----

[*]Copies of the program listing are available upon request.
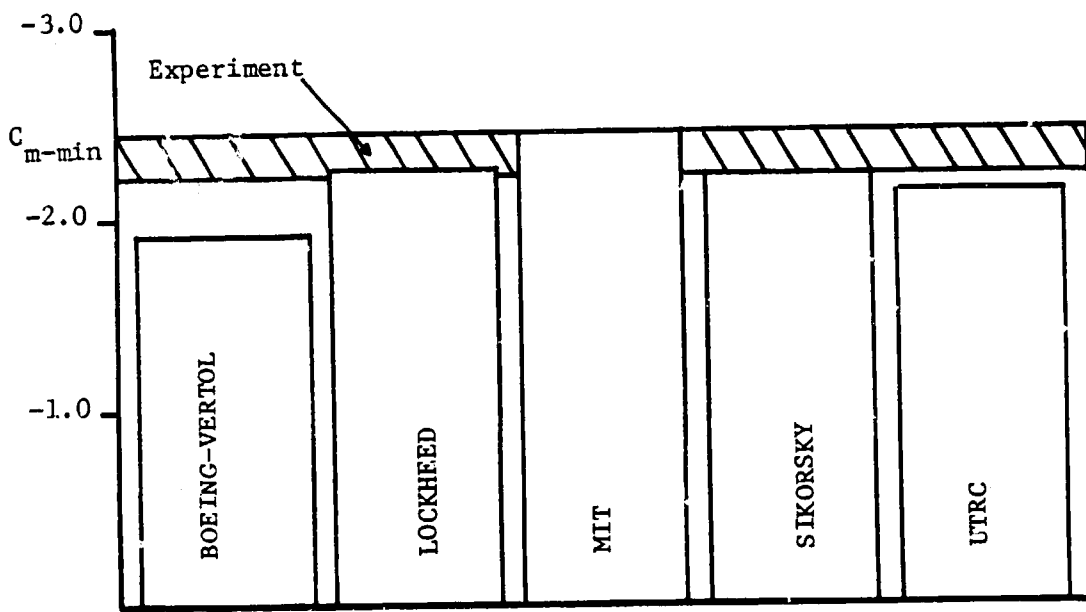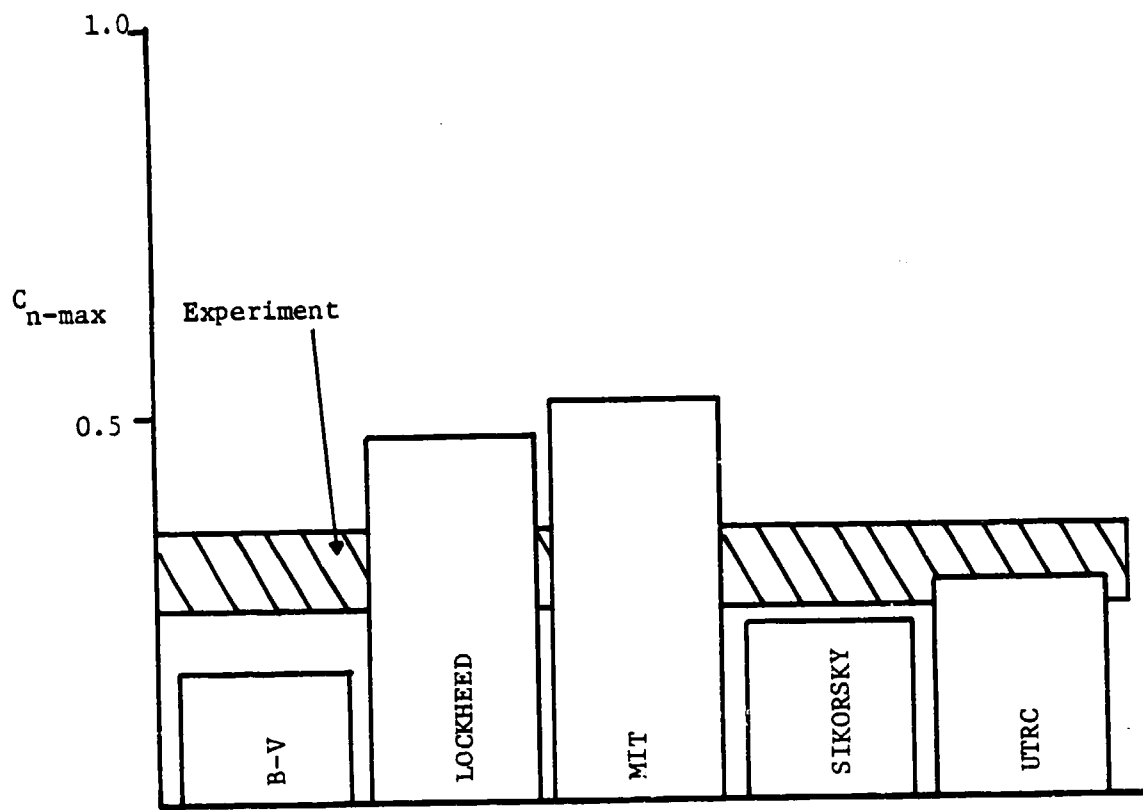
FIGURE 12: Comparison between empirical program predictions and independent data base. ($\alpha = 15^{\circ} \pm 6^{\circ} \sin \omega t$, k=0.15, Re=2.5x10^6).
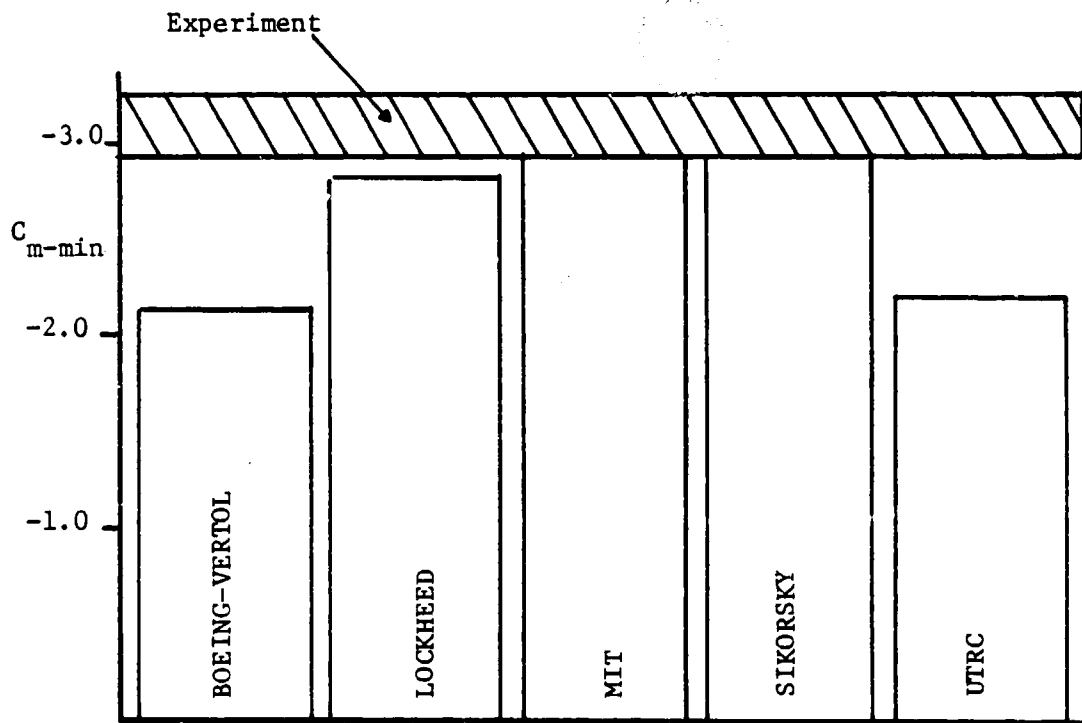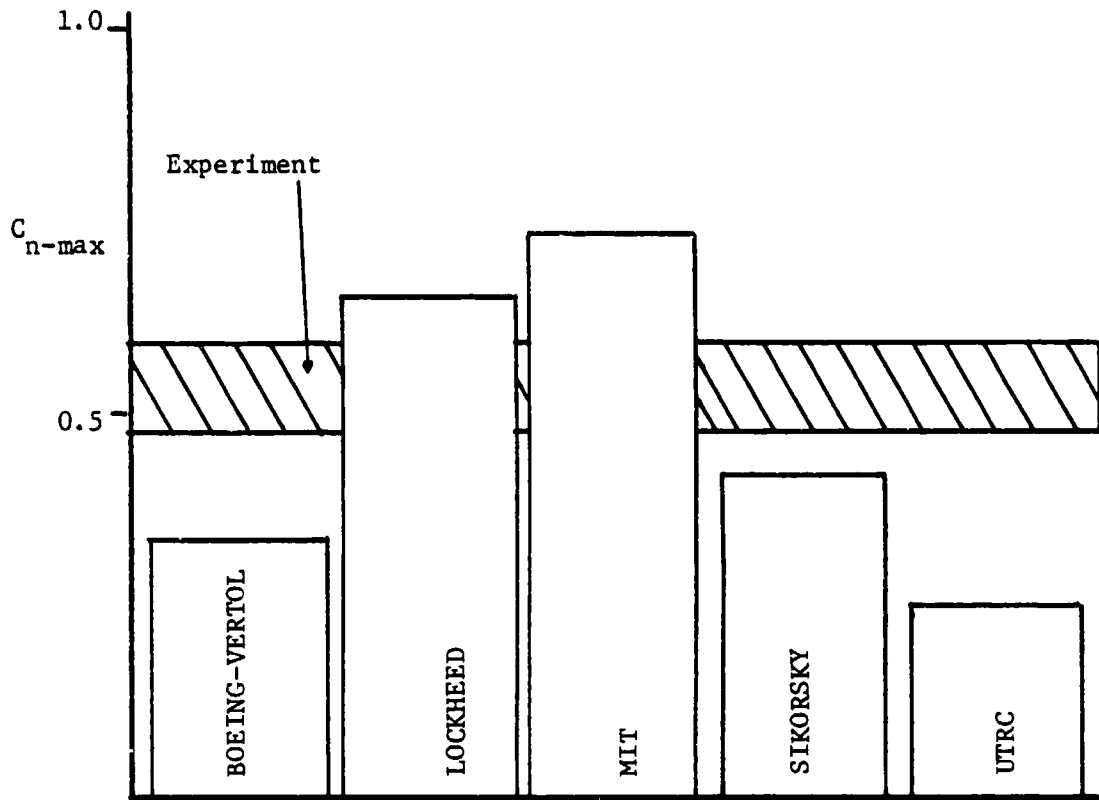
FIGURE 12 (cont.): $(\alpha=15^{\circ}\pm10^{\circ}\sin\omega t,\ k=0.15,\ Re=2.5\times10^{6})$.

given below.

An airfoil is placed in a free-stream velocity with initial conditions on the torsional displacement angle, β, and angular velocity, $\dot{\beta}$, specified, as shown in Figure 13. Unsteady coefficient values are computed by the UTRC program, assuming initial values for α, A and B, and are used to "drive" the airfoil dynamics. The motion of an airfoil undergoing single-degree-of-freedom torsional oscillations is described by the equation

$$I\ddot{\beta} + 2\zeta\omega_n I\dot{\beta} + K_\theta\beta = (C_M + (EA-AC)C_L) \times 0.5\rho V_\infty^2 Sc,$$

where   I=moment of inertia of the wing about its elastic axis

ζ=damping ratio

ω_n=natural frequency of the wing

and where other variable definitions are given in Figure 13. Specifically, this non-homogenous, second-order differential equation is solved by the fourth-order Runge Kutta method over a short time interval, during which the unsteady coefficients are assumed to remain constant (18). This solution yields new "initial conditions" for the unsteady parameters, and these are used to calculate updated values of C_n and C_m. These updated values again drive the dynamics, and the cycle is repeated until dynamic equilibrium is reached. Figure 14 shows the flow diagram for this program.
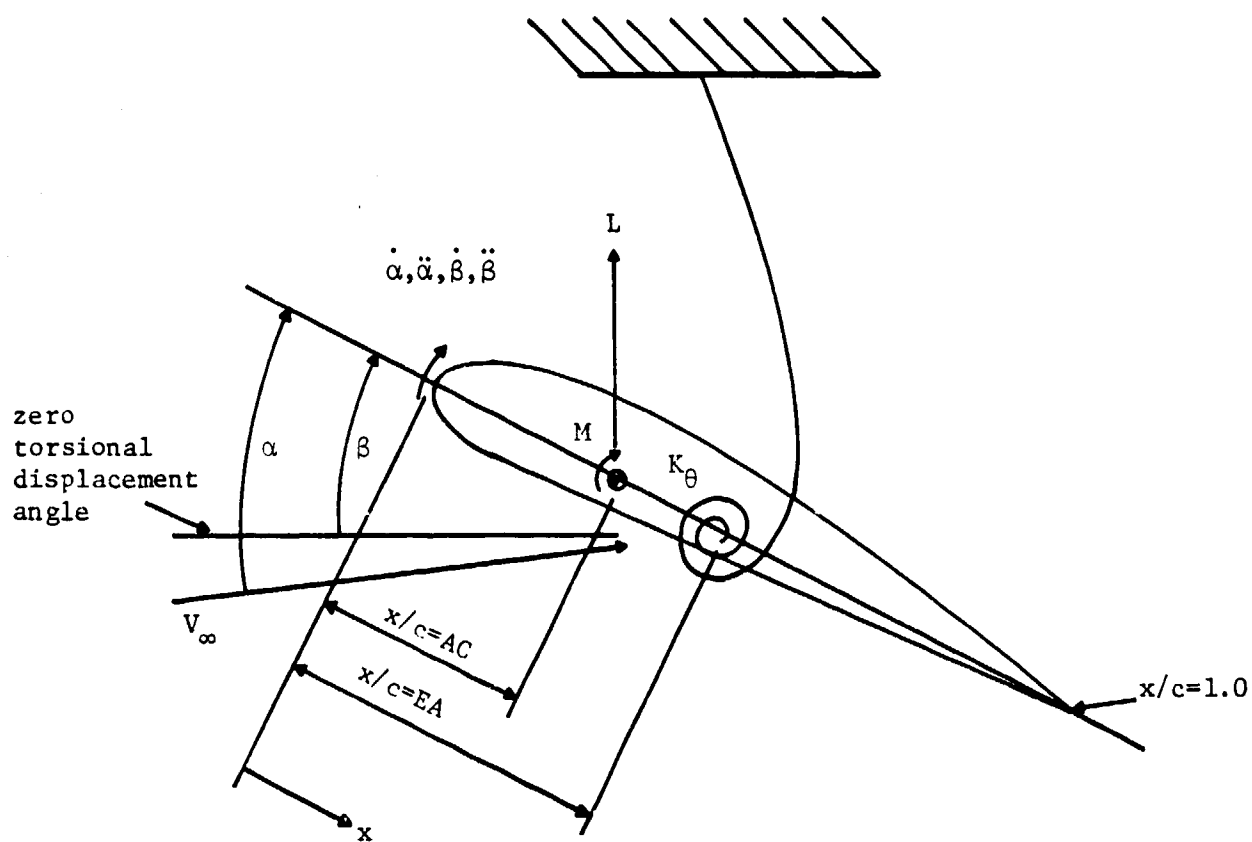
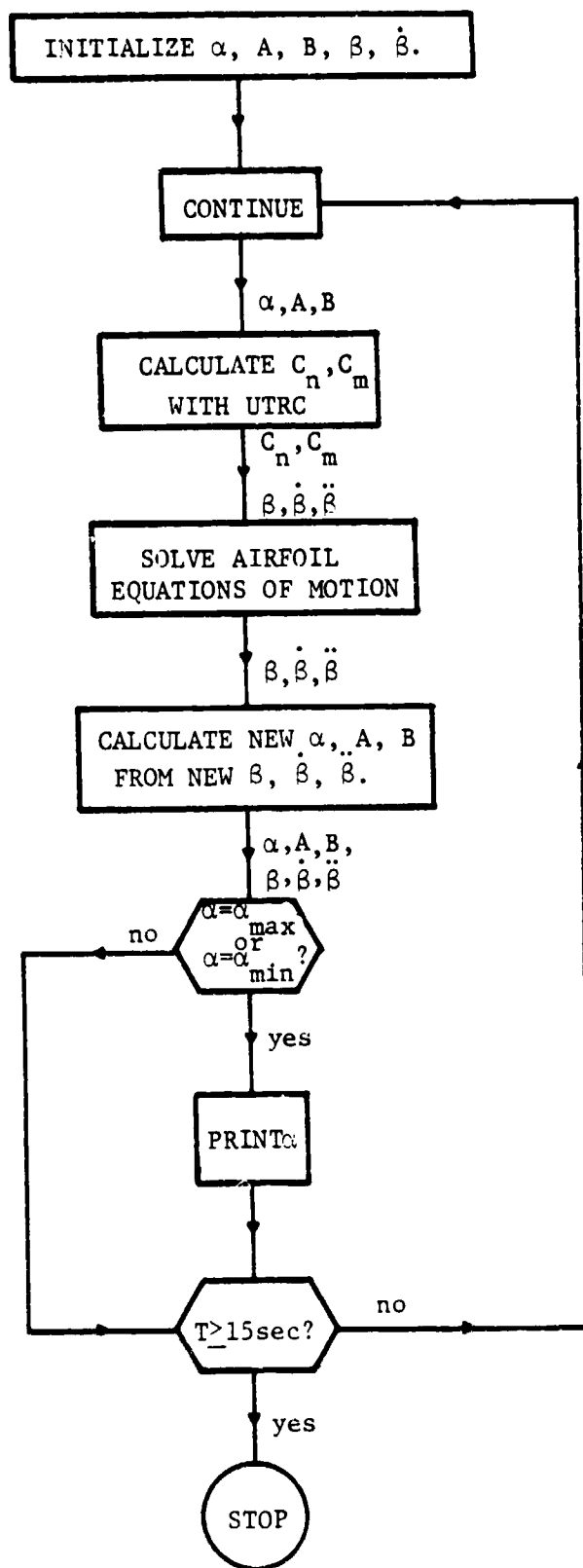FIGURE 13: Definition of aeroelastic variables.

FIGURE 14: Flow diagram for aeroelastic program.

CHAPTER IV

STALL FLUTTER EXPERIMENT

The purpose of the experiment described in this chapter was to collect dynamic data (amplitude and frequency vs. velocity) for a NACA 0012 wing section undergoing torsional stall flutter. This experimental data was used as a standard with which to compare data predicted by the aeroelastic program described in Chapter III. Results of the comparison are given in the next chapter.

Apparatus

This experiment was conducted in the PSU 4´ x 5´ subsonic wind tunnel, a closed circuit, atmospheric tunnel capable of a maximum velocity of approximately 140 ft/sec. The wing model was a hand-crafted rectangular, unswept NACA 0012 made of solid Phillipine Mohogany, coated with about 15 layers of lacquer. It had an aspect ratio of 5.3 and a chord length of 4.5 inches. Circular endplates, 1 foot in diameter and made of 1/8" plexiglass, were attached to the wing tips.

Static data for the wing, which was measured with a pyramidal balance placed below the tunnel test section, was taken with the endplates, aluminum support bars and accelerometer connected (see next section), since these attachments all rotated with the wing during flutter. This data, shown in Figures 15 and 16, is uncorrected for solid blocking, wake blocking or streamline curvature (32). It was left in this "raw" form for two reasons: first, these effects were estimated to be rather small, due to the relatively small size of the wing as
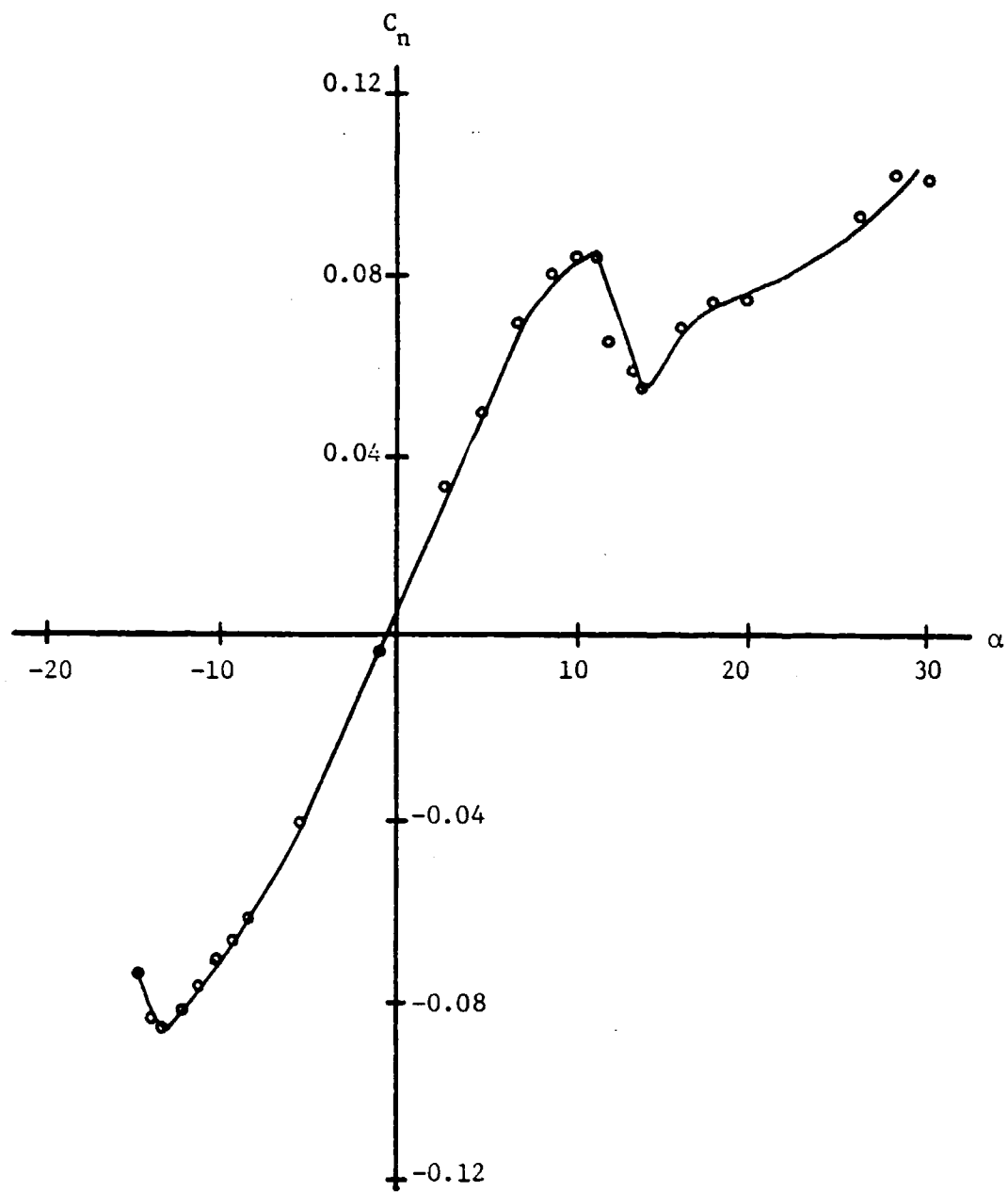
-41-

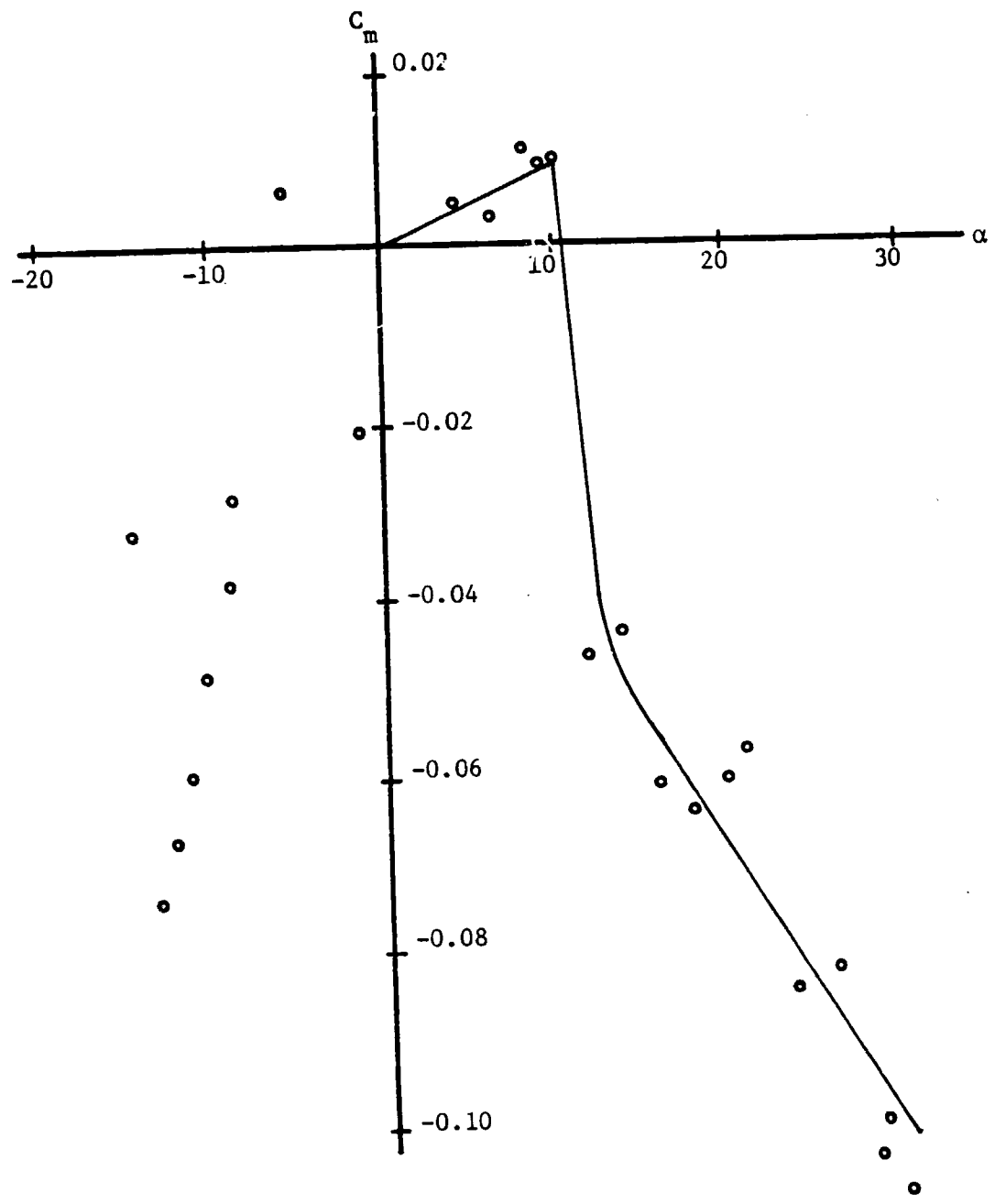FIGURE 15: Normal force characteristic line for PSU 0012 wing.

FIGURE 16: Moment characteristic line for PSU 0012 wing pivoted at the 1/4 chord.

compared to the test section, and second, the dynamic data was taken in the same tunnel where the same effects would be present. Drag interference was corrected, to a first order approximation, by taking measurements on the static-measurement-support bar without the wing attached and subtracting these values from those obtained with the wing attached.

The basic shapes of these static curves are like those of a NACA 0012 except that the stall angle is slightly below 11.0 degrees. This is most likely a Reynolds Number effect (2.5×10^5). Notice the abrupt stall of the lift curve, characteristic of a 0012. Tuft visualization verifies that this stall is of the abrupt, trailing edge type, again characteristic of the 0012. Finally, the lift curve slope, approximately equal to 0.0914/degree, is a reasonable value for this geometry, but the value of C_L at zero angle of attack of 0.015 should, of course, equal zero for a symmetrical wing. This discrepancy, in addition to the stray points and positive C_{M_α}, evident on the moment curve, is probably due to a combination of aluminum support bar and accelerometer contributions and inaccuracy in the airfoil construction[*].

The frame used to hold the wing was made of 1/8" x 1 1/4" flat steel bars, welded together in a rectangular-box configuration (see

----

[*]A repeat of the static tests verified the data shown in Figures 15 and 16. However, it should be noted that while general features, such as stall angle and general curve shape, were repeated in the re-testing, specific data points were rarely repeated. In addition, the updated static C_L characteristics consistently yielded a slope above 0.1/degree, a value greater than a NACA 0012 airfoil section. This should never occur for a three-dimensional wing. The reason for this large lift curve slope is unknown.

Photograph 1). It had an overall height of 20.5" a "span" (perpendicular to the wind velocity) of 27.0" and a "chord" of 10.0". A hinged wooden bar, connected to the tunnel floor and downstream legs of the frame, enabled it to rotate to varying angles of attack. It was "locked out" at these different angles in the following way: two threaded rods, bolted to the tunnel floor, "pierced" the "eyes" of two eyebolts which were attached to the frame's forward legs. These eyebolts were then held into position with two opposing nuts mounted on each rod. The wing and endplates were attached to the frame, approximately 15.0" above the tunnel floor, via two 16.0" aluminum bars and six 1 1/2" wood screws.

The torsional restoring spring consisted of between 2 and 8 translational linear springs[*]. They were 1 1/2" long and were attached to the frame and the aluminum bars approximately 7.5" from the wing's center of rotation. The elastic axis was varied, then, by positioning the wing such that the midpoint of the aluminum support bar was adjacent to the desired elastic axis. Finally, an electromagnet was hung from the top chord-beam on the frame's far side. It was used to prevent the wing from oscillating until the tunnel wind could be brought up to the desired speed.

---

[*]See Appendix A for calculation of torsional spring constants.
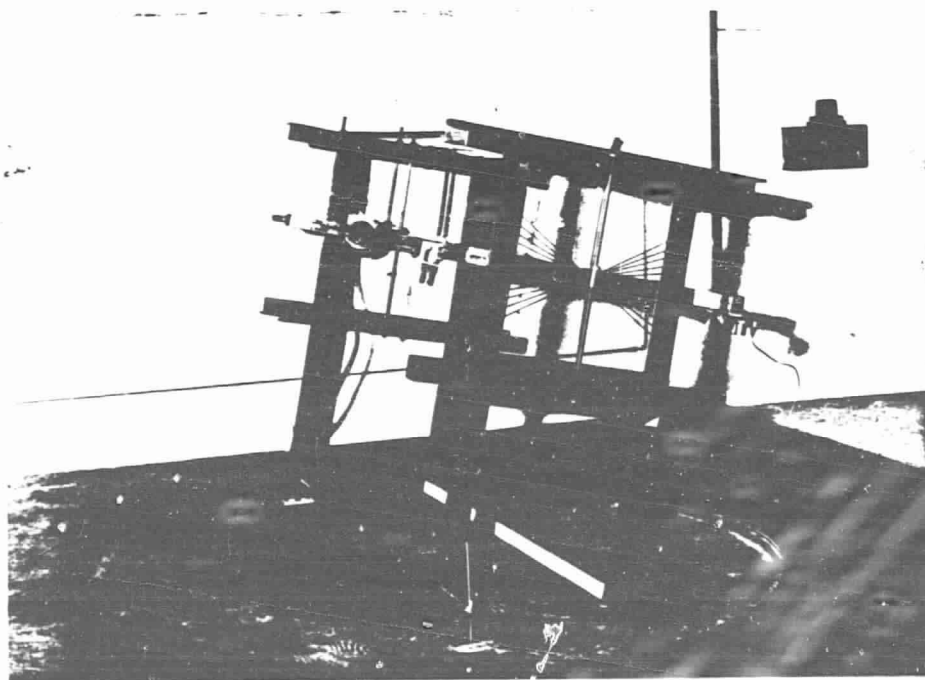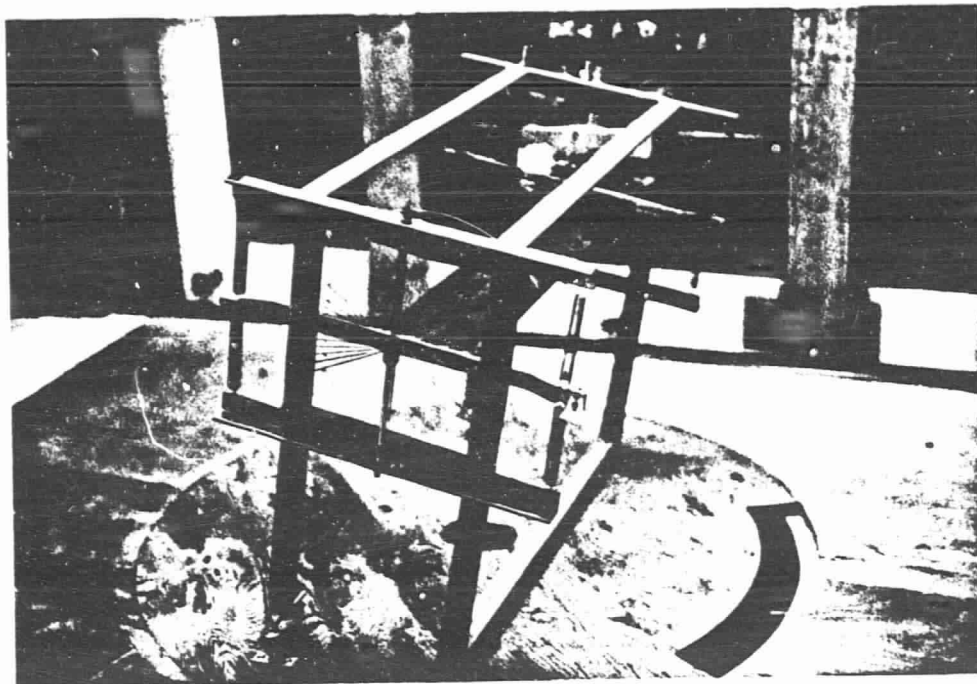
Photograph 1: Two views of the flutter frame and wing mounted in the tunnel.

Experimental Procedure and Data Measurement

When the desired torsional spring constant, initial angle of
attack and elastic axis were set, the electromagnet was turned on, and
the wind velocity was brought up to speed (test Re: 1.0×10^5-2.5×10^5).
The magnet was then switched off and, if flutter occured, the free-
stream velocity, frequency, peak-to-peak acceleration, and maximum and
minimum angles of oscillation were recorded. If, when the magnet was
switched off, flutter did not occur, the wing was tapped until it did
occur. The maximum angle to which the wing had to be tapped, in order
to excite self-sustained flutter, was then recorded along with the above
mentioned data. After this, the tunnel velocity was brought to zero,
and the procedure was repeated for a different value of V_∞. These steps

TABLE III. VARIATION of PARAMETERS for PSU EXPERIMENT.			
x/c	VELOCITY (ft/sec)	α_1/α_{ss}	ω_n (cyc/sec)
0.250	28-110	0.64-1.27	1.85-3.82
0.375	28-70	0.45-1.36	3.22-6.0
0.500	28-70	0.64-1.36	3.30-5.90

were carried out for the parametric varations shown in Table III.

Static equilibrium angles were measured using angular markings
drawn on a clear plastic surface which was taped to the near end of the
frame. Dynamic flutter amplitudes were measured using both the

aforementioned markings and an Endevco 2233 Accelerometer, which was attached to the near-end, aluminum wing-support bar. The accelerometer's signals were wired through an Endevco Amplifier and a high-frequency filter before being displayed on an oscilloscope screen from which peak-to-peak amplitude and frequency values were taken.

Experimental Results

Limit cycle oscillations about the 1/4 chord elastic axis were found to be very nearly sinusoidal. Flutter amplitudes varied from approximately 2.0 to 7.0 degrees. In general, as can be seen from Figure 17, the amplitudes increased with respect to V_∞. Values for ω/ω_n varied from 1.1 to 1.3 and showed a slight increase with respect to V_∞, as shown in Figure 18. In addition, k varied from 0.12 for stiff springs at low V_∞, to 0.03 for "loose" springs, at high V_∞, values large enough to yield unsteady stalling for all conditions studied. It should be noted here that a similar experiment, done at MIT (8), showed amplitudes of the same magnitude but produced no increase in these values with V_∞, for purely torsional stall flutter. However, this experiment did yield an increase in ω with V_∞. Figures 19 and 20 are graphs of these values.

Limit cycle oscillations about the 37.5% chord elastic axis were also found to be sinusoidal, but the amplitudes, as expected, were much larger, ranging from approximately 4.0 to 15.0 degrees. Again, as Figure 21 shows, amplitudes increased with V_∞ but began to level off at higher velocities. However, ω/ω_n for this case, stayed equal to 1.0 for
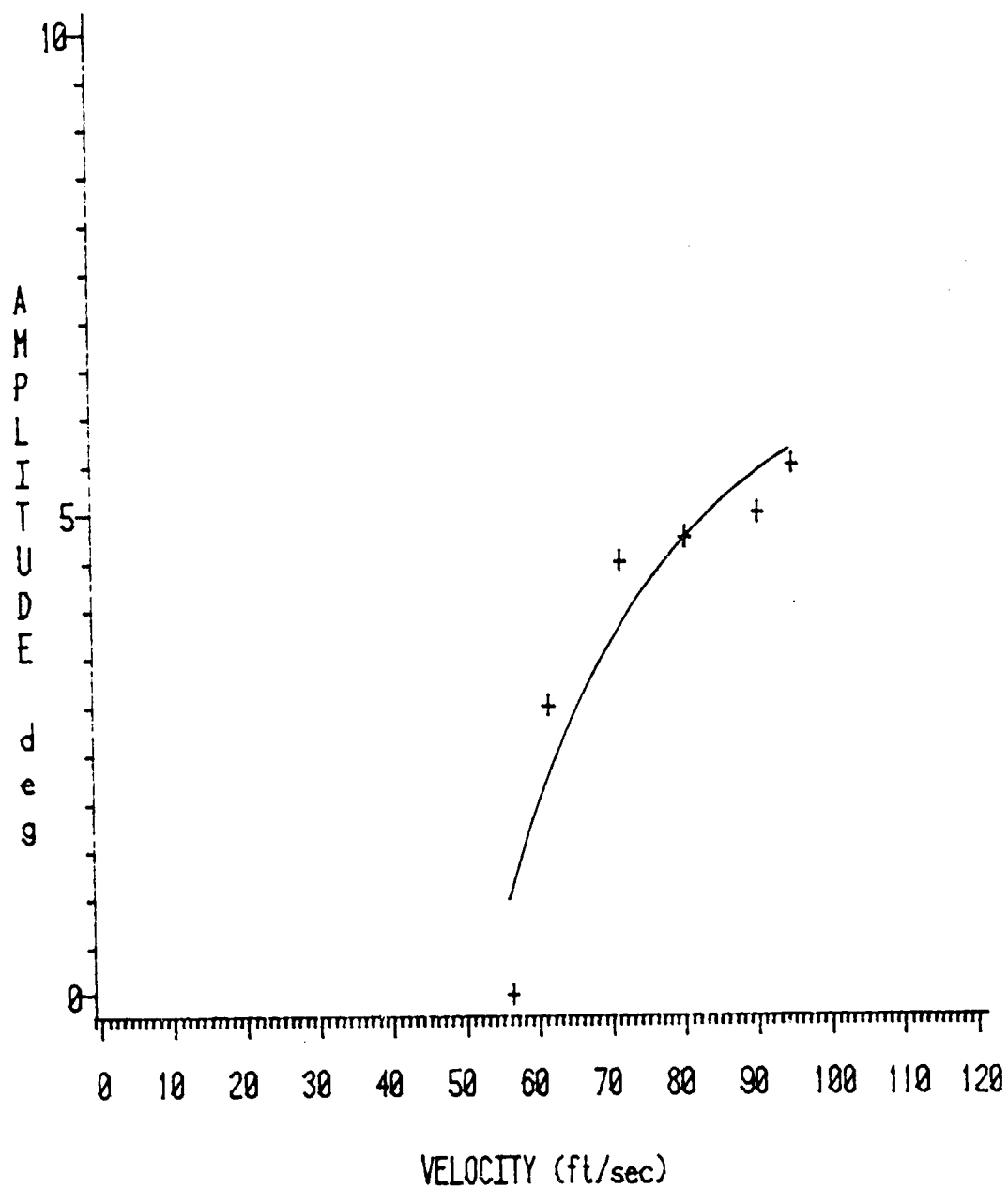
Elastic Axis=0.250c
Natural Frequency=1.85 Hz
Initial Angle of Attack=11.0 Degrees
Zeta=0.00994
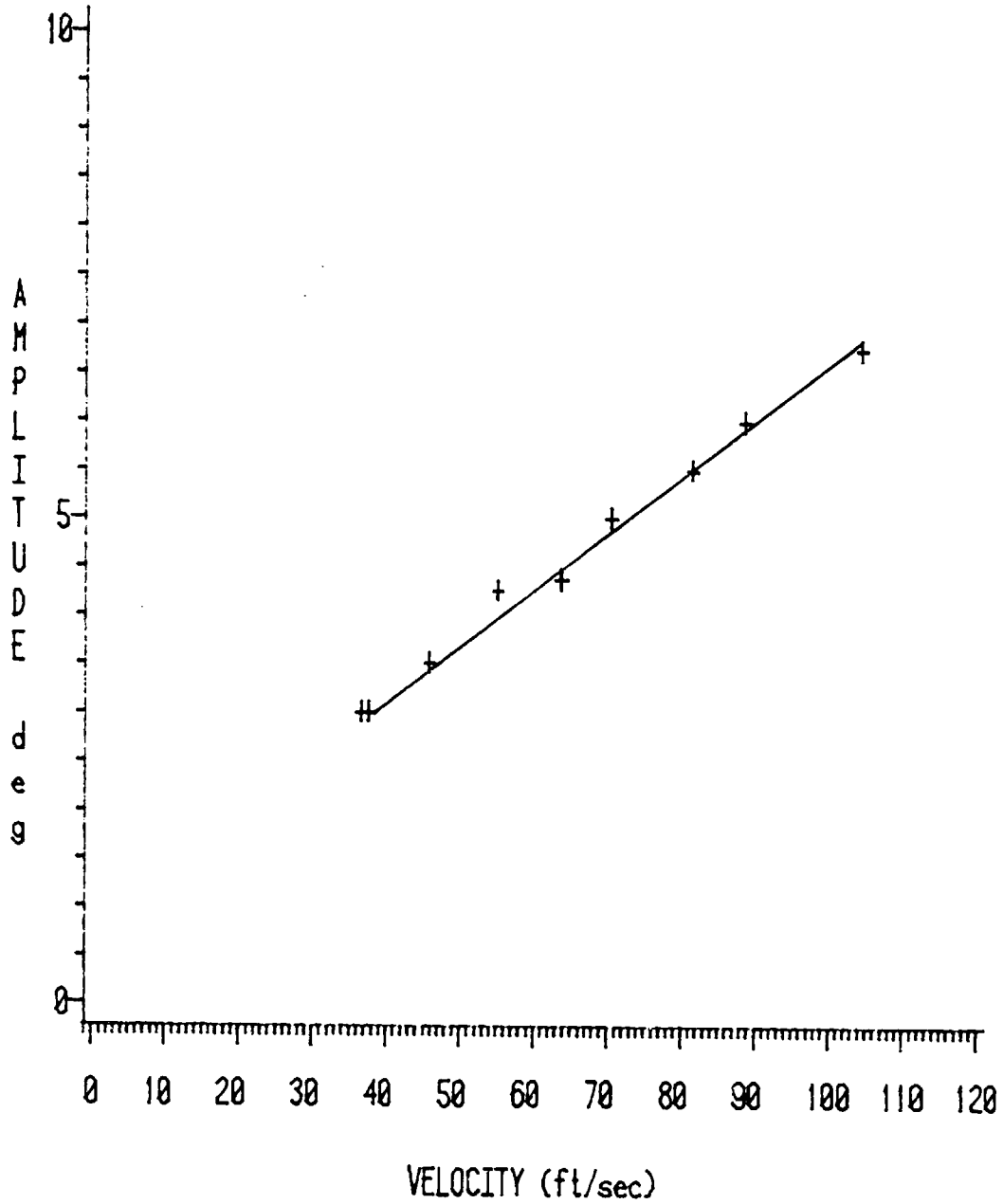
a.

FIGURE 17: Experimental amplitude values for PSU wing undergoing
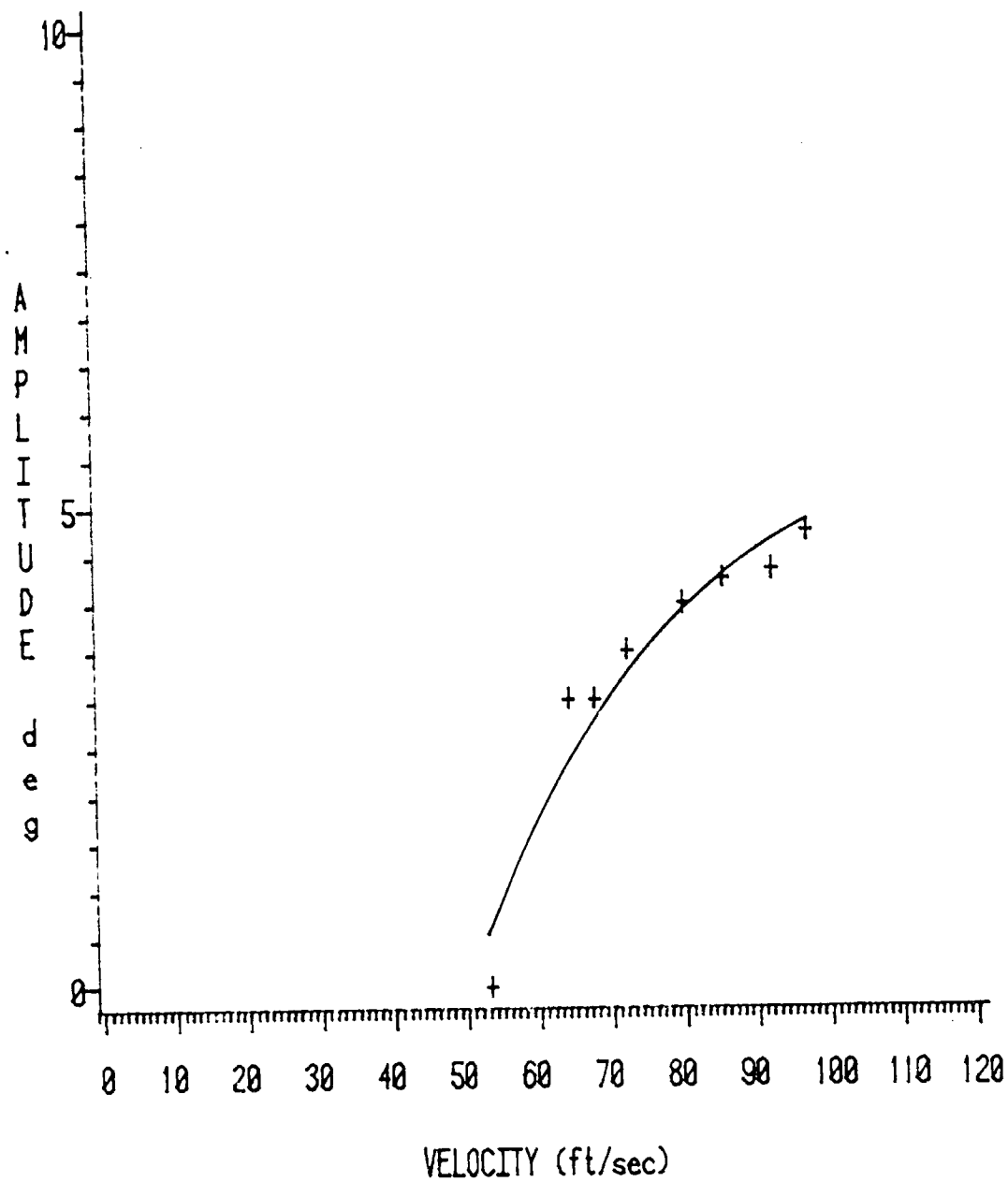torsional stall flutter.

Elastic Axis=0.250c
Natural Frequency=2.10 Hz
Initial Angle of Attack=14.0 Degrees
Zeta=0.01050

VELOCITY (ft/sec)

b.

FIGURE 17: (cont.).

Elastic Axis=0.250c
Natural Frequency=3.08 Hz
Initial Angle of Attack=12.5 Degrees
Zeta=0.00473

VELOCITY (ft/sec)

c.

FIGURE 17: (cont.).

Elastic Axis=0.250c
Natural Frequency=4.28 Hz
Initial Angle of Attack=11.0 Degrees
Zeta=0.00427

VELOCITY (ft/sec)

d.

FIGURE 17: (cont.).

Elastic Axis=0.250c
Natural Frequency=1.85 Hz
Initial Angle of Attack=11.0 Degrees
Zeta=0.00994

a.

FIGURE 18: Experimental frequency values for PSU wing undergoing
torsional stall flutter.

Elastic Axis=0.250c
Natural Frequency=2.10 Hz
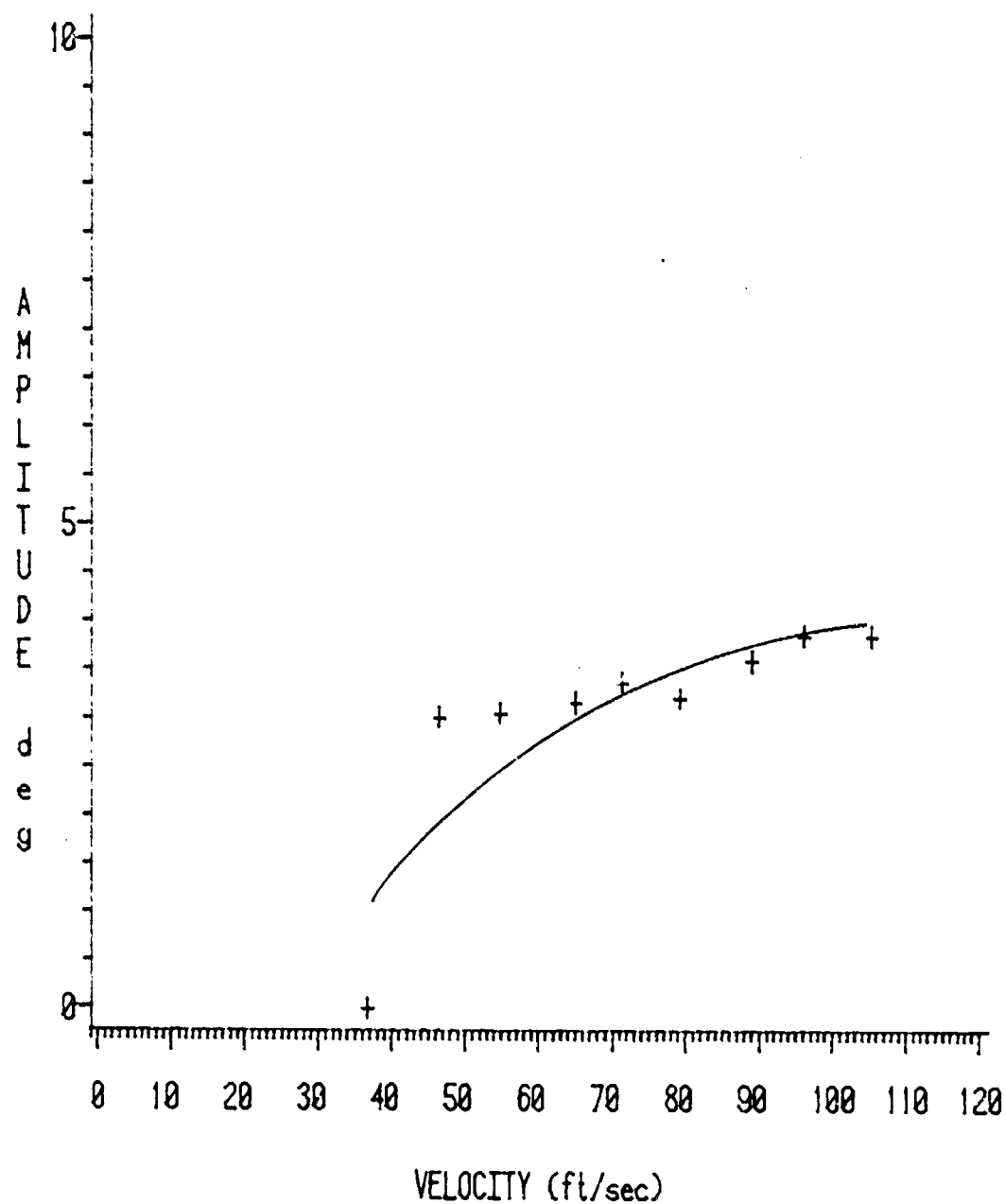Initial Angle of Attack=14.0 Degrees
Zeta=0.01050

VELOCITY (ft/sec)

b.

FIGURE 18: (cont.).

Elastic Axis=0.250c
Natural Frequency=3.08 Hz
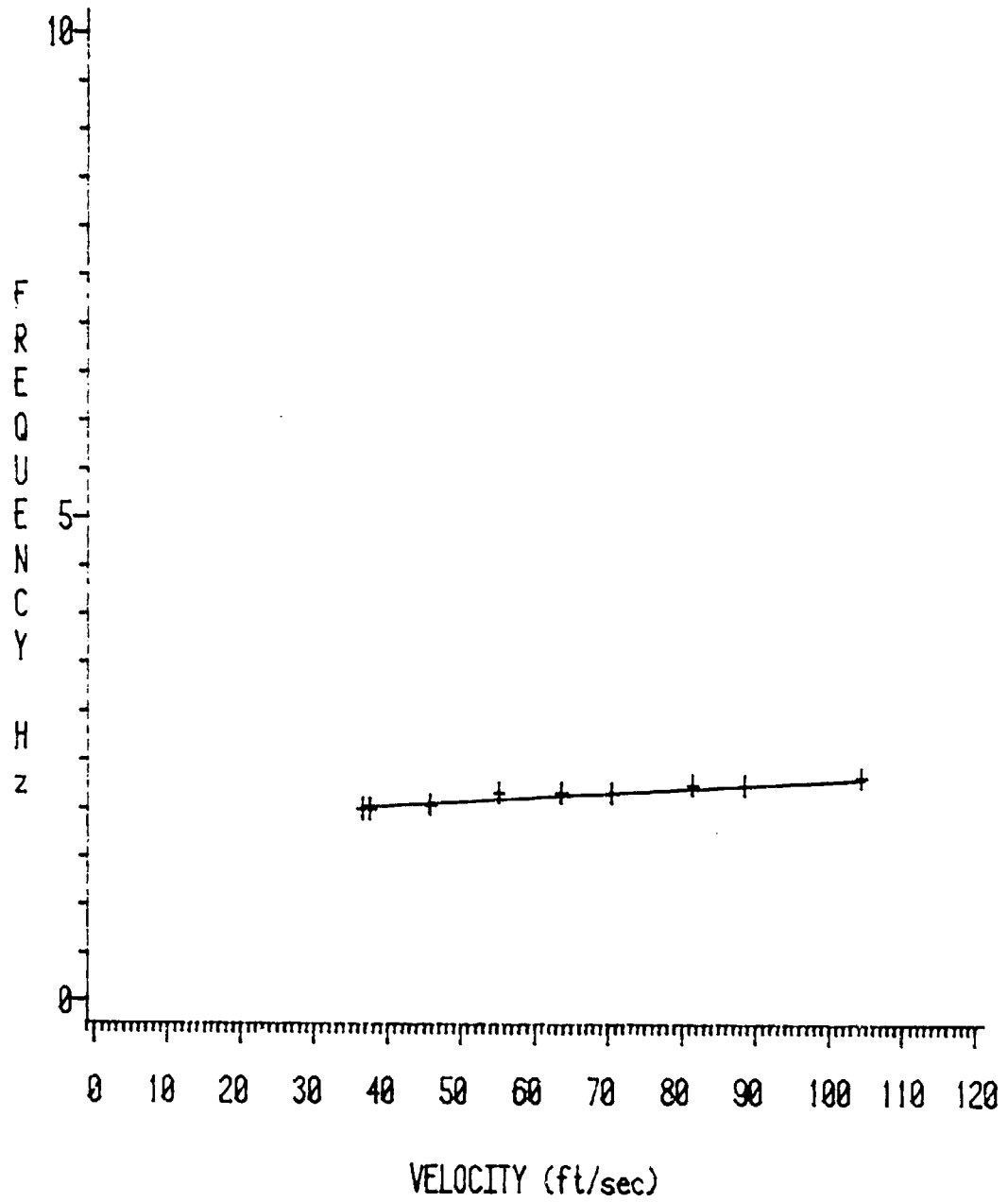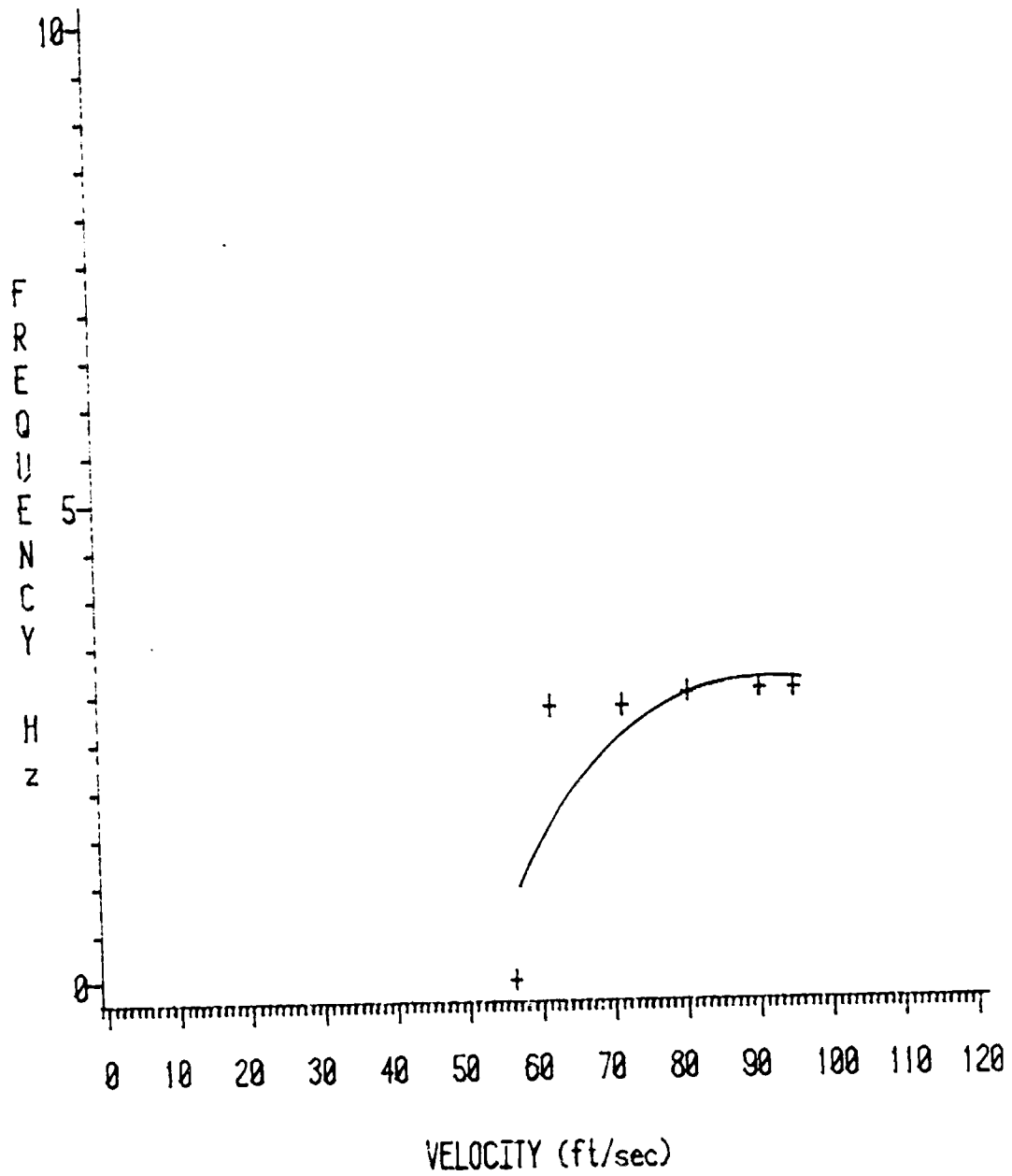Initial Angle of Attack=12.5 Degrees
Zeta=0.00473

VELOCITY (ft/sec)

c.

FIGURE 18: (cont.).

Elastic Axis=0.250c
Natural Frequency=4.28 Hz
Initial Angle of Attack=11.0 Degrees
Zeta=0.00427

VELOCITY (ft/sec)

d.

FIGURE 18: (cont.).

Elastic Axis=0.250c
Natural Frequency=2.55 Hz
Initial Angle of Attack=14.0 Degrees
Zeta=0.13

FIGURE 19: Experimental amplitude values for MIT airfoil undergoing torsional stall flutter.

Elastic Axis=0.250c
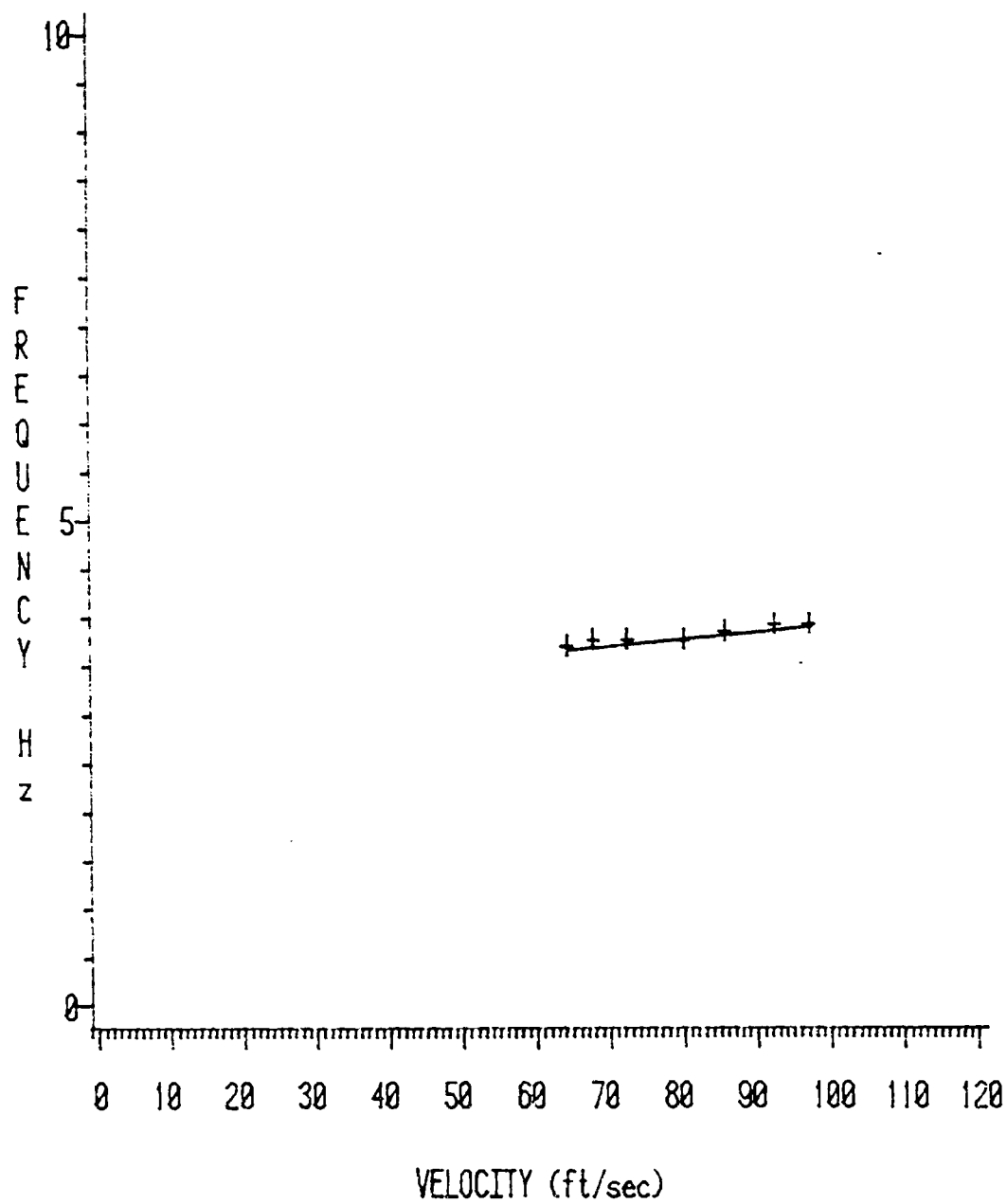Natural Frequency=2.55 Hz
Initial Angle of Attack=14.0 Degrees
Zeta=0.13

FIGURE 20: Experimental frequency values for MIT airfoil undergoing torsional stall flutter.

Elastic Axis=0.375c
Natural Frequency=3.81 Hz
Initial Angle of Attack=7.0 Degrees
Zeta=0.00679

a.

FIGURE 21: Experimental amplitude values for PSU wing undergoing torsional stall flutter.

Elastic Axis=0.375c
Natural Frequency=5.50 Hz
Initial Angle of Attack=4.8 Degrees
Zeta=0.00628

b.

FIGURE 21: (cont.).

Elastic Axis=0.375c
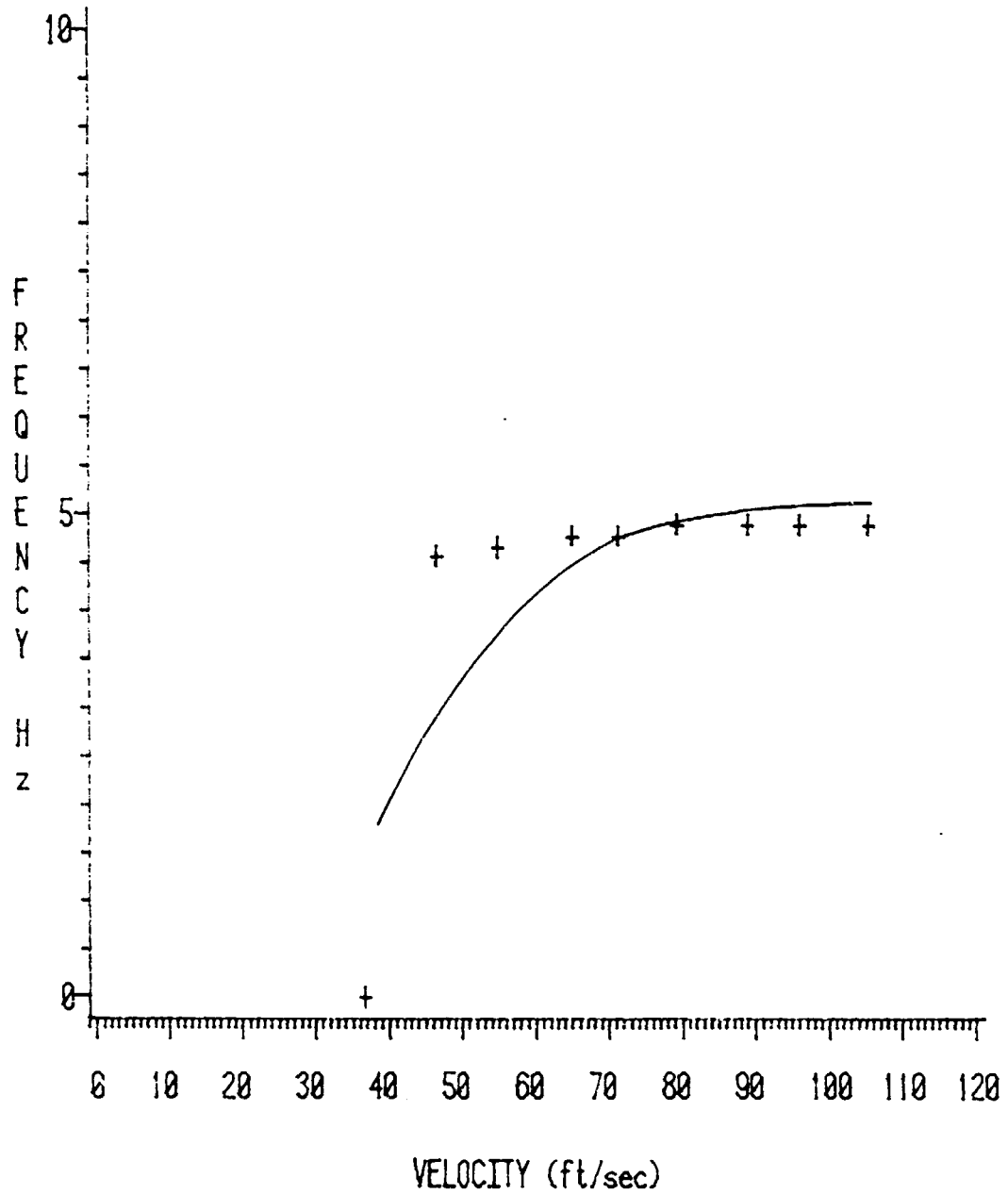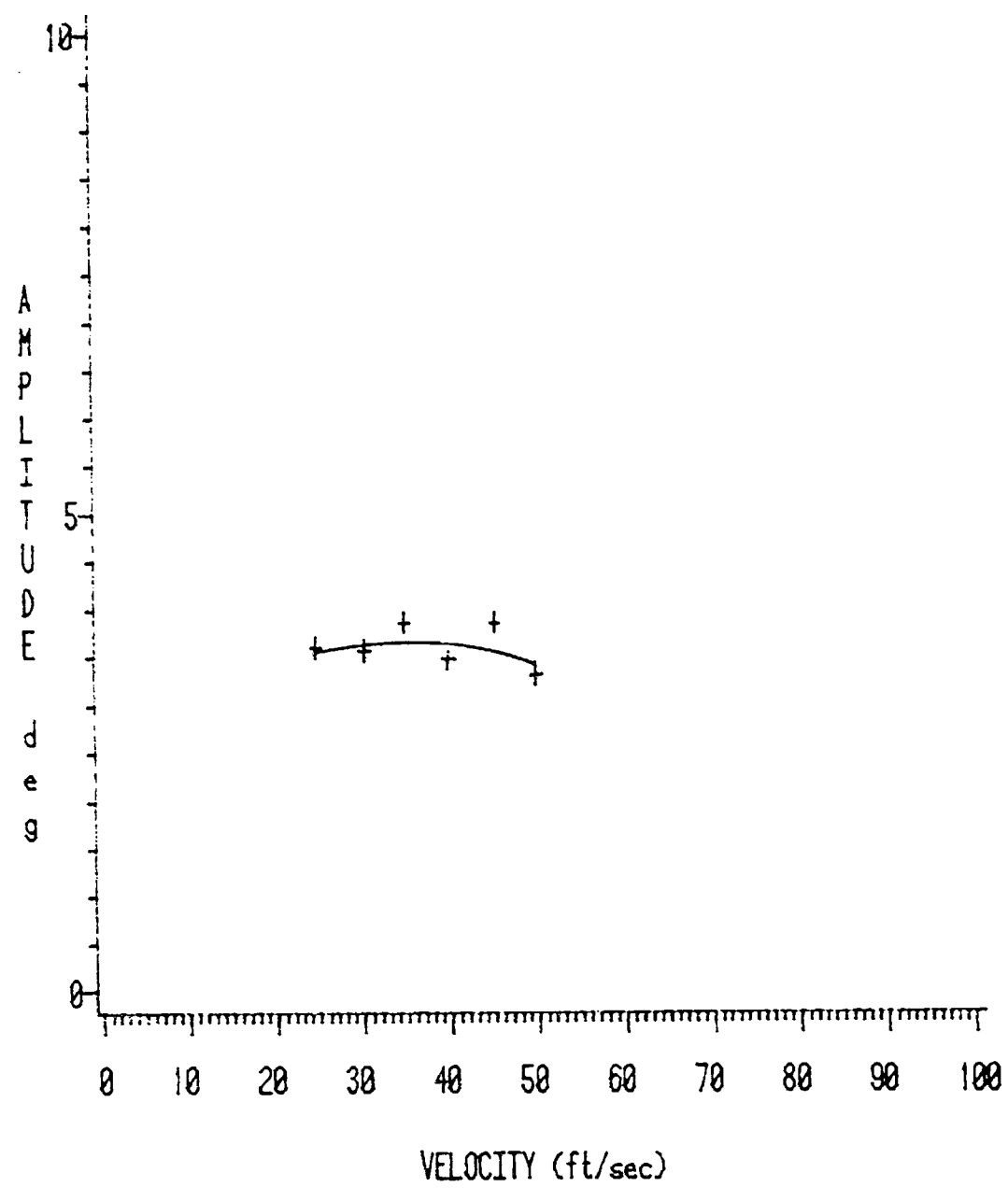Natural Frequency=5.83 Hz
Initial Angle of Attack=10.5 Degrees
Zeta=0.00888

VELOCITY (ft/sec)
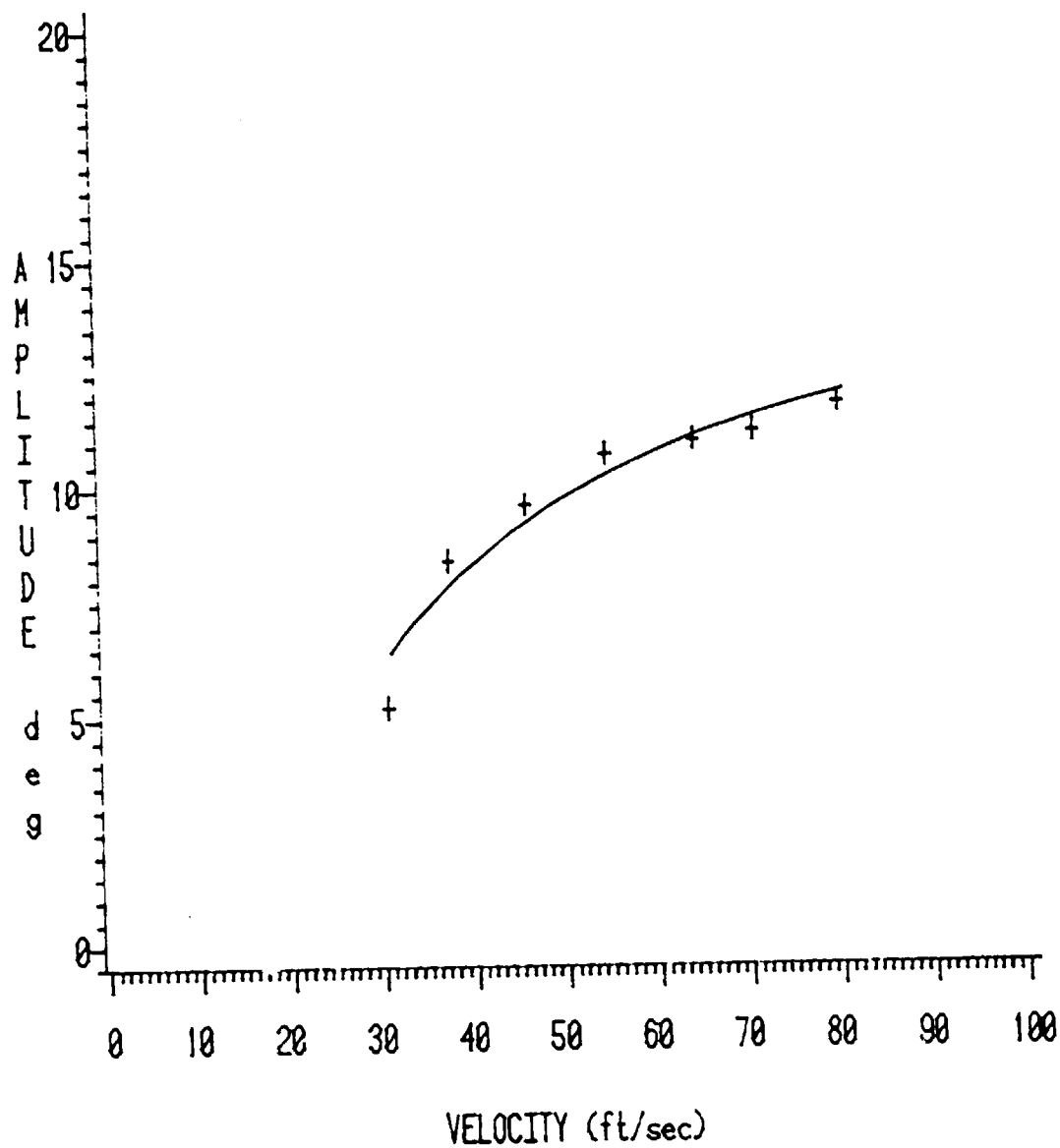
c.

FIGURE 21: (cont.).

Elastic Axis=0.375c
Natural Frequency=6.00 Hz
Initial Angle of Attack=9.0 Degrees
Zeta=0.00493

d.

FIGURE 21: (cont.).

all trials and conditions (Figure 22). Again, reduced frequencies were
high enough to produce unsteady conditions; values of k ranged from 0.04
to 0.23.

Results for oscillations about the 50.0% chord elastic axis are
virtually the same as those obtained from oscillations about the 37.5%
chord elastic axis, except that amplitudes vary from approximately 10.0
to 20.0 degrees, as shown in Figures 23 and 24.

Elastic Axis=0.375c
Natural Frequency=3.81 Hz
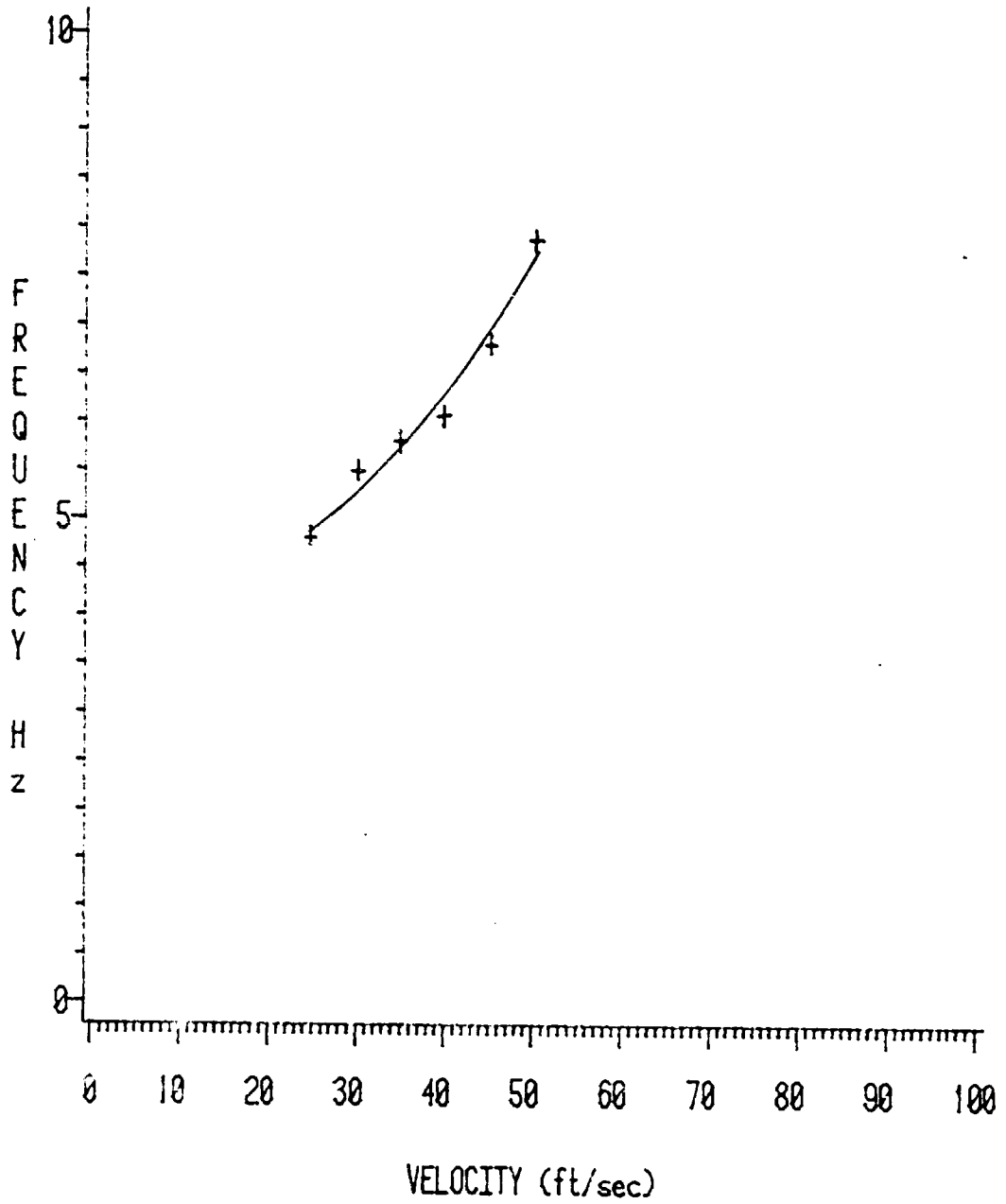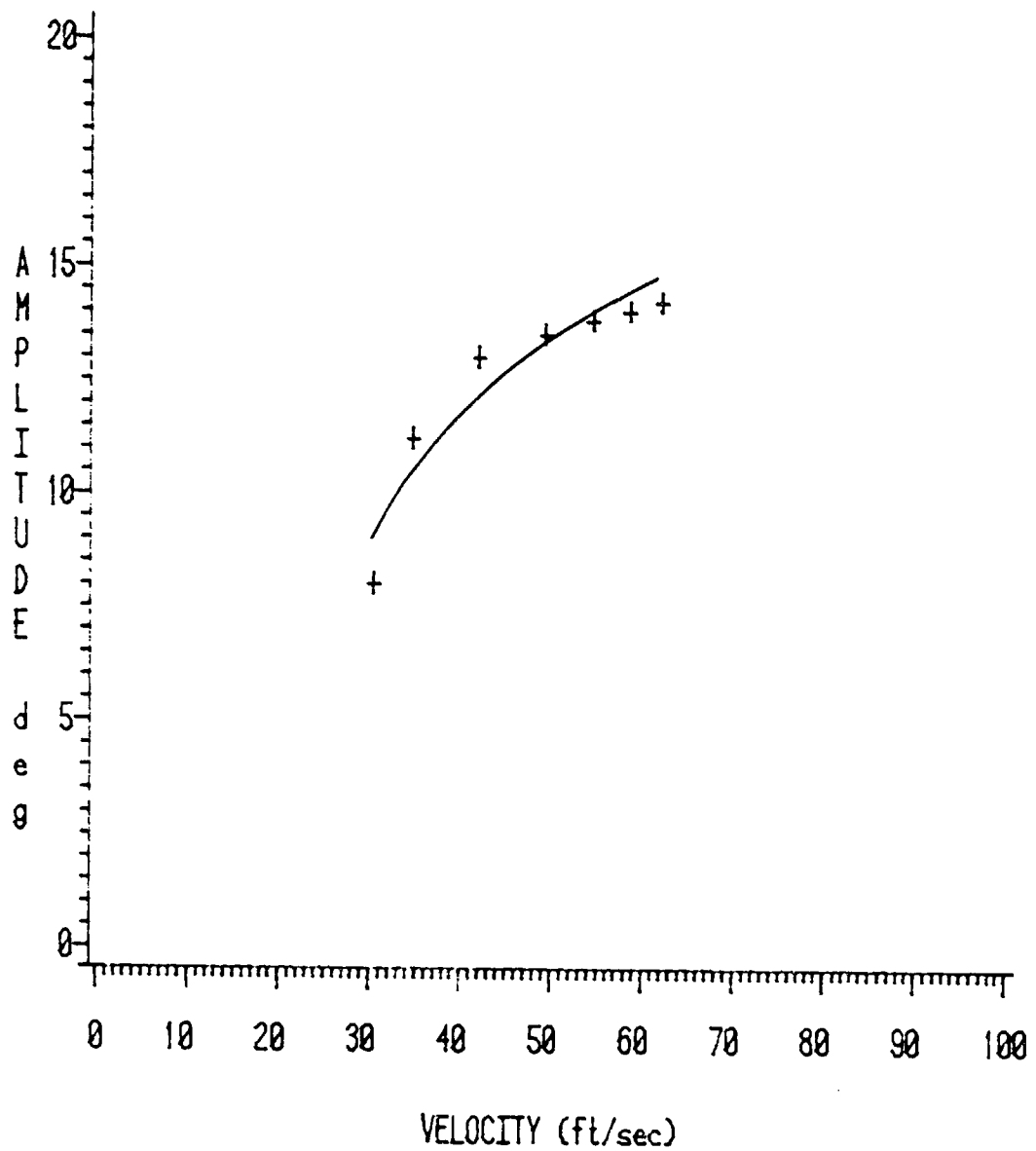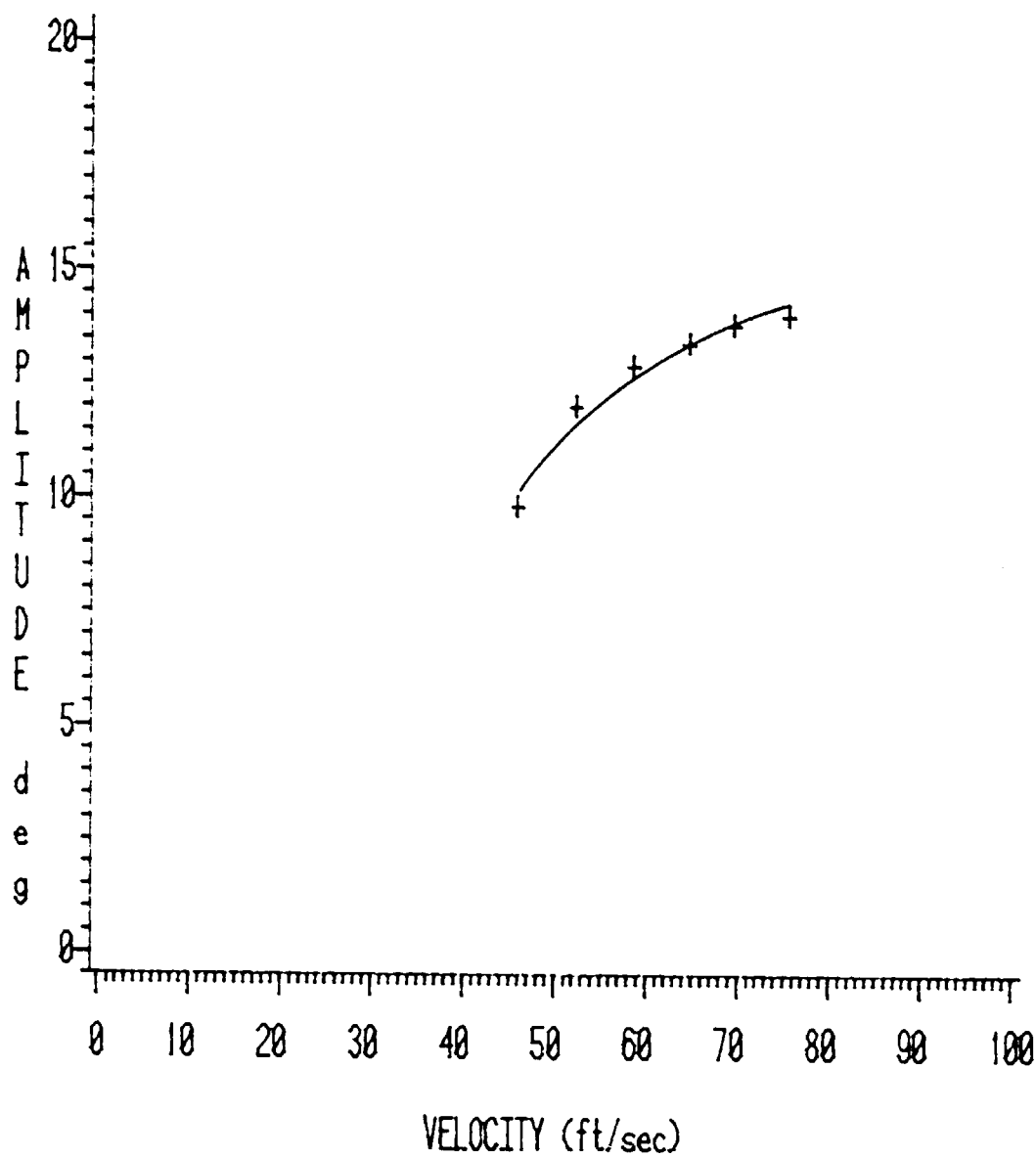Initial Angle of Attack=7.0 Degrees
Zeta=0.00679

a.

FIGURE 22: Experimental frequency values for PSU wing undergoing torsional
stall flutter.

Elastic Axis=0.375c
Natural Frequency=5.50 Hz
Initial Angle of Attack=4.8 Degrees
Zeta=0.00628

VELOCITY (ft/sec)

b.

FIGURE 22: (cont.).

Elastic Axis=0.375c
Natural Frequency=5.83 Hz
Initial Angle of Attack=10.5 Degrees
Zeta=0.00888

VELOCITY (ft/sec)

c.

FIGURE 22: (cont.).

Elastic Axis=0.375c
Natural Frequency=6.00 Hz
Initial Angle of Attack=9.0 Degrees
Zeta=0.00493

VELOCITY (ft/sec)

d.

FIGURE 22: (cont.).

Elastic Axis=0.500c
Natural Frequency=3.30 Hz
Initial Angle of Attack=6.8 Degrees
Zeta=0.00670

a.

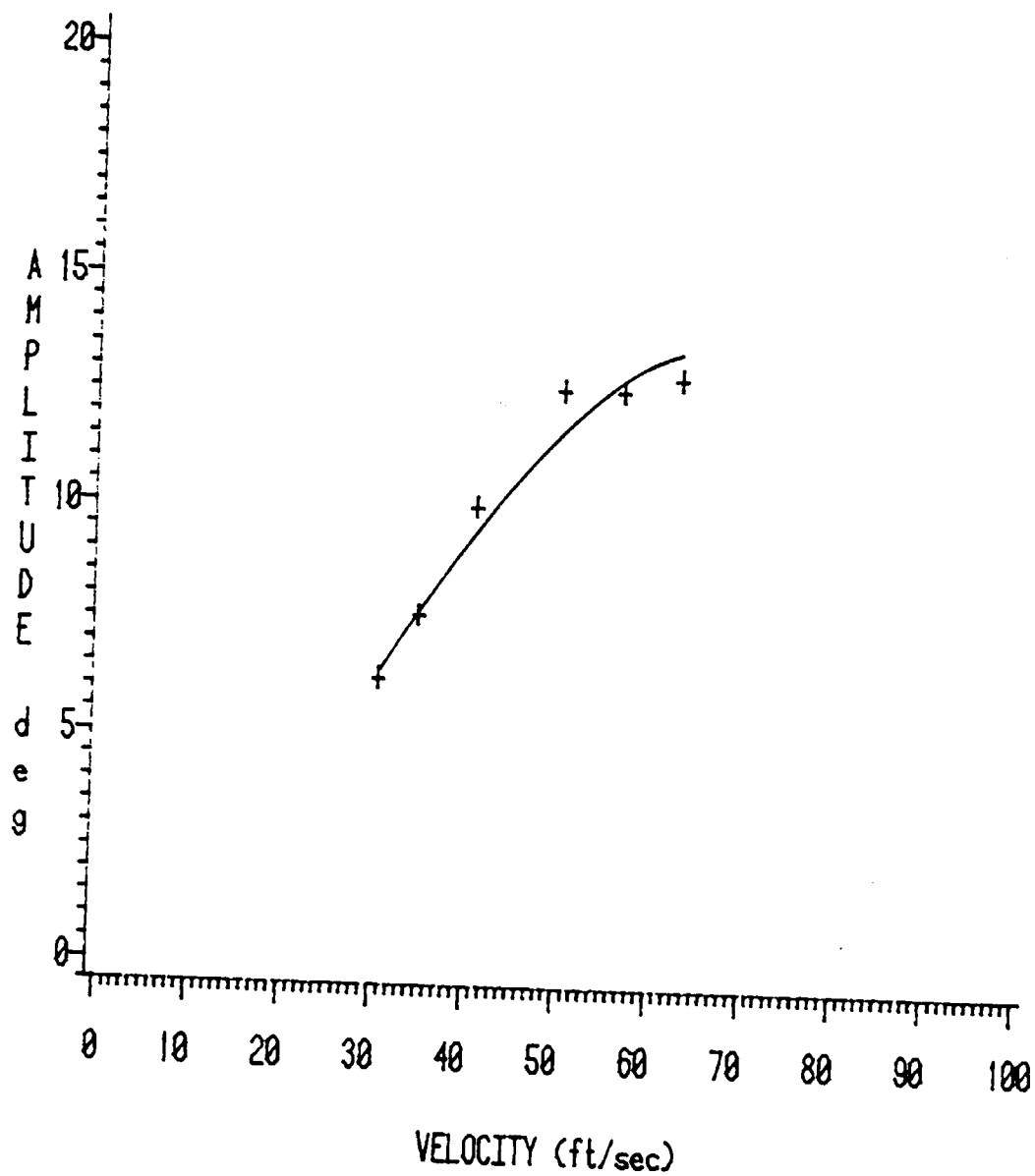FIGURE 23: Experimental amplitude values for PSU wing undergoing torsional
stall flutter.

Elastic Axis=0.500c
Natural Frequency=3.83 Hz
Initial Angle of Attack=10.8 Degrees
Zeta=0.00726

VELOCITY (ft/sec)

b.

FIGURE 23: (cont.).

Elastic Axis=0.500c
Natural Frequency=5.48 Hz
Initial Angle of Attack=8.9 Degrees
Zeta=0.00493

c.

FIGURE 23: (cont.).

71

Elastic Axis=0.500c
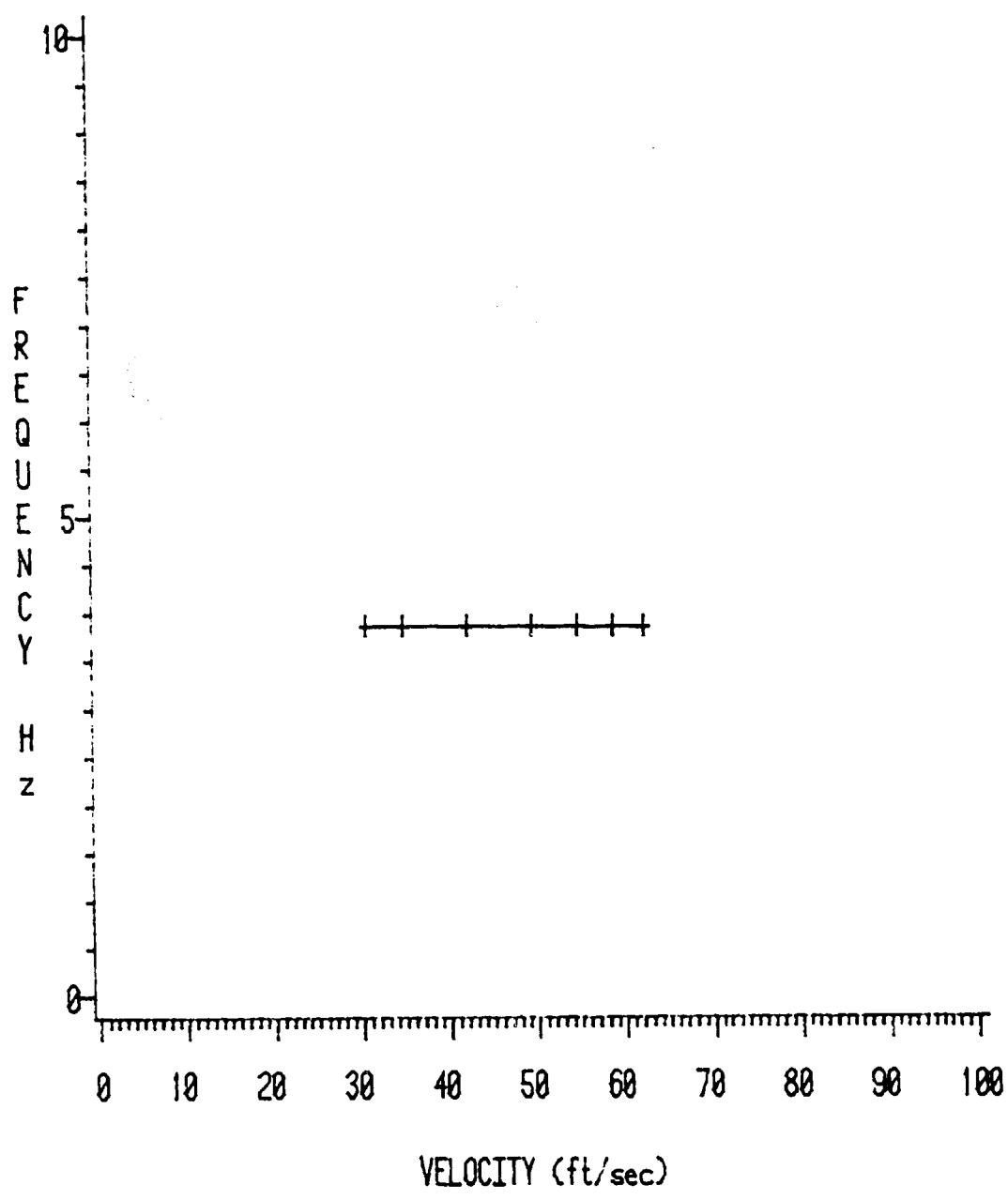Natural Frequency=5.90 Hz
Initial Angle of Attack=12.8 Degrees
Zeta=0.01090

VELOCITY (ft/sec)
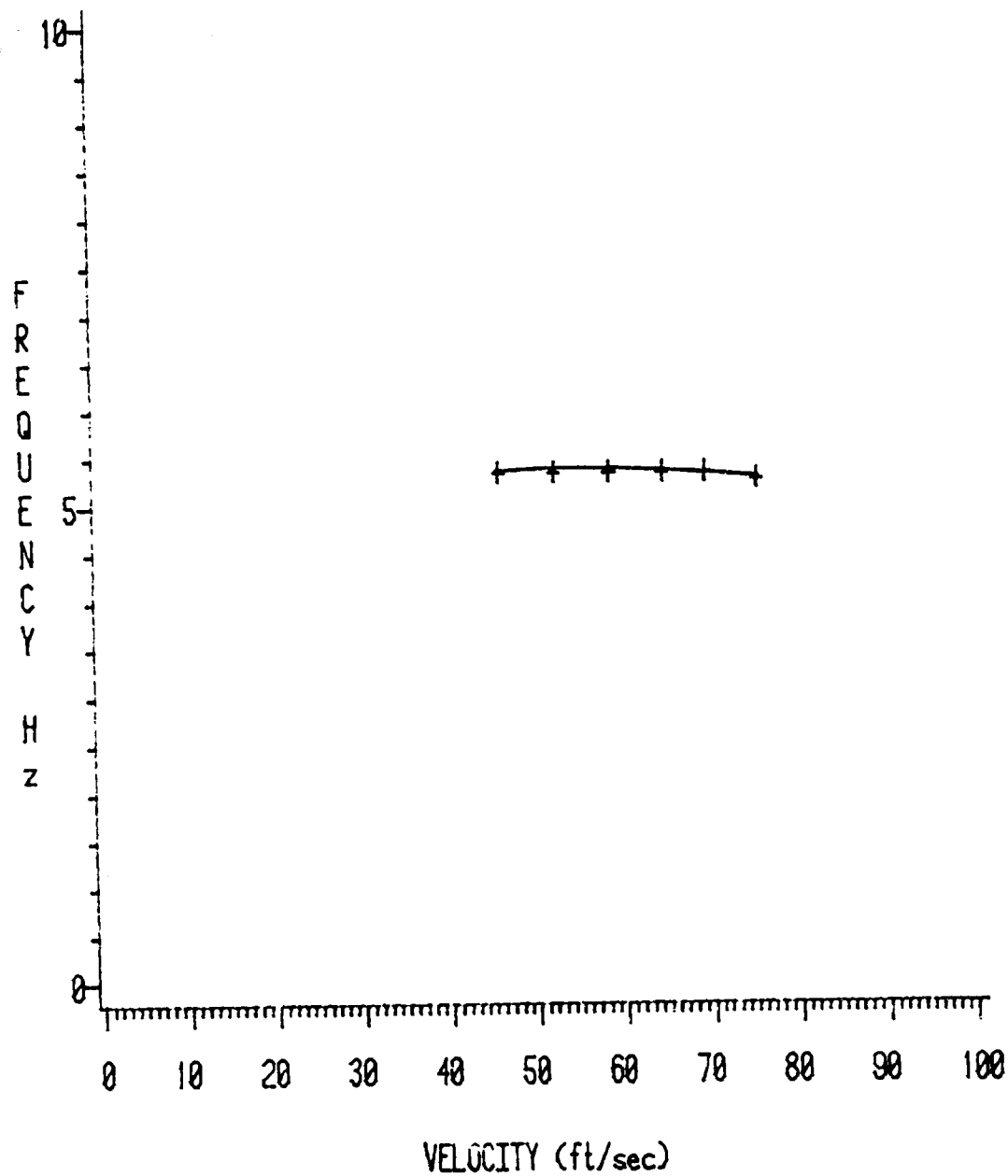
d.

FIGURE 23: (cont.).

Elastic Axis=0.500c
Natural Frequency=3.30 Hz
Initial Angle of Attack=6.8 Degrees
Zeta=0.00670

a.

FIGURE 24: Experimental frequency values for PSU wing undergoing torsional
stall flutter.
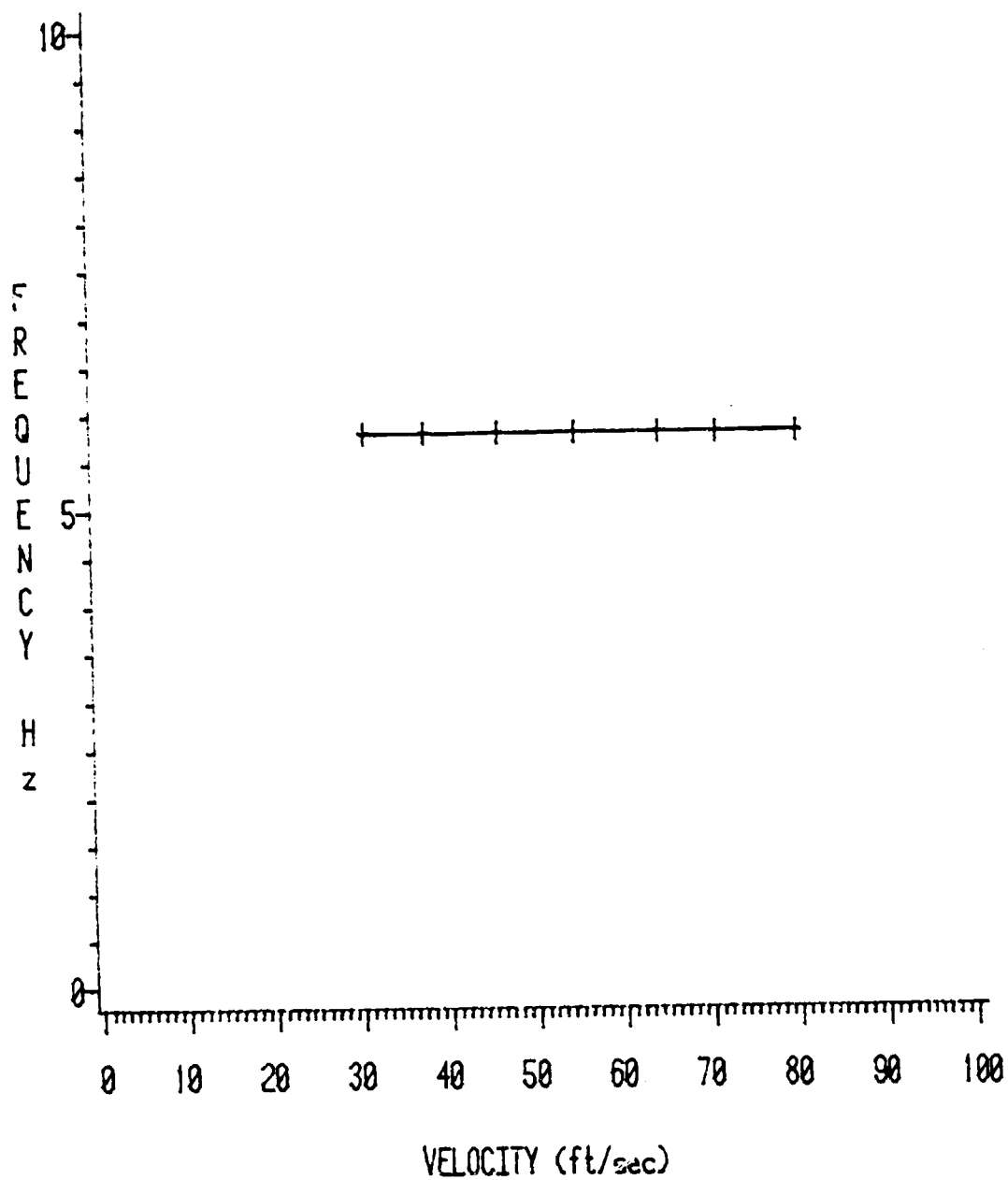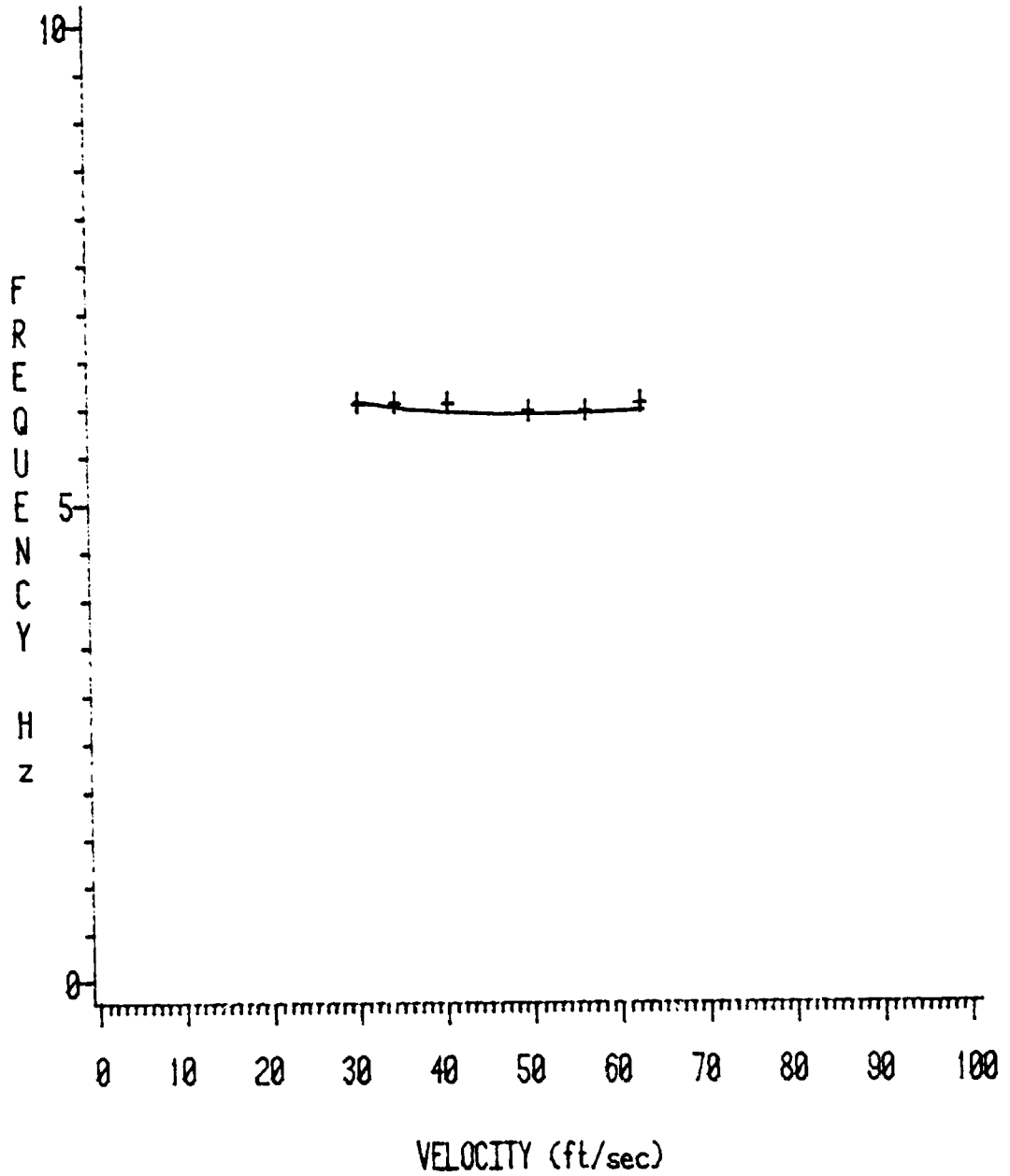
Elastic Axis=0.500c
Natural Frequency=3.83 Hz
Initial Angle of Attack=10.8 Degrees
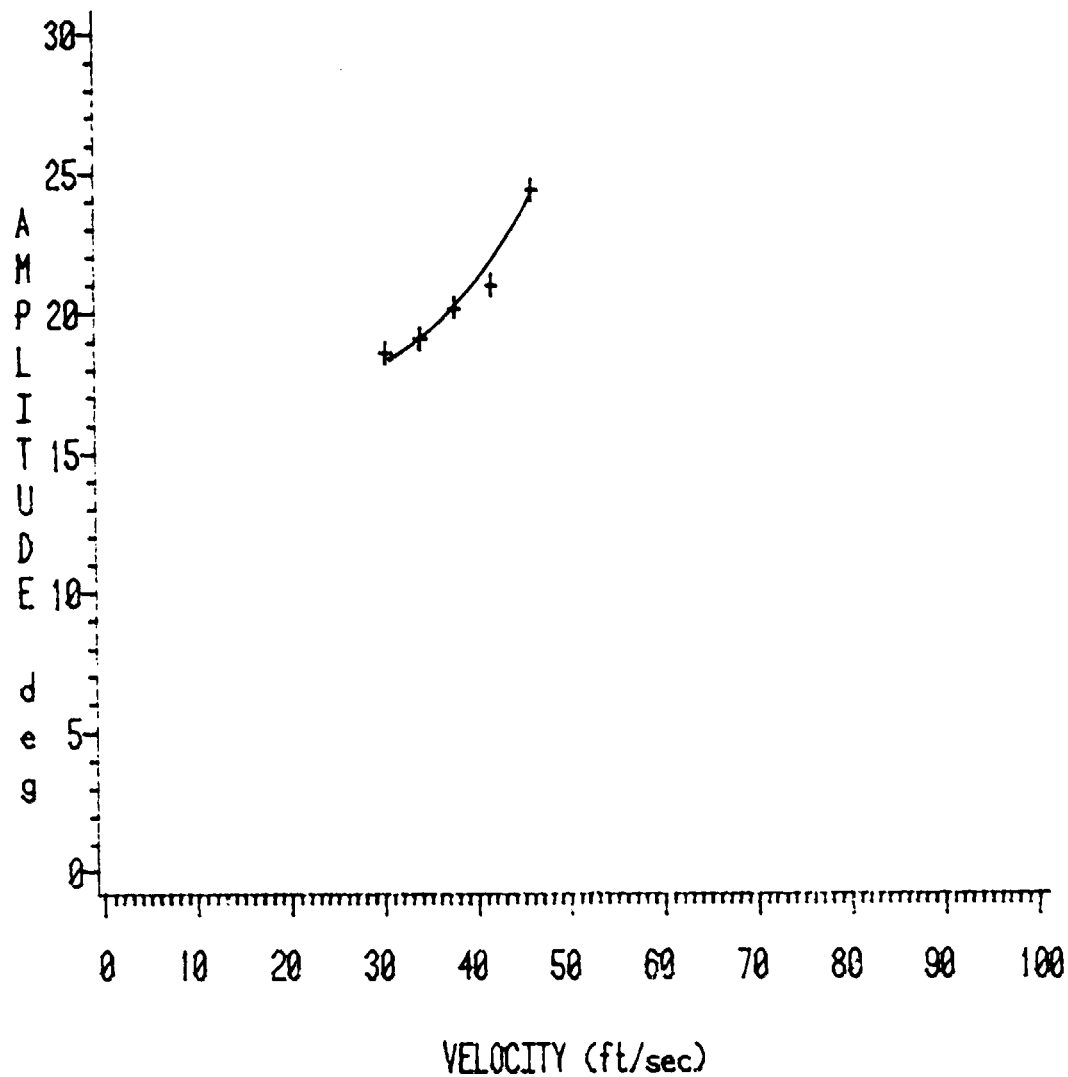Zeta=0.00726
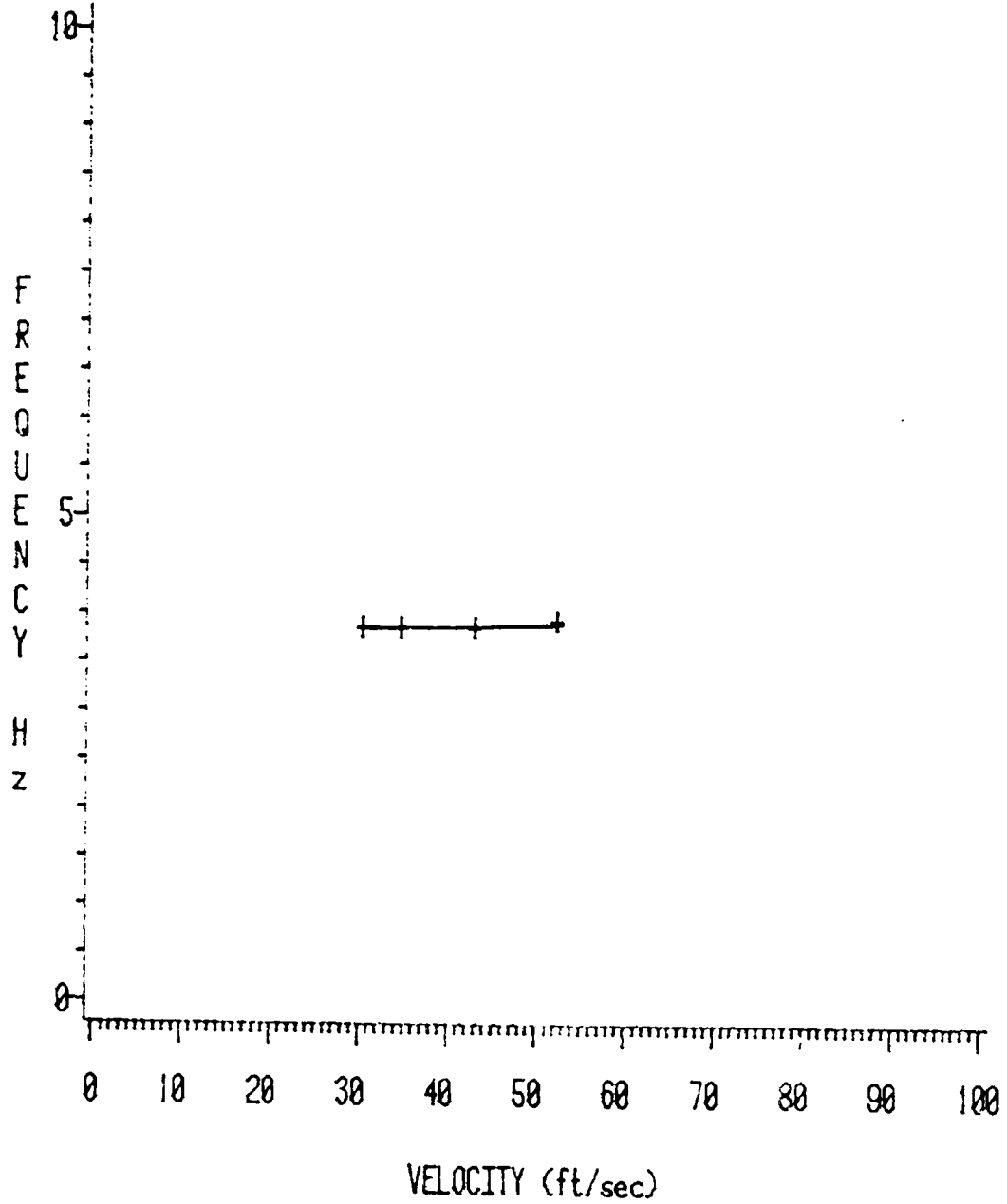
b.

FIGURE 24: (cont.).

Elastic Axis=0.500c
Natural Frequency=5.48 Hz
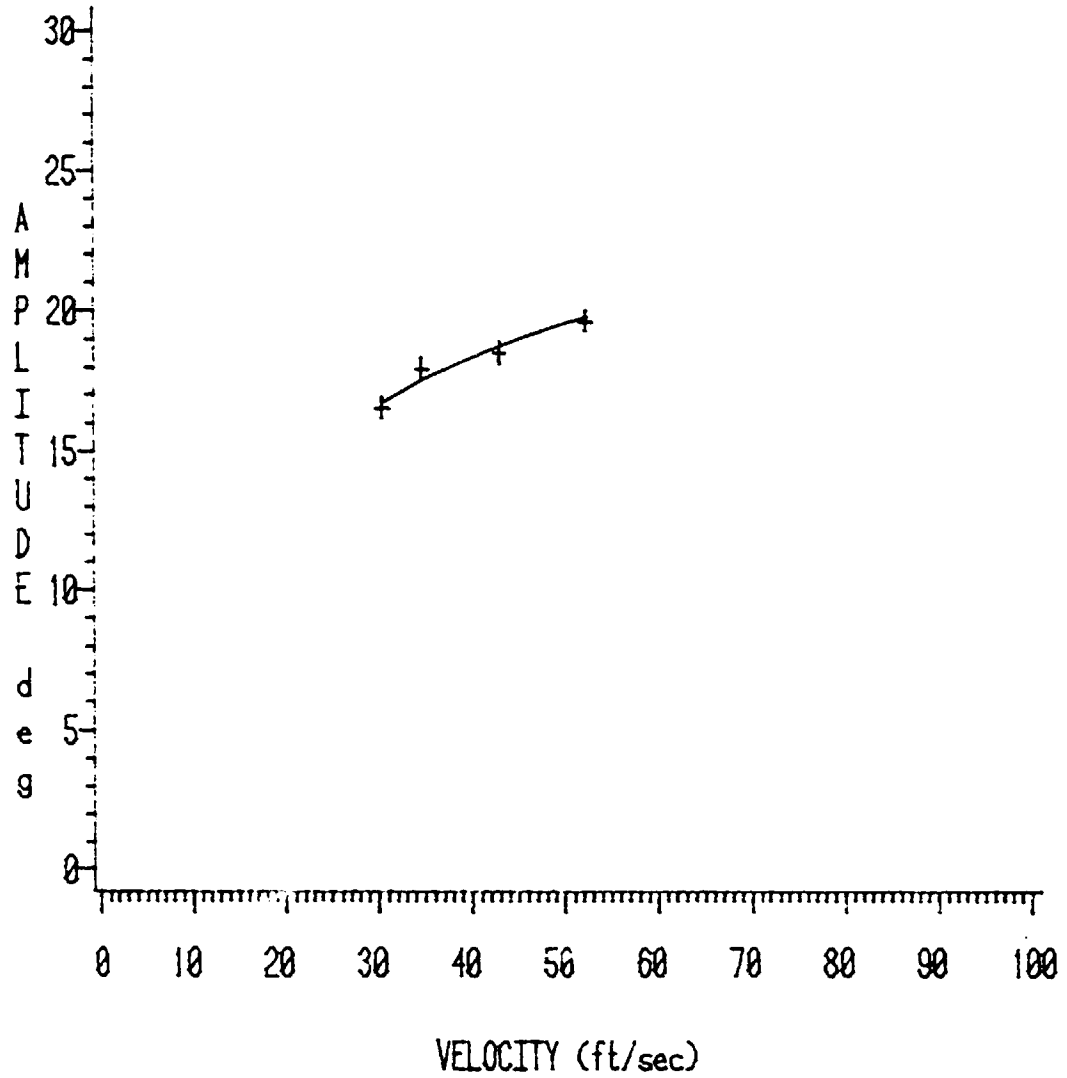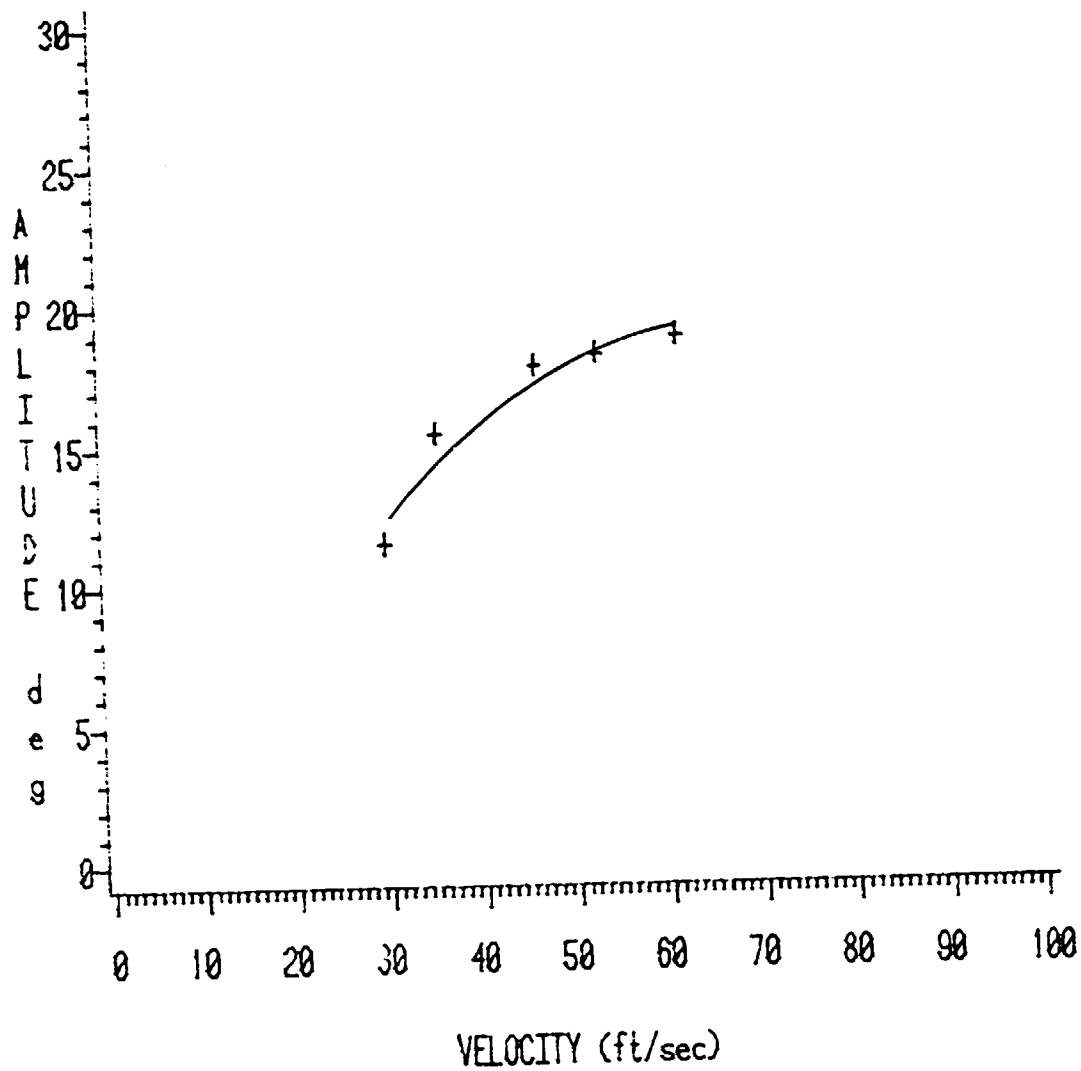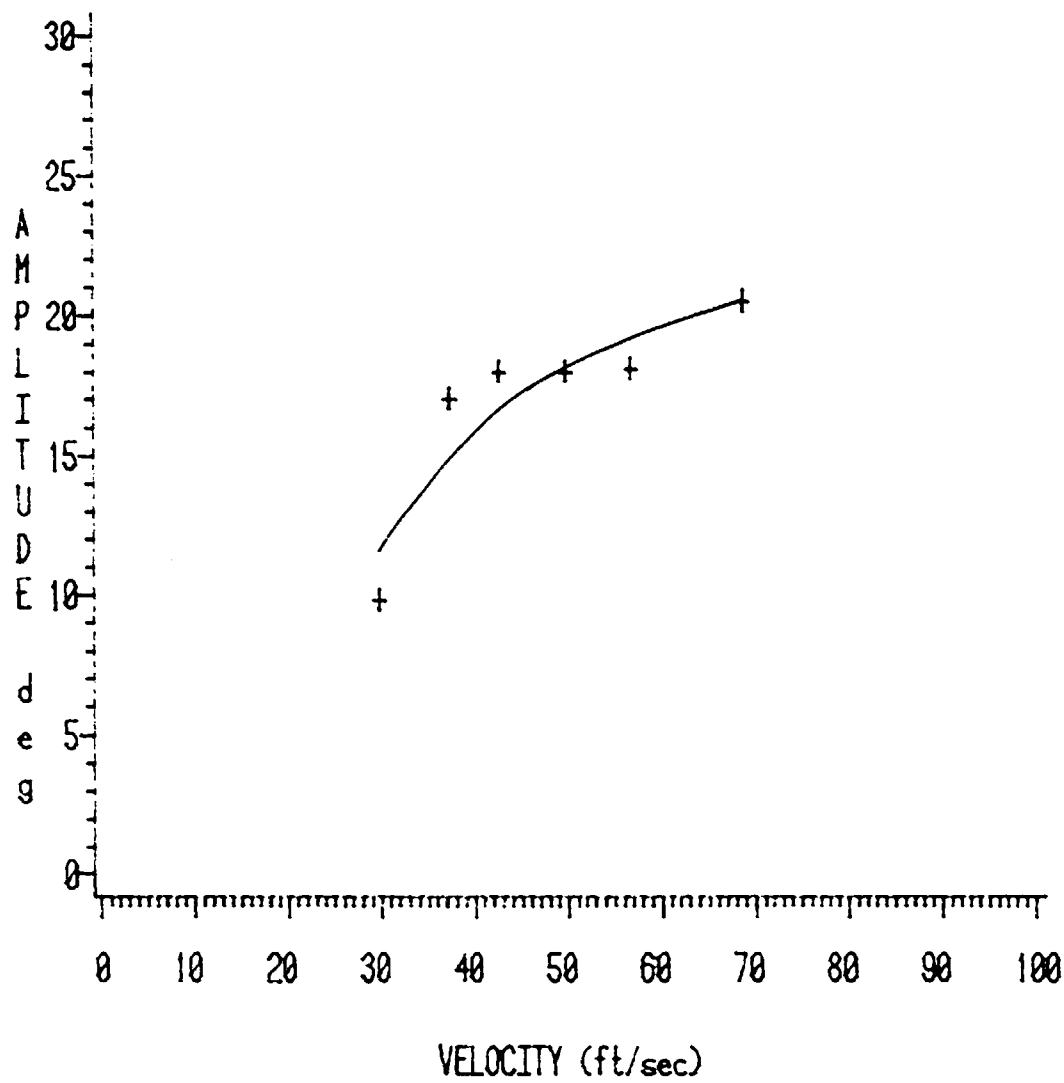Initial Angle of Attack=8.9 Degrees
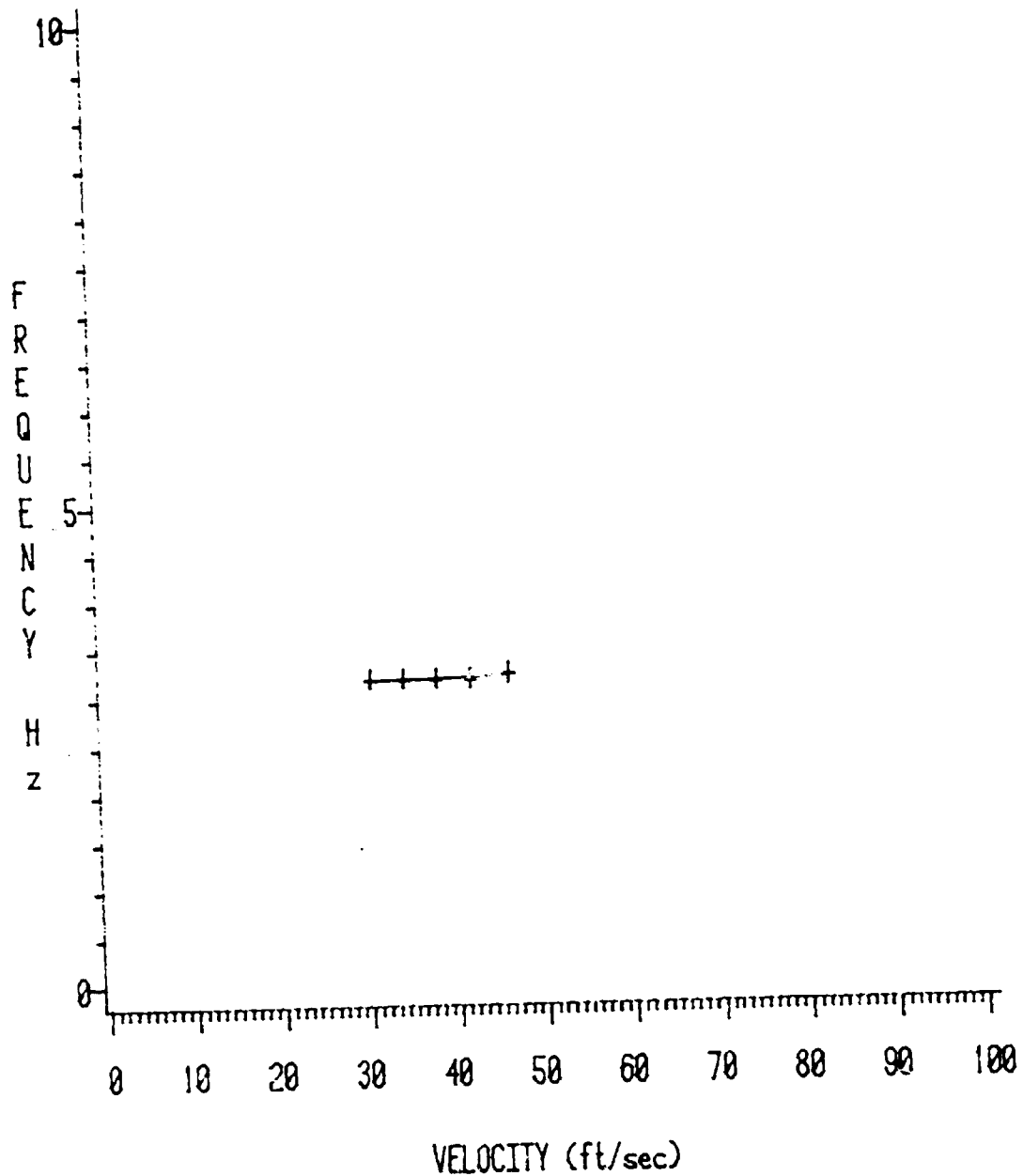Zeta=0.00493
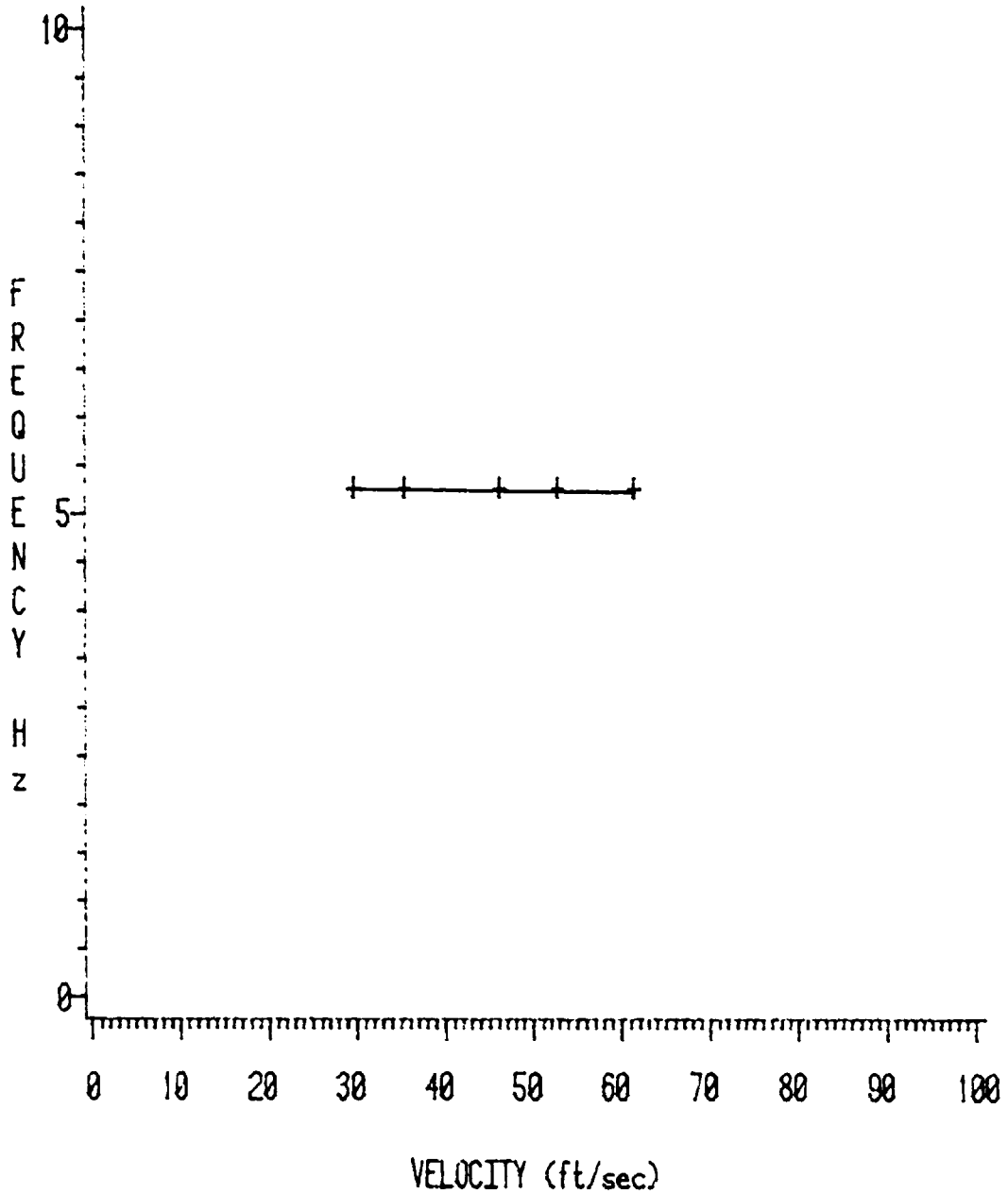
c.

FIGURE 24: (cont.).

Elastic Axis=0.500c
Natural Frequency=5.90 Hz
Initial Angle of Attack=12.8 Degrees
Zeta=0.01090

VELOCITY (ft/sec)
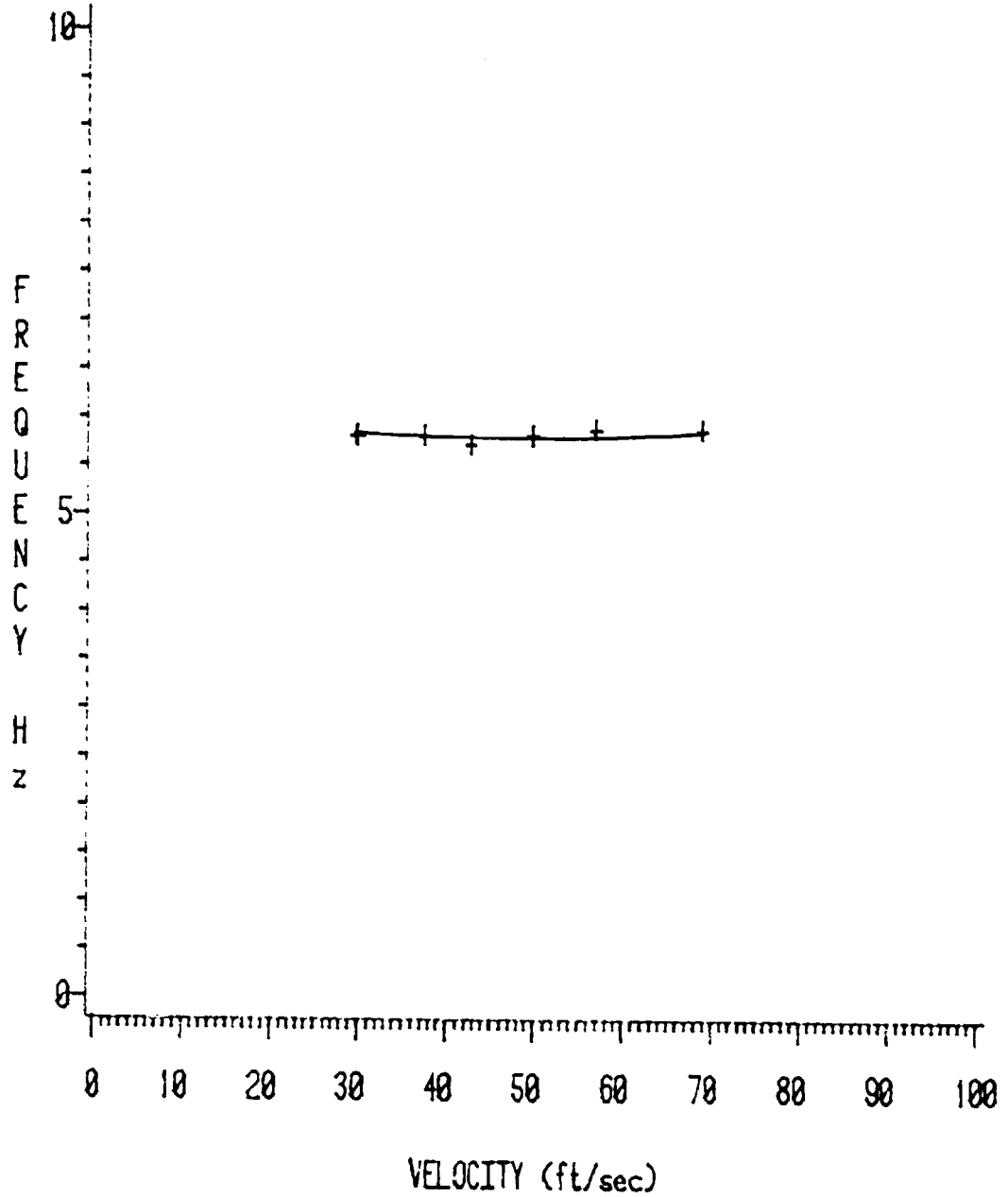
d.

FIGURE 24: (cont.).

CHAPTER V

COMPARISON BETWEEN PREDICTED AND EXPERIMENTAL
STALL FLUTTER RESPONSE

The comparison between predicted and experimental results is only fair. For the case where the elastic axis was positioned at the 1/4 chord, predicted values of amplitudes are consistently lower than those taken from the experiment. Figures 25a through 25d show typical cases. Note that comparisons are fairly accurate at lower velocities, but that they get progressively worse at higher velocities. This is because computed values show little increase with V_∞, in contrast to the similar but much greater increase shown by experimental data. Relative values of frequency show exactly opposite trends: predicted values of ω overestimate experimental values, and they increase with V_∞ while experimental values do not (Figure 26). Comparison with MIT data, where MIT's NACA 0012 airfoil data were substituted into the UTRC program, shows an underprediction of both amplitude and frequency, but the slopes of both are accurately predicted (Figure 27).

Predicted and experimental data taken from the 37.5% chord elastic axis show much better agreement than those taken from the 1/4 chord elastic axis. Unfortunately, the program often went out of its bounds due to the high angles of attack reached during the larger amplitude oscillations. When it did, predicted values diverged yielding very poor comparisons. However, when it stayed in bounds, predicted values yielded the following results: amplitude errors are of the same order of magnitude as those of the 1/4 chord elastic axis, but, in general, the slope of the amplitude lines are predicted fairly well

Elastic Axis=0.250c

Natural Frequency=1.85 Hz

Initial Angle of Attack=11.0 Degrees

ZETA=0.00994

— + — Experimental

--△-- Predicted

VELOCITY (ft/sec)
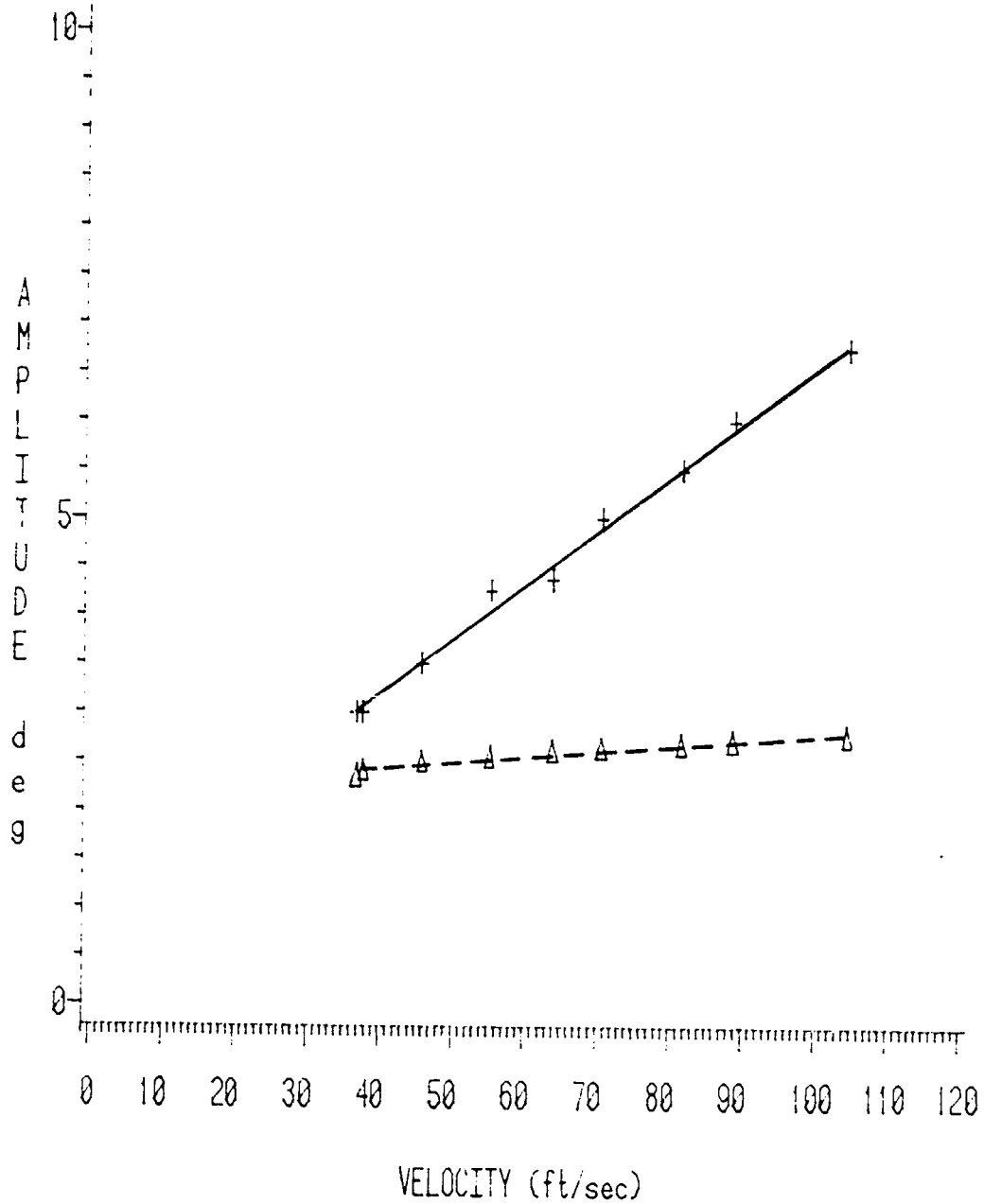
a.

FIGURE 25: Comparison between PSU experimental amplitude values and values predicted with the UTRC program.

Elastic Axis=0.250c

Natural Frequency=2.10 Hz

Initial Angle of Attack=14.0 Degrees

ZETA=0.01050

— + — Experimental

--△-- Predicted

VELOCITY (ft/sec)

b.

FIGURE 25: (cont.).

FIGURE 25: (cont.).

Elastic Axis=0.250c
Natural Frequency=4.28 Hz
Initial Angle of Attack=11.0 Degrees
ZETA=0.00427

— + — Experimental
--△-- Predicted

VELOCITY (ft/sec)

d.

FIGURE 25: (cont.).

Elastic Axis=0.250c   — + — Experimental

Natural Frequency=1.85 Hz   --△-- Predicted .

Initial Angle of Attack=11.0 Degrees

ZETA=0.00994

a.

FIGURE 26: Comparison between PSU experimental frequency values and values
predicted with the UTRC program.

Elastic Axis=0.250c
Natural Frequency=2.10 Hz
Initial Angle of Attack=14.0 Degrees
ZETA=0.01050

— + — Experimental
--△-- Predicted .

VELOCITY (ft/sec)

b.

FIGURE 26: (cont.).

Elastic Axis=0.250c

Natural Frequency=3.08 Hz

Initial Angle of Attack=12.5 Degrees

ZETA=0.00473

— + — Experimental

--△-- Predicted

VELOCITY (ft/sec)

c.

FIGURE 26: (cont.).

Elastic Axis=0.250c

Natural Frequency=4.28 Hz

Initial Angle of Attack=11.0 Degrees

ZETA=0.00427

—+— Experimental

--△-- Predicted

VELOCITY (ft/sec)
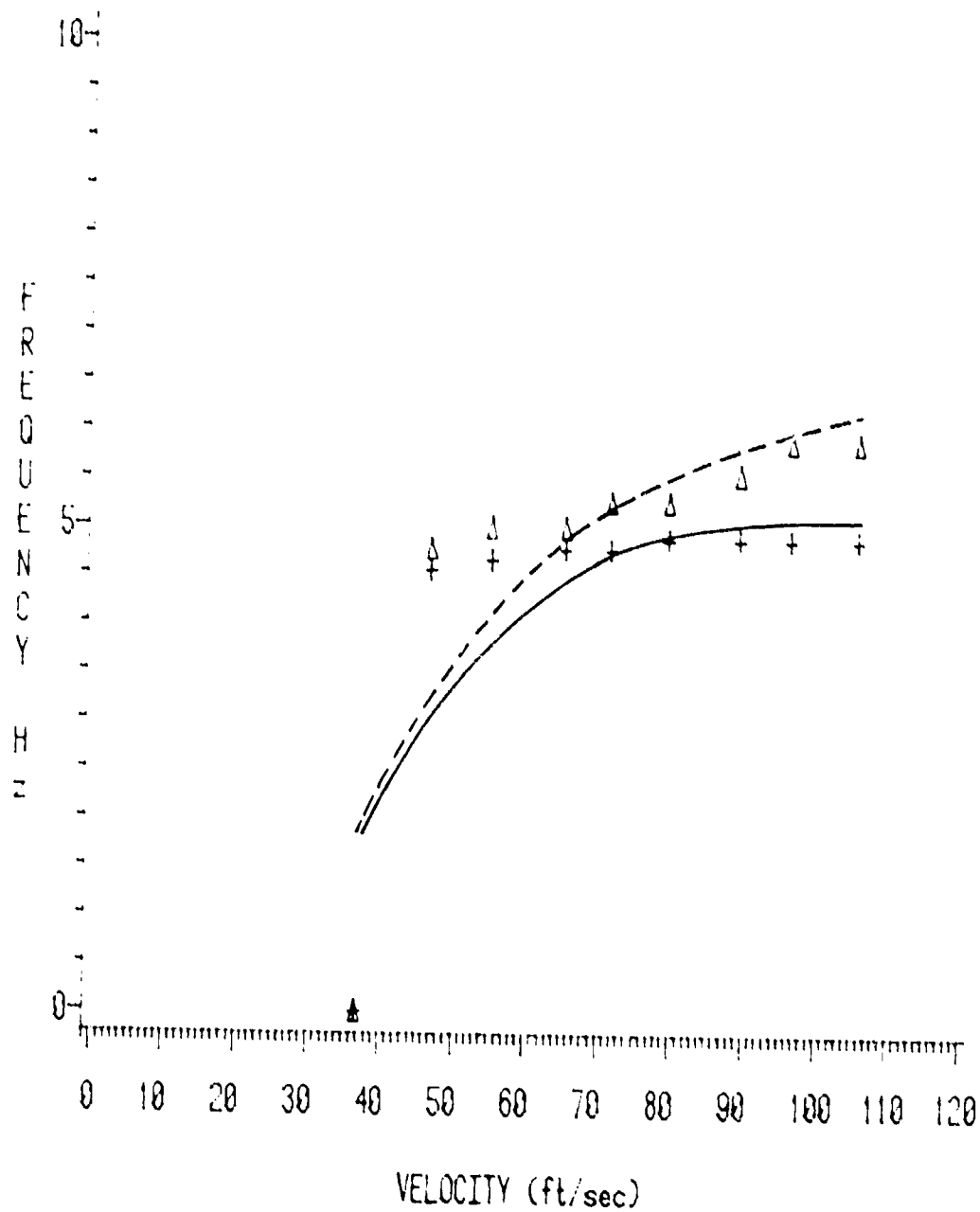
d.

FIGURE 26: (cont.).

Elastic Axis=0.250c

Natural Frequency=2.55 Hz

Initial Angle of Attack=14.0 Degrees

ZETA=0.13

— + — Experimental
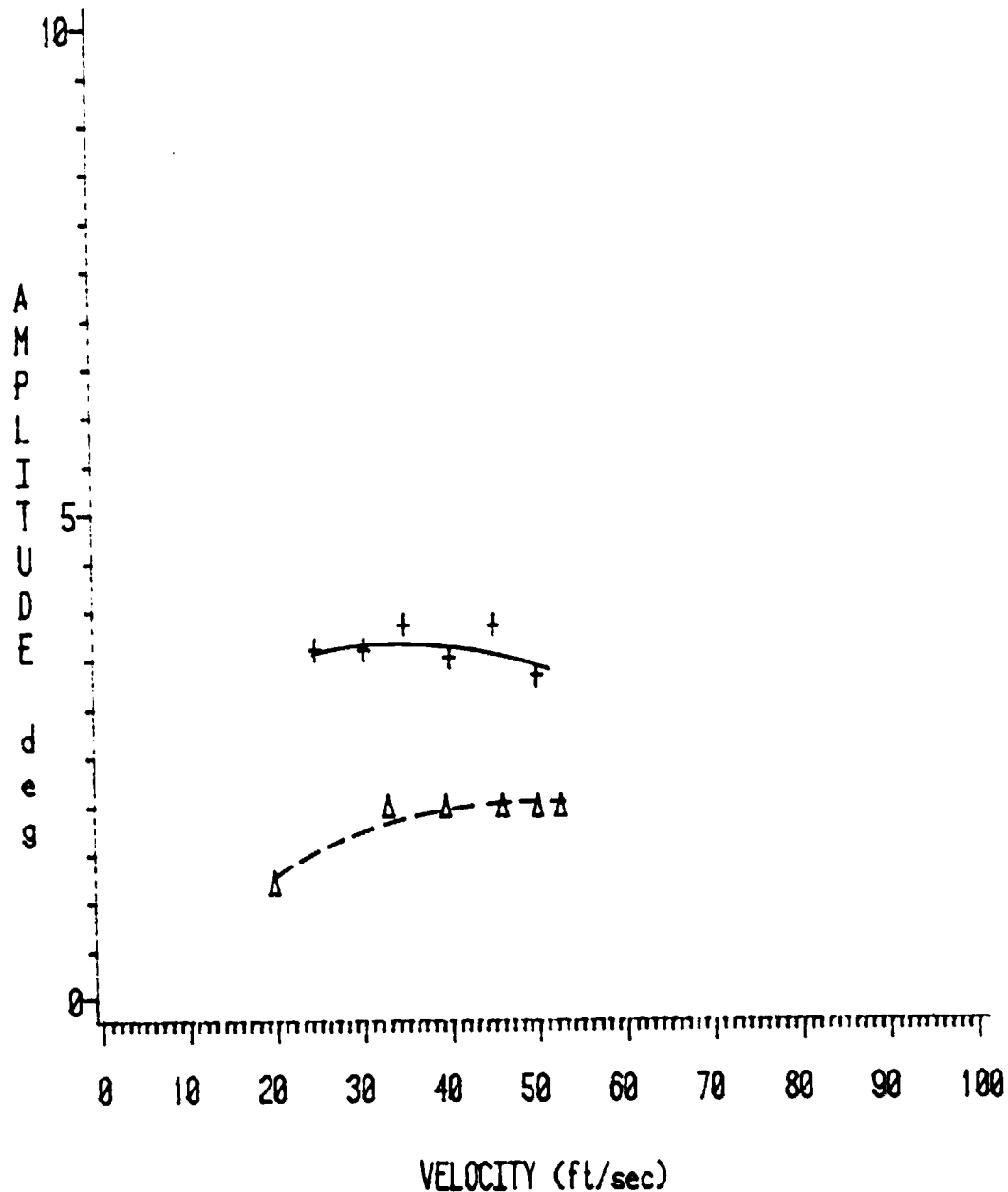
--△-- Predicted

a.

FIGURE 27: Comparison between MIT experimental amplitude values and values predicted with the UTRC program.

Elastic Axis=0.250c   — + — Experimental

Natural Frequency=2.55 Hz   --∆-- Predicted .

Initial Angle of Attack=14.0 Degrees

ZETA=0.13
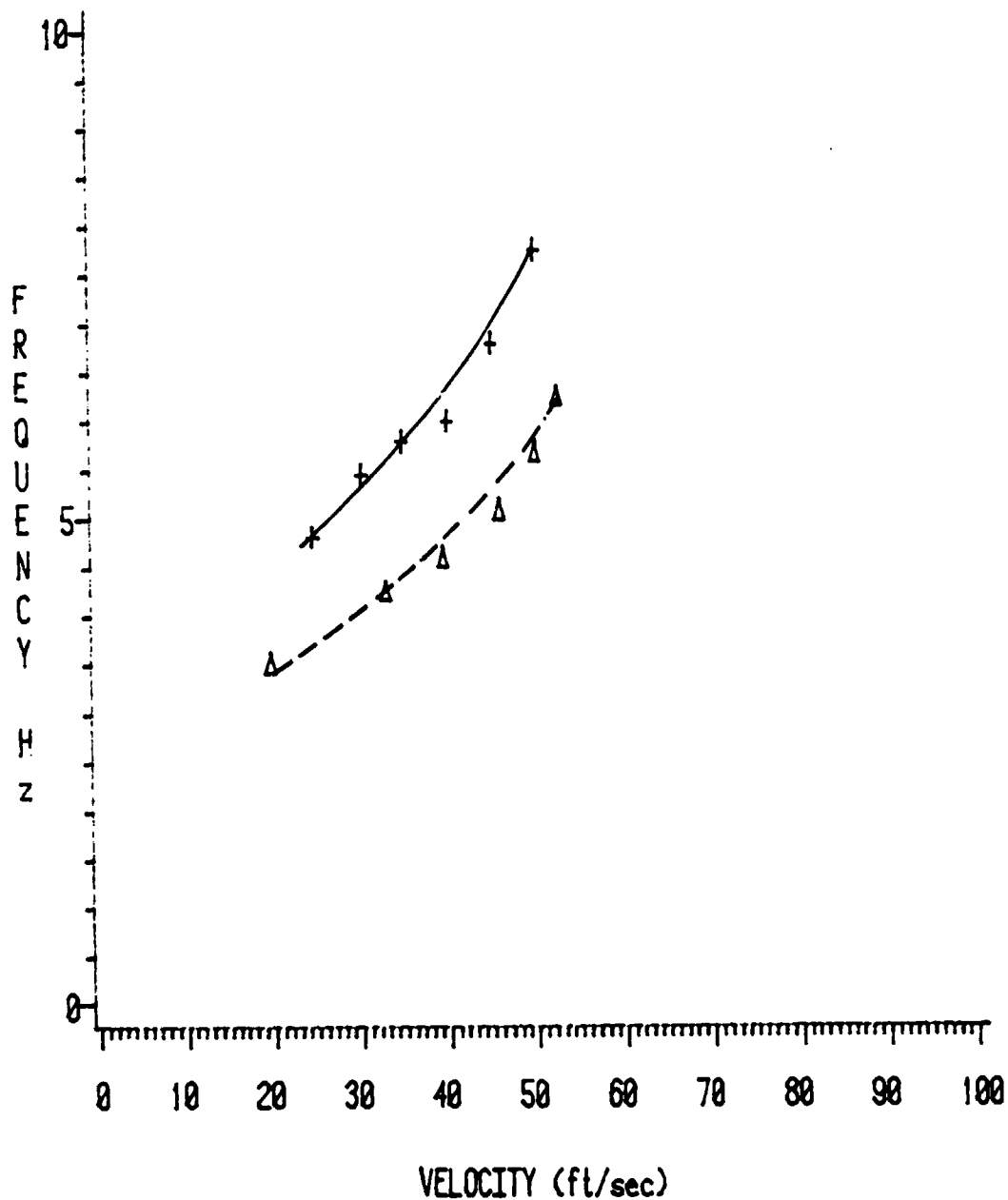
FIGURE 27: (cont.).

(Figure 28). However, in contrast to 1/4 chord results, program amplitude predictions overestimate experimental values. Finally, frequency values are predicted almost exactly, as shown in Figure 29.

Experimental oscillation amplitudes about the 50.0% chord elastic axis are so large that predictions calculated at only the lowest velocities, yielding the smallest amplitudes, are in bounds.

Prediction of stall flutter onset was good in some cases and not so good in others. In most cases, predicted stall flutter did not begin on its own unless the experimental flutter did (ie., unless experimental stall flutter began without having to tap the wing), and vice-versa. Most of the discrepancies were encountered when predicting the angle to which the wing had to be tapped. For instance, a fairly good prediction

TABLE IV. FLUTTER ONSET PREDICTION				
VELOCITY (ft/sec)	β_{i-e} (deg)	WING RESPONSE (experimental)	β_{i-p} (deg)	WING RESPONSE (predicted)
37.3	-4.5	FLUTTER	-4.5	FLUTTER
50.1	-3.5	FLUTTER	-3.5	FLUTTER
63.8	-2.0	FLUTTER	-2.0	FLUTTER

is shown in Table IV. Here, it is found that, when β_{i-p} was set equal to β_{i-e}, self-sustained stall flutter occurred, whereas, without this β_{i-p} angle, no flutter occurred. A poor prediction is illustrated in Table V. Gross inconsistencies exist here. Notice, that at 46.3 ft/sec

Elastic Axis=0.375c

Natural Frequency=3.81 Hz

Initial Angle of Attack=7.0 Degrees

ZETA=0.00679

— + — Experimental

--△-- Predicted .

VELOCITY (ft/sec)
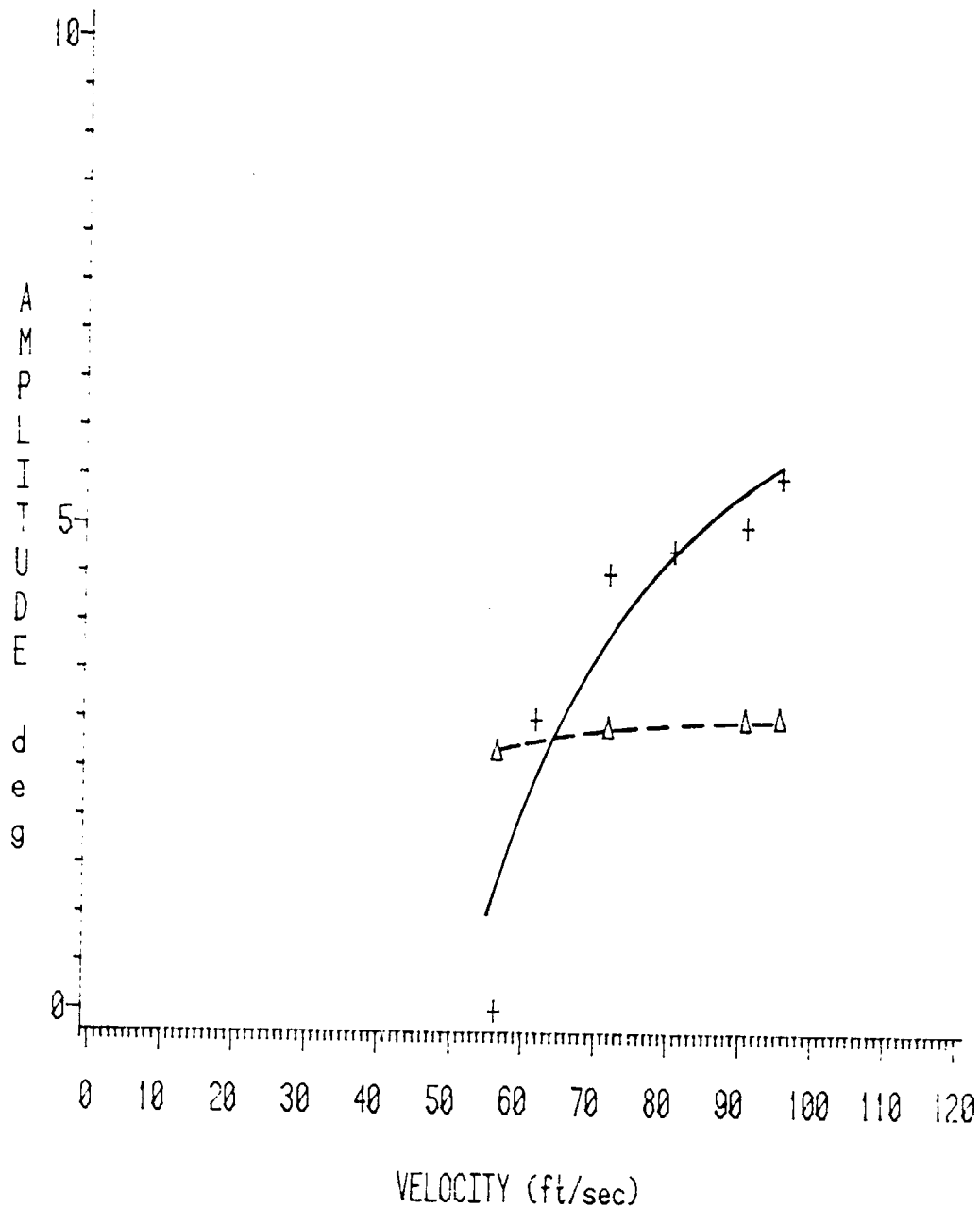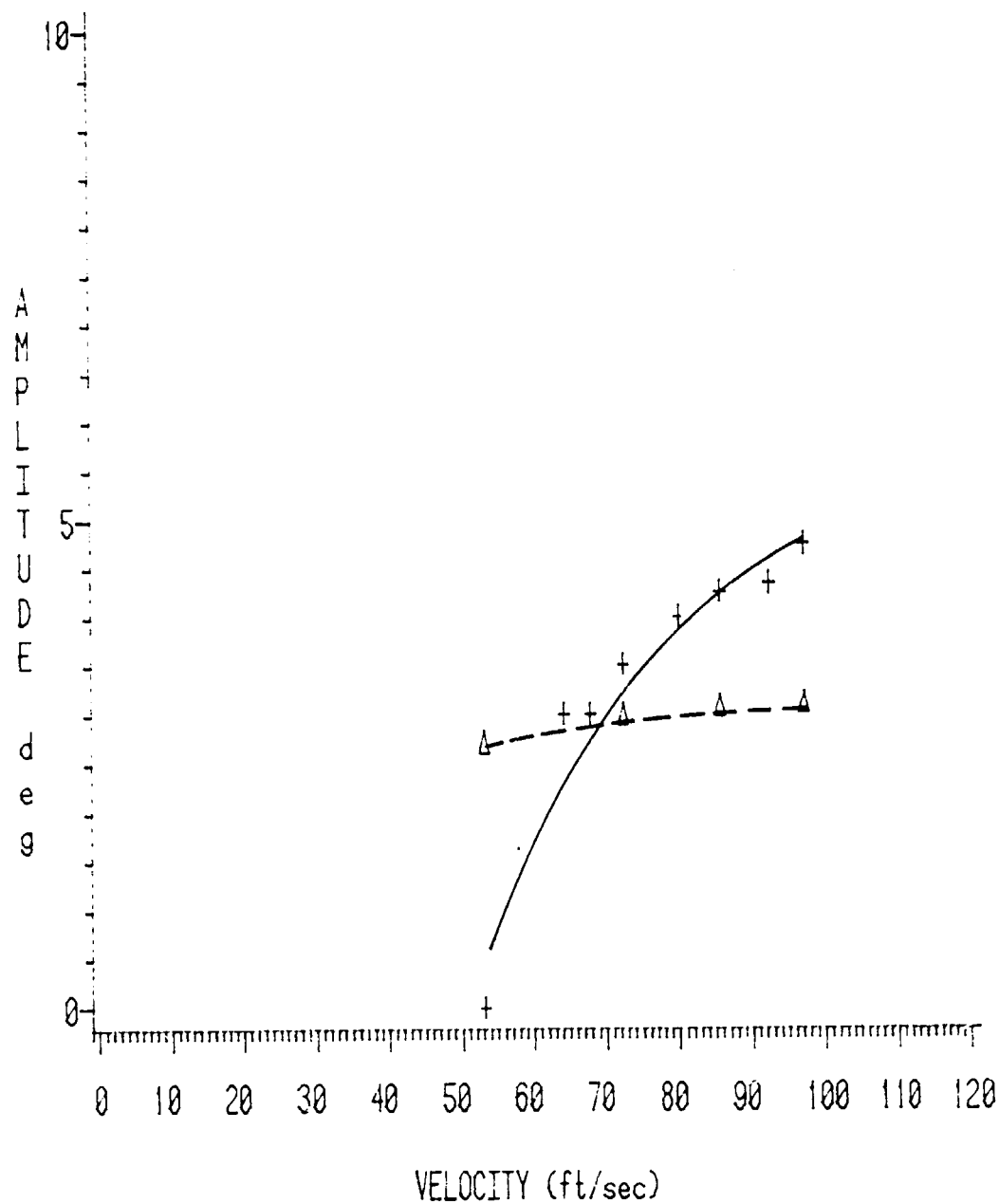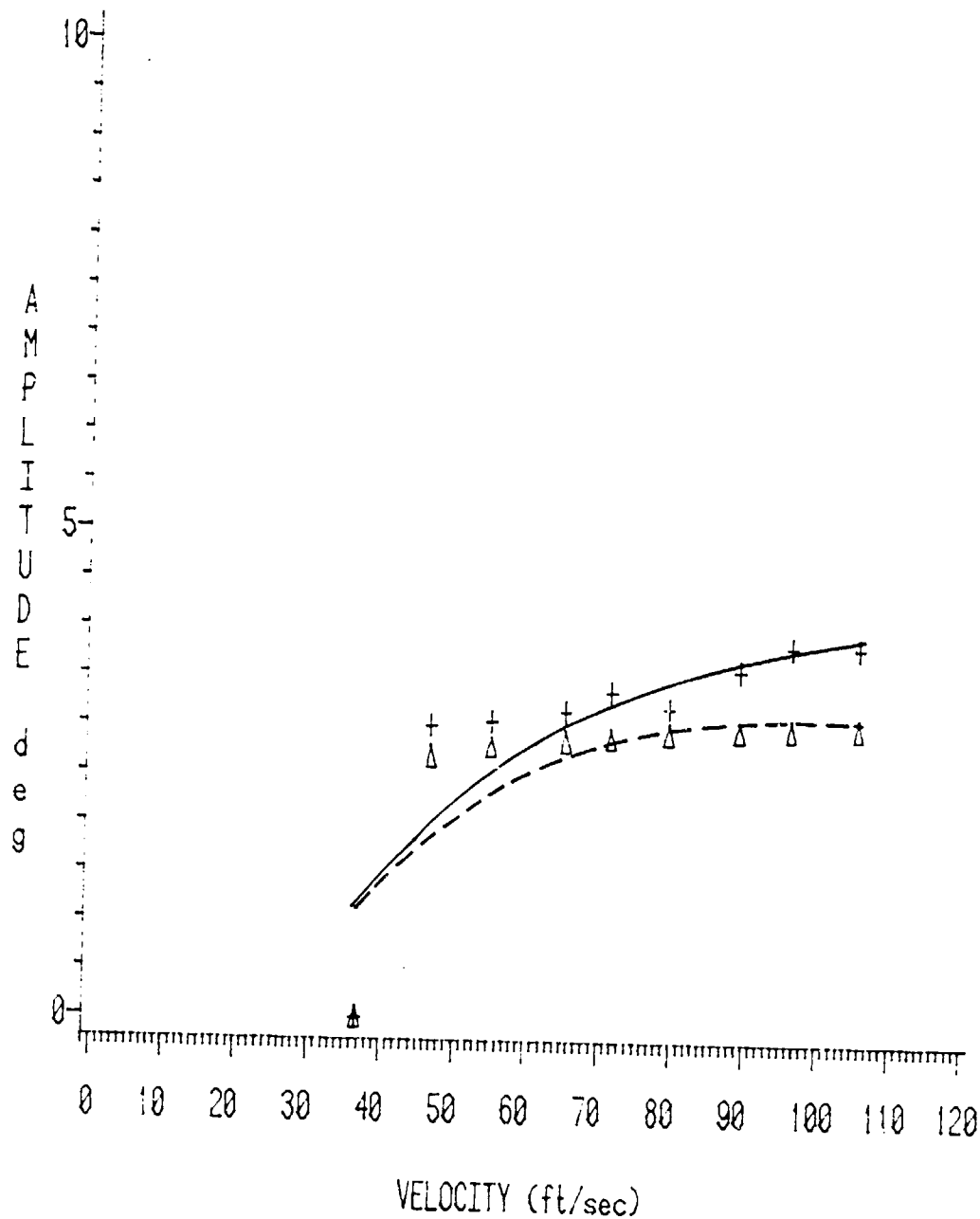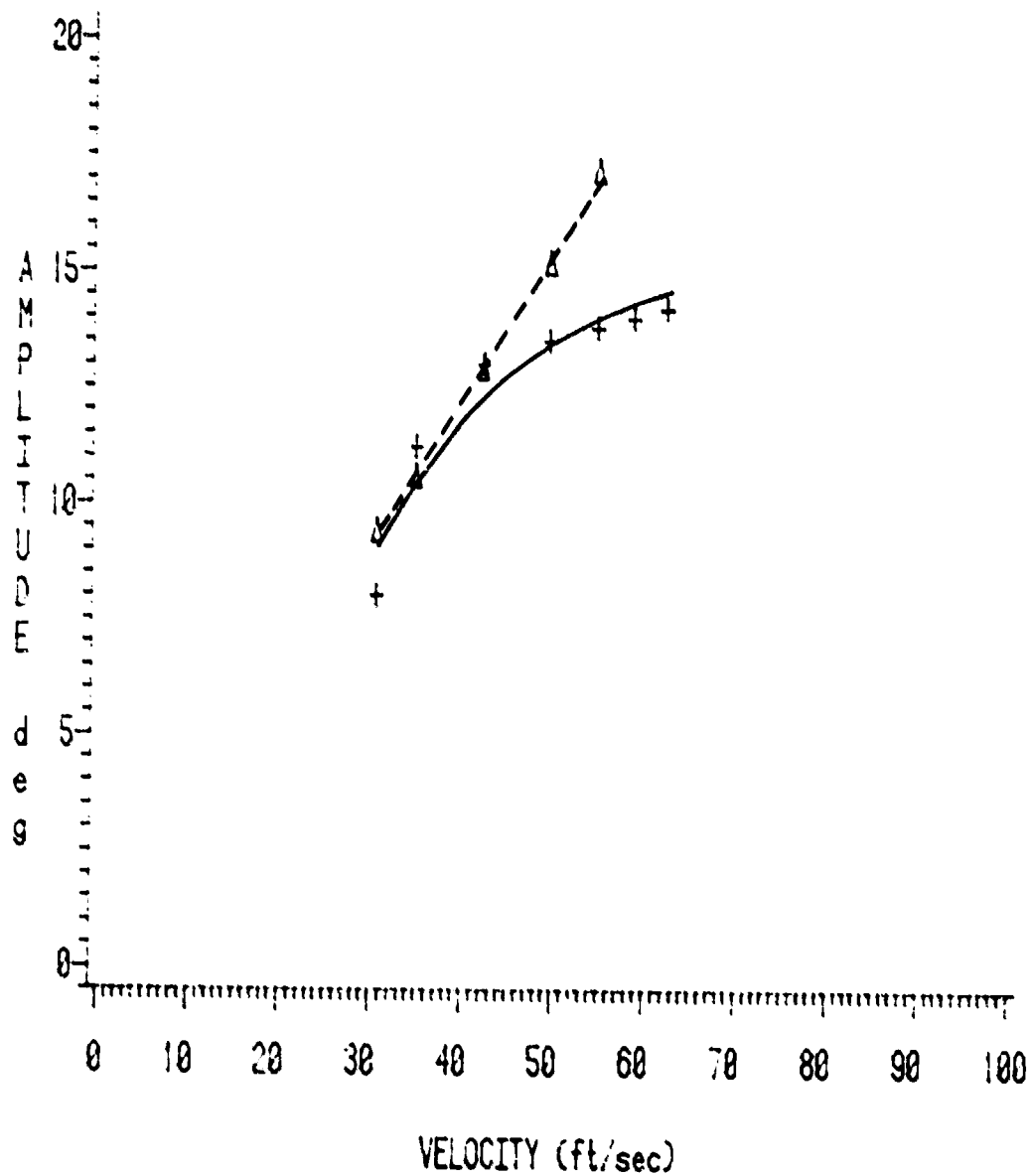
a.

FIGURE 28: Comparison between PSU experimental amplitude values and values predicted with the UTRC program.

Elastic Axis=0.375c   _ + _ Experimental

Natural Frequency=5.50 Hz   --Δ-- Predicted .

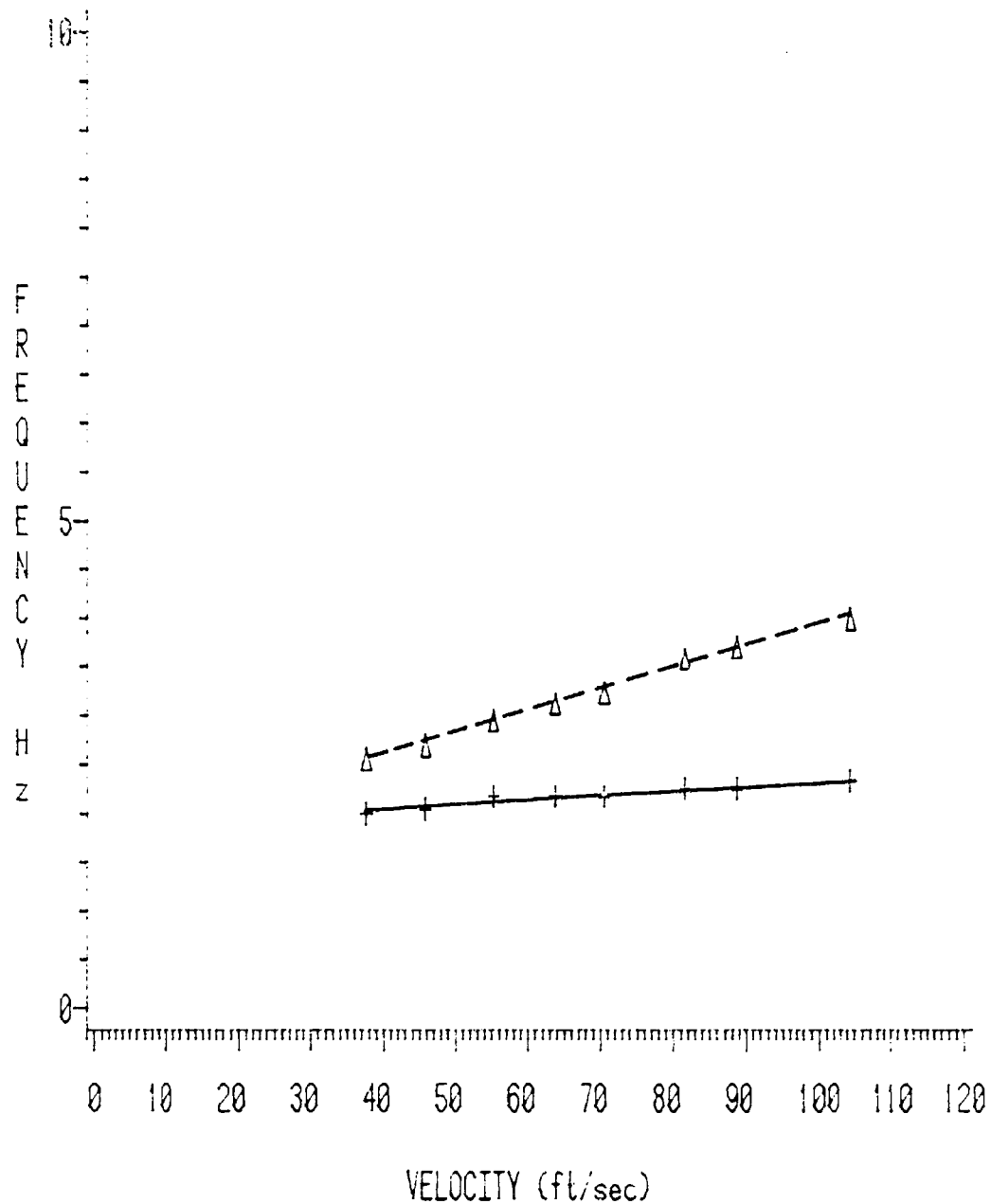Initial Angle of Attack=4.8 Degrees

ZETA=0.00628

VELOCITY (ft/sec)

b.

FIGURE 28: (cont.).

Elastic Axis=0.375c
Natural Frequency=5.83 Hz
Initial Angle of Attack=10.5 Degrees
ZETA=0.00888

— + — Experimental
--△-- Predicted .

VELOCITY (ft/sec)

c.

FIGURE 28: (cont.).

Elastic Axis=0.375c
Natural Frequency=6.00 Hz
Initial Angle of Attack=9.0 Degrees
ZETA=0.00502

— + — Experimental
--Δ-- Predicted
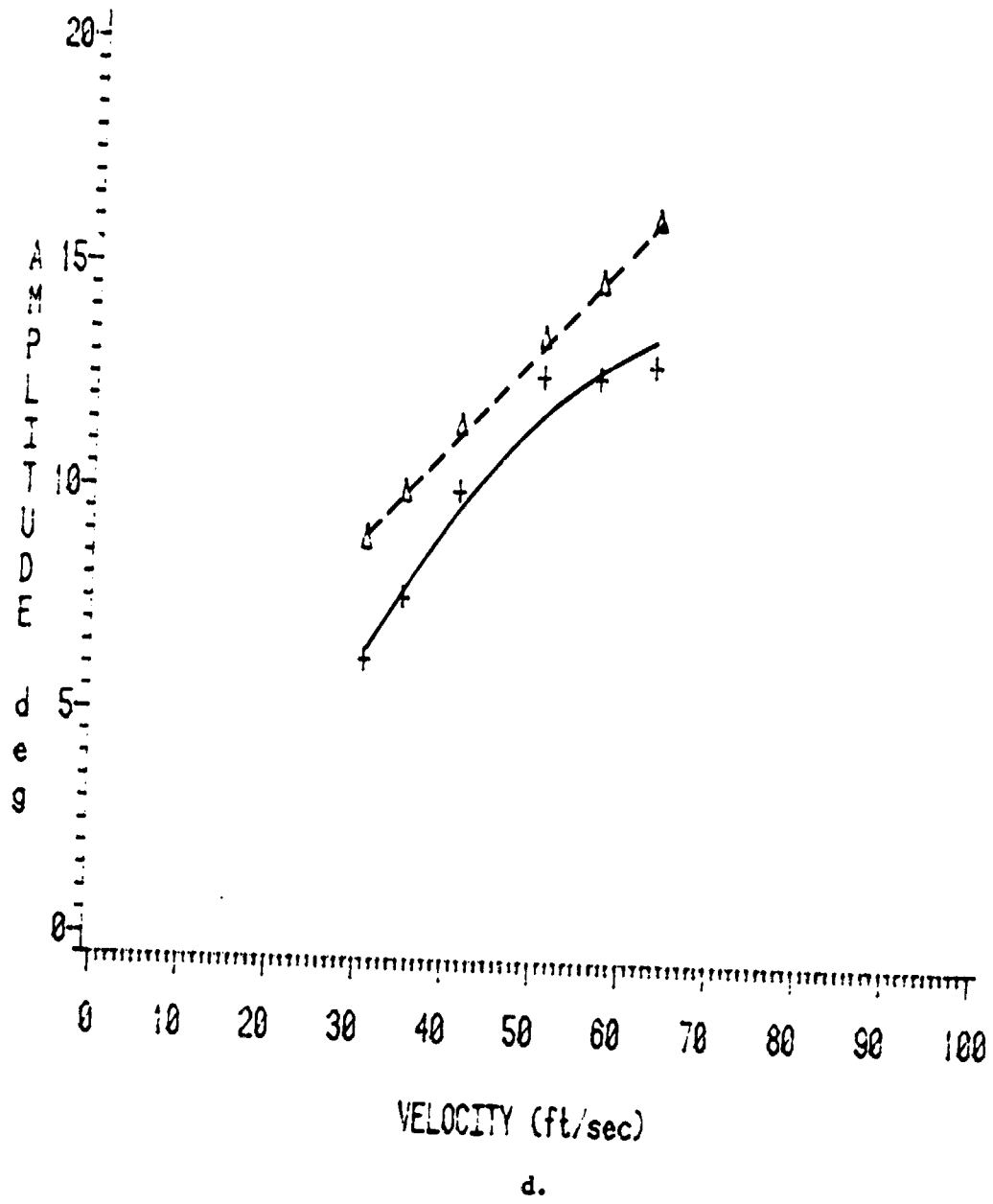
VELOCITY (ft/sec)

d.

FIGURE 28: (cont.).

Elastic Axis=0.375c

Natural Frequency=3.81 Hz

Initial Angle of Attack=7.0 Degrees
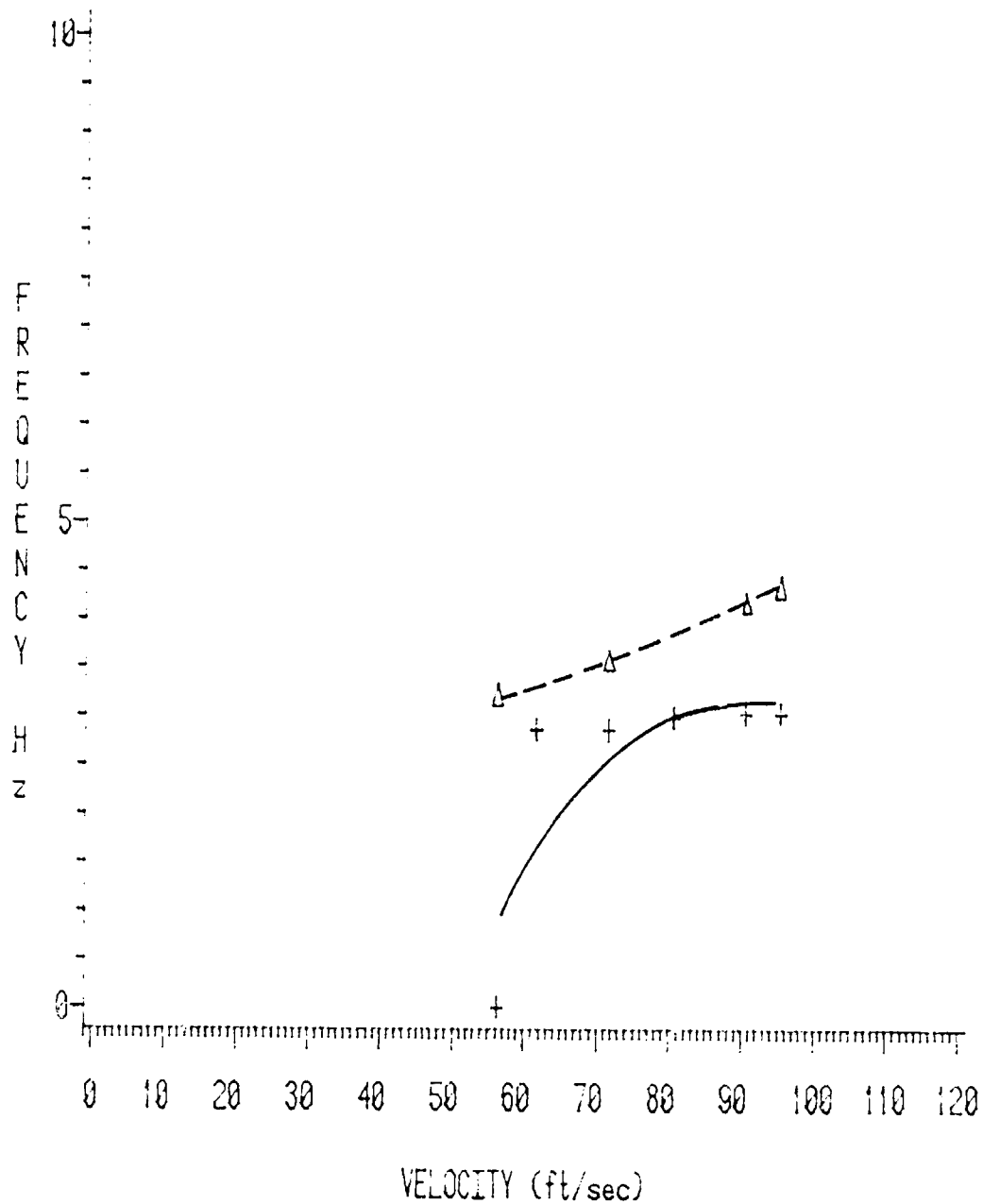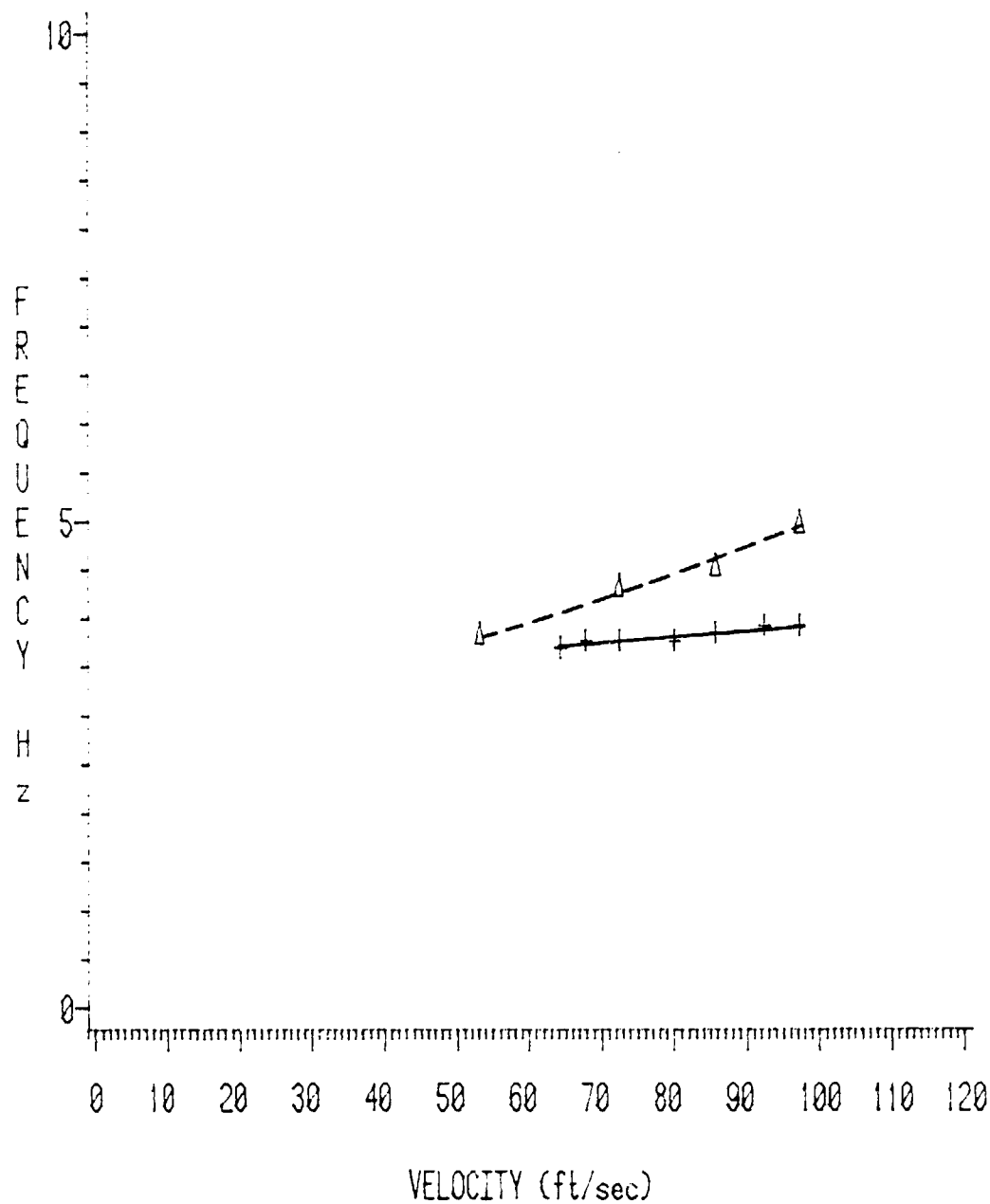
ZETA=0.00679

— + — Experimental

--Δ-- Predicted .
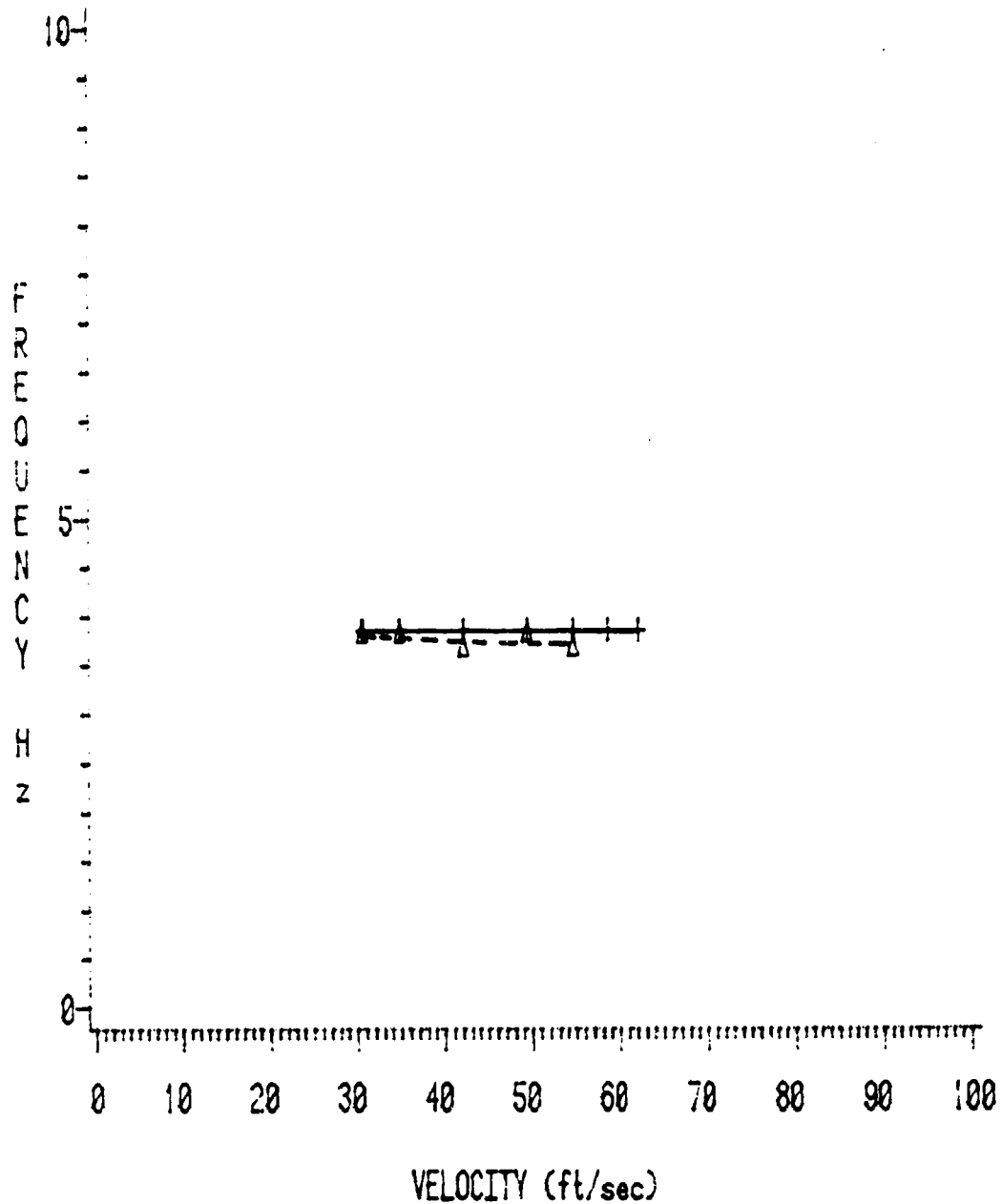
FIGURE 29: Comparison between PSU experimental frequency values and values predicted with the UTRC program.

Elastic Axis=0.375c

Natural Frequency=5.50 Hz

Initial Angle of Attack=4.8 Degrees

ZETA=0.00628

— + — Experimental

--△-- Predicted .

VELOCITY (ft/sec)

b.

FIGURE 29: (cont.).

Elastic Axis=0.375c
Natural Frequency=5.83 Hz
Initial Angle of Attack=10.5 Degrees
ZETA=0.00888

— + — Experimental
--Δ-- Predicted

VELOCITY (ft/sec)

c.

FIGURE 29: (cont.).

Elastic Axis=0.375c   — + — Experimental
Natural Frequency=6.00 Hz   --△-- Predicted
Initial Angle of Attack=9.0 Degrees
ZETA=0.00502

VELOCITY (ft/sec)

d.

FIGURE 29: (cont.).

		TABLE V. FLUTTER ONSET PREDICTION		
VELOCITY (ft/sec)	β_{1-e} (deg)	WING RESPONSE (experimental)	β_{1-p} (deg)	WING RESPONSE (predicted)
46.3	∞	NO FLUTTER	10.0	FLUTTER
55.1	5.5	FLUTTER	7.0	NO FLUTTER
69.5	5.5	FLUTTER	0.0	FLUTTER
89.3	6.0	FLUTTER	0.0	FLUTTER

the program predicted flutter with a β_{1-p} of only 10.0 degrees while the experiment showed no flutter at all, whereas at 55.1 ft/sec the program predicted no flutter with a β_{1-p} of 7.0 degrees while the experiment showed flutter with a β_{1-e} of only 5.5 degrees. Then, for the final two velocities the program predicts flutter without any tapping while, in the experiment, the wing had to be tapped to 5.5 degrees and 6.0 degrees, respectively. It should be noted that the program predicted the same limit cycle for all β_{1-p} that produced flutter.

Note, however, that there is a difference between the two ways of "tapping" the wing. In the experiment, the wing was actually tapped, and the maximum angle to which this tap would cause the wing to oscillate, β_{1-e}, was recorded. In the program, however, the wing was just "locked out" to an incidence angle, β_{1-p}, and then released.

Thus, the above comparisons are not entirely valid since the aerodynamic history of the experimental wing, before reaching β_{1-e}, was

unsteady, whereas the aerodynamic history of the computer wing, before reaching β_{1-p}, was steady. This would certainly have an effect, at least for a short time after the maximum angle of attack was reached, on the unsteady forces acting on the wing. This effect could, in some cases, be great enough to cause a discrepancy between predicted and experimental stall flutter onset.

Reasons for Inaccurate Predictions

The explanations for experimental and predicted flutter discrepancies to follow are qualitative, since the complicated nature of this problem makes a quantitative analysis virtually impossible. It is hoped that this discussion will aid the reader in understanding both the stall flutter phenomenon and the problems inherent in dynamic stall testing and prediction.

Experimental Measurement Error

A close look at experimental values and their error estimates reveals, immediately, that the discrepancies between them and predicted values is not due to experimental measurement error[*]. For instance, measurement error does not explain the fact that predicted data for oscillations about the 1/4 chord elastic axis are consistently low whereas predicted data for those about the 37.5% chord elastic axis are consistently high. Rather, one would expect a more "normally" distributed error. In addition, it gives no hint as to why the

----

[*]See Appendix B for error estimation.

amplitude slopes for the 1/4 chord elastic axis are never correctly predicted.

Inaccuracy in the Wing and
Wing-Support Construction

Due to the less-than-perfect fitting of the wing into the frame's wing supports, the wing was able to oscillate vertically with amplitudes of up to approximately 1.0 mm. MIT found that, when an airfoil was allowed both translational and torsional freedom during stall flutter, the airfoil oscillated vertically with amplitudes varying between 0.1 mm and 1.0 mm and that the torsional amplitude increased by roughly 2.0 degrees and showed a positive increase with respect to V_∞. Therefore, it is entirely possible that this seemingly insignificant free-play, which was strictly a mechanical error in the wing support, could have caused, at least in part, the differences between predicted and experimental amplitude data. However, this inaccuracy could not have been the only factor involved in causing these differences since MIT reports a positive $d\omega/dV_\infty$ value for this two-degree-of-freedom motion, whereas PSU finds a $d\omega/dV_\infty$ value equal to zero. Thus, this explanation remains only a possibility, at best, until further data is collected with this second degree-of-freedom completely eliminated.

Flow Interference due to the Frame
and Wing Supports

Free-stream flow interference caused by the proximity of the wing-support frame to the wing itself are estimated to be negligible. Tuft flow visualization showed that the large endplates eliminated any gross flow disturbances that may have been created by the frame's metal

bars.

The aluminum support bars and accelerometer attached to, and oscillating with, the wing may have changed the wing's static moment and drag characteristics enough to cause significant error. Since these attachments do not stall in the same manner as a NACA 0012 airfoil, the UTRC program could not properly correct for their presence. A better way to take this effect into account would be to substitute the static data of the wing, with endplates only, into the UTRC program and then to correct for support bar and accelerometer effects by adding these attachments' static C_N and C_M values to the wing's unsteady C_N and C_M values. In this way, the non-linear normal force and moment coefficient values peculiar to a dynamically stalling airfoil are calculated for the wing only, and any extra forces or moments due to other effects are merely added on.

Inaccurate Static Data

The recalculated static characteristics, mentioned in Chapter IV, did yield, for two recalculated cases, flutter predictions that were different from what has been reported herein. However, these differences do not significantly change original comparisons with experimental results. Furthermore, it is believed that the greater source of error is due to the manner in which the static data was used in the UTRC program, which is discussed in the previous paragraph, rather than to inaccurate data collection.

Tunnel Effects

Tunnel interference effects, present during the collection of the UTRC data base, could have altered the relationship between static and dynamic data especially since the UTRC two-dimensional tunnel has such a small test section height compared to the airfoil chord length. However, just how much of an effect this may have had is impossible to estimate since the difference between static and dynamic tunnel interference effects is currently unknown (4, 30).

Reynold's Number Effects

The low experimental Reynold's Numbers used in these tests of, 1.0×10^5, to 2.5×10^5 could have caused greater oscillation amplitudes about the 1/4 chord due to delayed boundary layer reattachment after stall. As stated in Chapter II, dynamic reattchment at a Reynold's Number of approximately 1.0×10^6 occured later than at a Reynold's Number of 2.5×10^6 and caused greater moment hysteresis and negative aerodynamic damping. It is, then, very possible that the low experimental values used in the PSU experiment, as compared to those used for the UTRC data base (9.6×10^5), could partly account for the experimental amplitude values being higher than those predicted by the UTRC program. However, this does not explain why predicted amplitudes underestimate experimental amplitudes obtained from the 1/4 chord elastic axis and overestimate those obtained from the 37.5% chord elastic axis.

Mach Number Effects

The previously unaccounted for discrepancy between 1/4 chord and 37.5% chord elastic axis data comparisons can be explained in terms of dynamic stall type and Mach Number effects. The UTRC data base was taken at a free-stream Mach Number equal to 0.325. This relatively high subsonic Mach Number would easily cause early, shock-induced flow separation and, therefore, prevent the airfoil from entering into deep dynamic stall. This would significantly alter the clockwise moment hysteresis loops for the oscillating airfoil, especially at large amplitudes where the force and moment overshoots can be large and where subsequent dynamic stall behavior is strongly dependent upon the powerful, shed vortex. In other words, the UTRC program may be predicting C_n and C_m values characteristic of light stall, when, in fact, at lower Mach Numbers, conditions would have yielded C_n and C_m values characteristic of deep stall. This is borne out also in the comparisons done in references 31 and 32. Generally, light stall will cause greater negative aerodynamic damping and, therefore, greater limit cycle amplitudes. Thus, the UTRC program would be expected to overpredict deep stall amplitudes. This is the case for oscillation amplitudes about the 37.5% chord. One would not expect this effect to be quite as pronounced for the 1/4 chord where light stall conditions prevail throughout.

Three-Dimensional Effects

Finally, it must be pointed out that large errors may result from the three-dimensional flow pattern over the wing. Figure 30 shows, roughly, how the wing stalled statically as visualized with tufts placed at the 12.5%, 25.0%, 37.5%, 50.0% and 62.5% chords. The stall regions are inside of the thin, black lines. It can be seen that the wing stalls inboard first and that this stall gradually moves outboard along the span. This is indicative of varying downwash along the span, characteristic of three-dimensional wing stall.

In this study, the three-dimensional static characteristics were substituted into a program designed for a two-dimensional airfoil. It is quite possible that this program cannot accommodate such a substitution. Perhaps better results would be obtained if the wing's two-dimensional static characteristics were used in the program, and the three-dimensional effects were taken into account by using a strip analysis of the wing.

x/c=0.0

α=10.0°

x/c=1.0

α= 11.0°

α=11.5°

α=12.0°.

α=12.5°
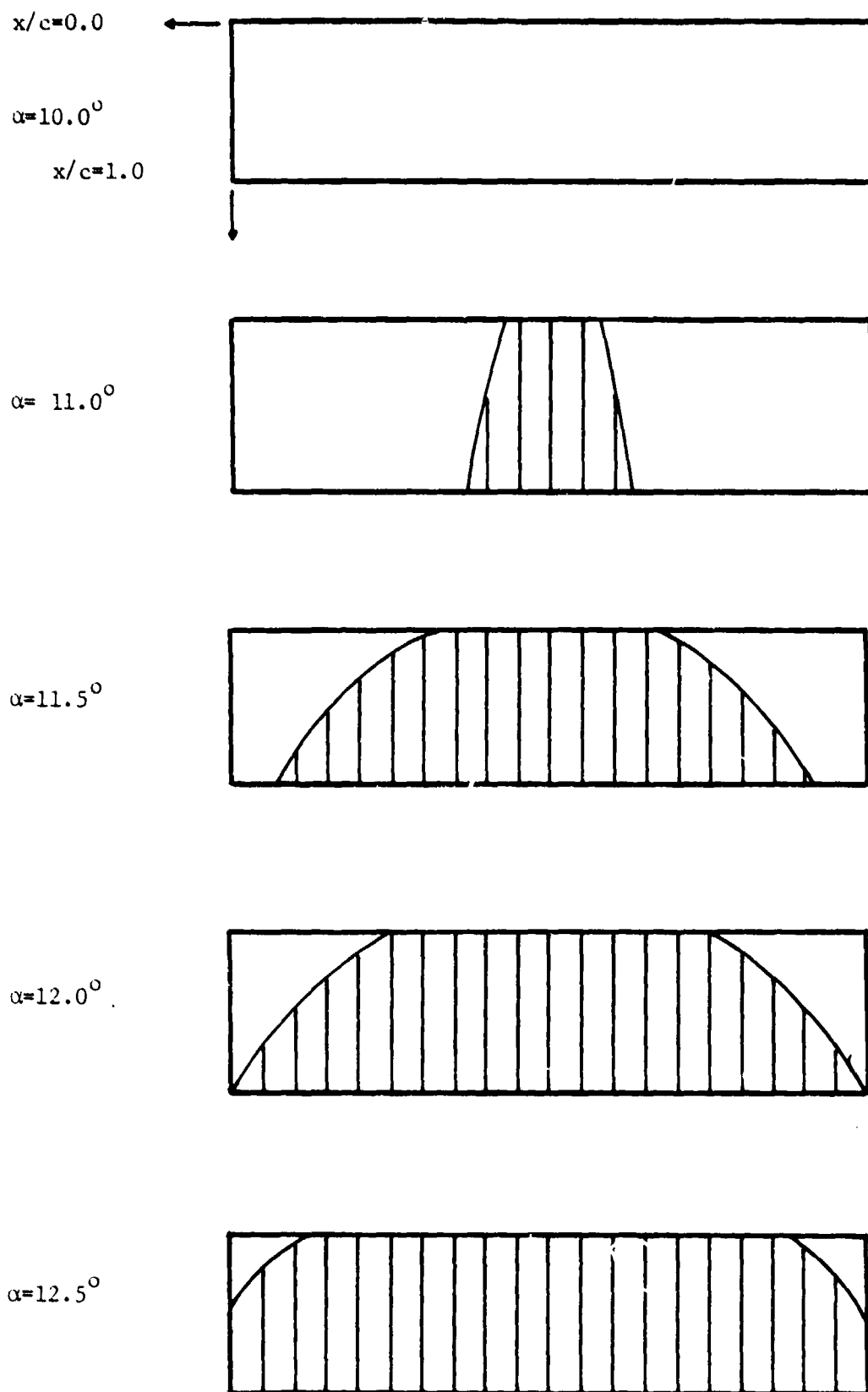
FIGURE 30: Three-dimensional stall pattern and washout angles for the PSU wing.

CHAPTER VI

CONCLUSIONS AND RECOMMENDATIONS

Conclusions

In light of the comparisons between predicted and experimental stall flutter data and taking the dynamic stall characteristics into consideration, the following conclusions are drawn:

1. The empirical prediction method developed at UTRC yields reasonably accurate values for unsteady, non-linear C_n and C_m for a NACA 0012 airfoil undergoing dynamic stall.

2. This program, coupled with an accurate dynamics subroutine, produces fair estimates of stall flutter amplitude and frequency variation with respect to free-stream velocity for a NACA 0012 wing section undergoing torsional stall flutter.

3. The large percentage differences between predicted and experimental data are probably due to differences between test conditions of the PSU experiment and those of the data base rather than to program inaccuracies or random, experimental, measurement error. These differences include Reynolds and Mach Number effects, tunnel interference, vertical oscillations of the wing, wing-support bar and accelerometer interference effects and three-dimensional flow effects.

4. The best empirical prediction method for a given airfoil is one which is derived from a data base most closely representing the dynamic stall type and unsteady conditions that the airfoil in question will experience.

Recommendations

Recommendations for further study are as follows:

1. Reconstruct the wing support so that no vertical free-play is possible.

2. Increase test Reynolds Numbers to correspond to those of the UTRC Program data base, 9.6×10^5, either by increasing the chord length or by using a trip-wire to increase turbulence over the wing surface[*]. This may decrease C_m vs. α hysteresis and reduce flutter amplitudes about the 1/4 chord.

3. Attempt to account for low Reynolds Number effects by including static hysteresis data in the program data input.

4. Eliminate all three-dimensional effects by doing the static tests in a two-dimensional tunnel and then accounting for three-dimensional effects by applying the computer code in a strip analysis along the wing span.

---

[*]According to reference 24, this should not have a gross effect on the type of dynamic boundary layer separation that the NACA 0012 experiences.

5. Account for effects on flutter predictions due to the aluminum, wing-support bars and accelerometers in the following way: substitute the static C_N and C_M characteristics for the wing, with endplates only, into the UTRC Program, and then add the static C_N and C_M values of the aforementioned attachments to the unsteady normal force and moment coefficients of the wing.

APPENDIX A

TORSIONAL SPRING CONSTANT, INERTIA
AND DAMPING RATIO MEASUREMENT

Torsional Spring Constant

Torsional springs used in this experiment were constructed using a varying number of translational springs connected to the wing via two aluminum support bars, as described in Chapter IV. All were linear over the range of experimental oscillation amplitudes. Thus, the overall torsional spring constant was calculated by measuring the individual translational spring constants and by multiplying those values by the square of the moment arm. That is, the torque on the wing, T, is given by the equation (Figure A-1):

$$T = F x R$$

Expressing this in terms of the translational spring constant, K_T, and assuming that each spring stretches by a value equal to that subtended by the circular arc, s, yields the following equation:

$$T = K_T R^2 \theta^2$$

This approximation yields only a 1.0 percent error for an oscillation amplitude, $\Delta\alpha$, of 20.0 degrees. Then, of course, K was calculated using the equation

$$K_\theta = \frac{T}{\theta} = K_T R^2$$
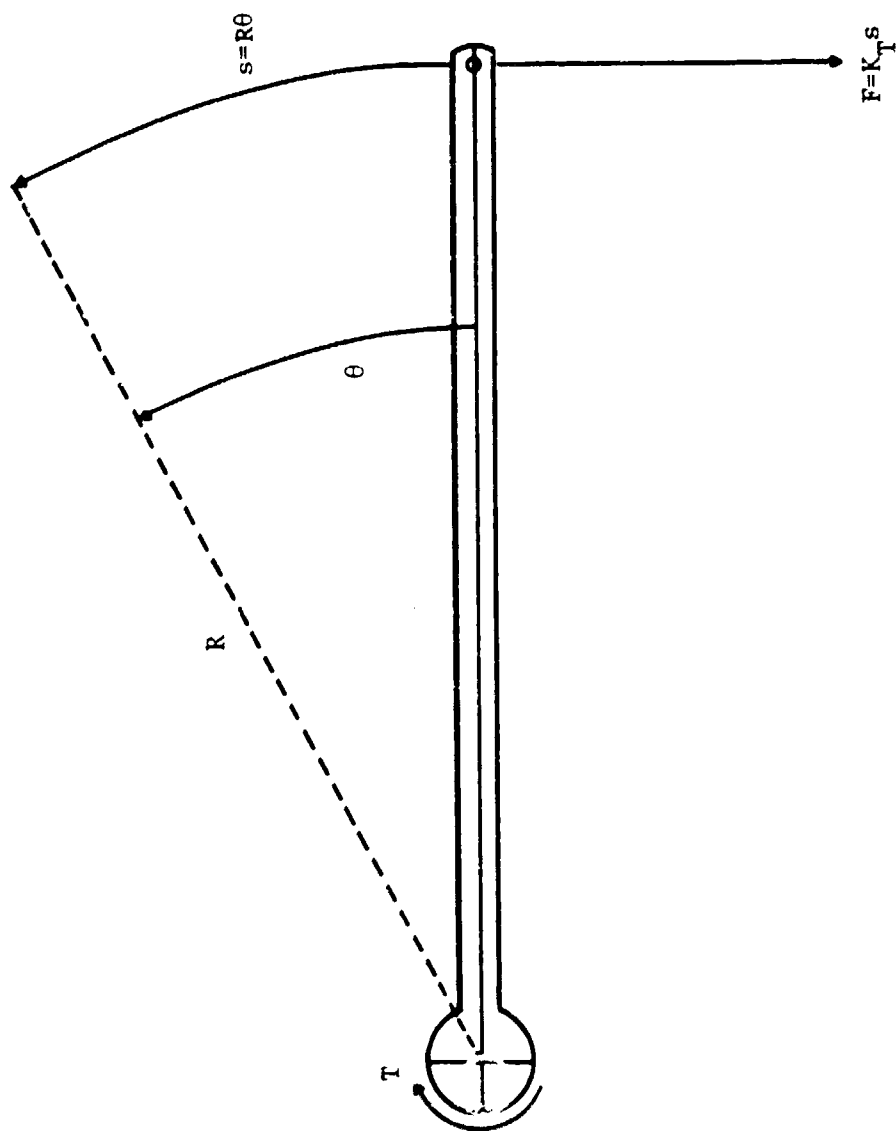
FIGURE A-1: Definition of force and moment variables.

Inertia

Wing inertial values, which varied for different elastic axes, were calculated using the relationship

$$I = \omega_d^{\,2}/K_\theta$$

Now, ω_n was assumed to be equal to ω_d because of the very low system damping, ζ (see next section). Thus, I was calculated by substituting ω_d, which was measued with the aid of the oscilloscope both before and after each experimental run, into the above equation. These values were then averaged over all runs for each configuration and it was these final averages that were used in the UTRC program input.

Damping Ratio

Before and after each experimental run, the wing was "locked out" to an angle approximately ten degrees above its equilibrium position. It was then released, and the attenuation curve was constructed from the oscilloscope (Figure A-2) by recording peak acceleration values as the wing underwent its damped oscillations. These peaks were then normalized and curve fitted, as in Figure A-3, for each different wing inertia used in the experiment, according to the equation,

$$y/y_o = e^{-\zeta \omega_n t}$$

$y(t)$

y_o

$e^{-\zeta\omega_n t}$

$y(t)=y_o \dfrac{e^{-\zeta\omega_n t}}{\sqrt{1-\zeta^2}} \sin\omega_d t \cong y_o e^{-\zeta\omega_n t} \sin\omega_n t$

y_{p2}

y_{p1}

y_{p3}

t

FIGURE A-2: Attenuation curve.
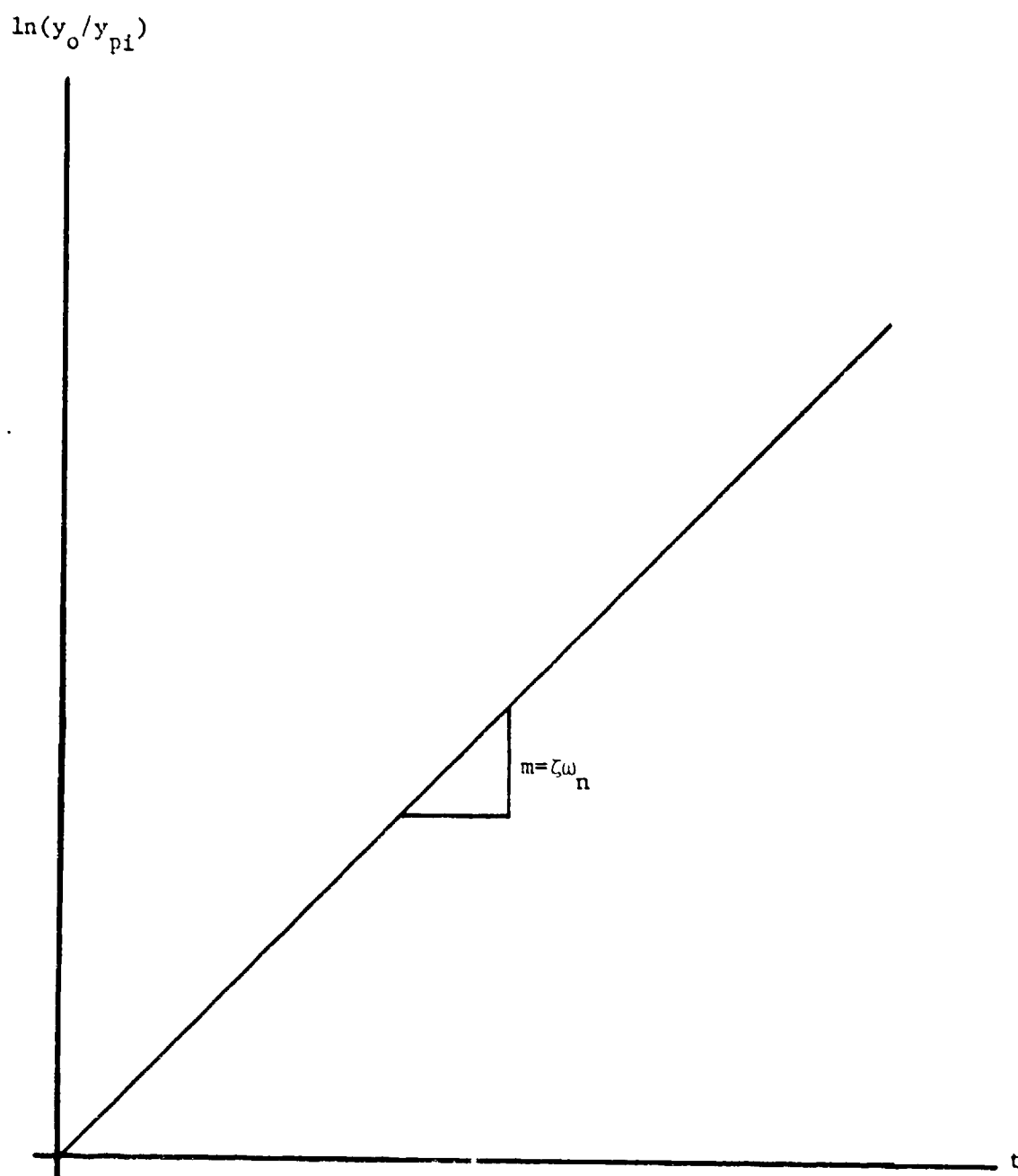
FIGURE A-3: Logarithmic graph of attenuation peaks.

This was done, with PSU's statistical program, MINITAB, using a linear least-squares method. The final value of ζ was calculated using the equation
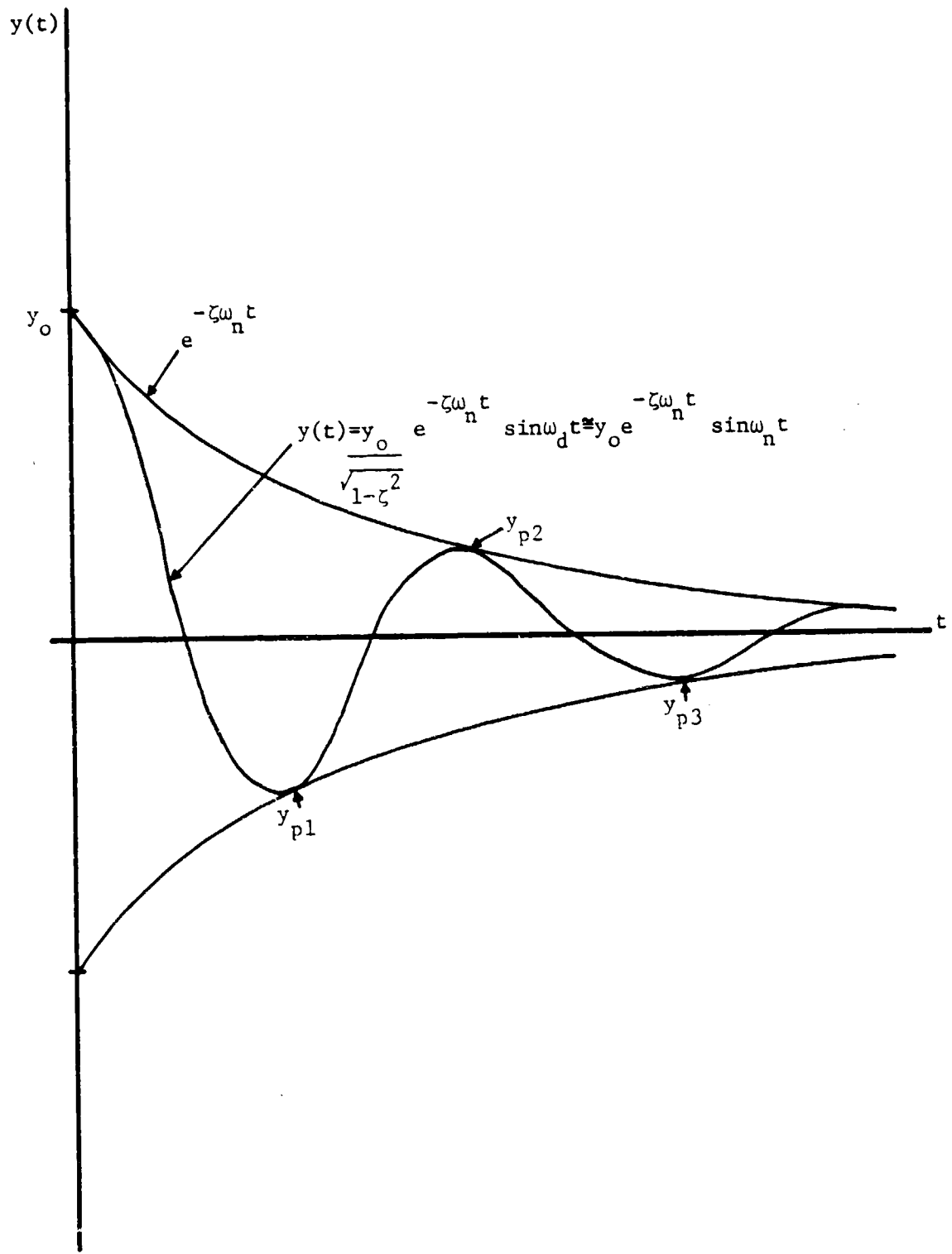
$$\zeta = m/\omega_n.$$

APPENDIX B

ACCELEROMETER CALIBRATION AND MEASUREMENT
ERROR ESTIMATE

Accelerometer Calibration

The Endevco 2233 Accelerometer was calibrated as a function of torsional oscillation amplitude and frequency. The acceleration of a point P (Figure B-1) undergoing sinusoidal, constant amplitude oscillations at a distance, R, from the center of rotation is given by the following equation:

$$\ddot{s}_p = -R\Delta\alpha\omega^2 \sin\omega t.$$

It immediately follows that the maximum absolute value of the acceleration at this point is

$$|\ddot{s}_p| = R\Delta\alpha\omega^2$$

and, therefore, that the amplitude of this oscillation is

$$\Delta\alpha = |\ddot{s}_p|/R\omega^2.$$

The next logical step would be to calibrate the accelerometer such that its voltage output could be directly correlated to an acceleration, in ft/sec^2, and to apply this information to the above equation. This value, coupled with the known radius, R, and frequency of oscillation, ω, would make it possible to calculate the angular amplitude. However, another method was chosen, due to difficulties encountered in accurately reproducing low frequency, sinusoidal

-113-

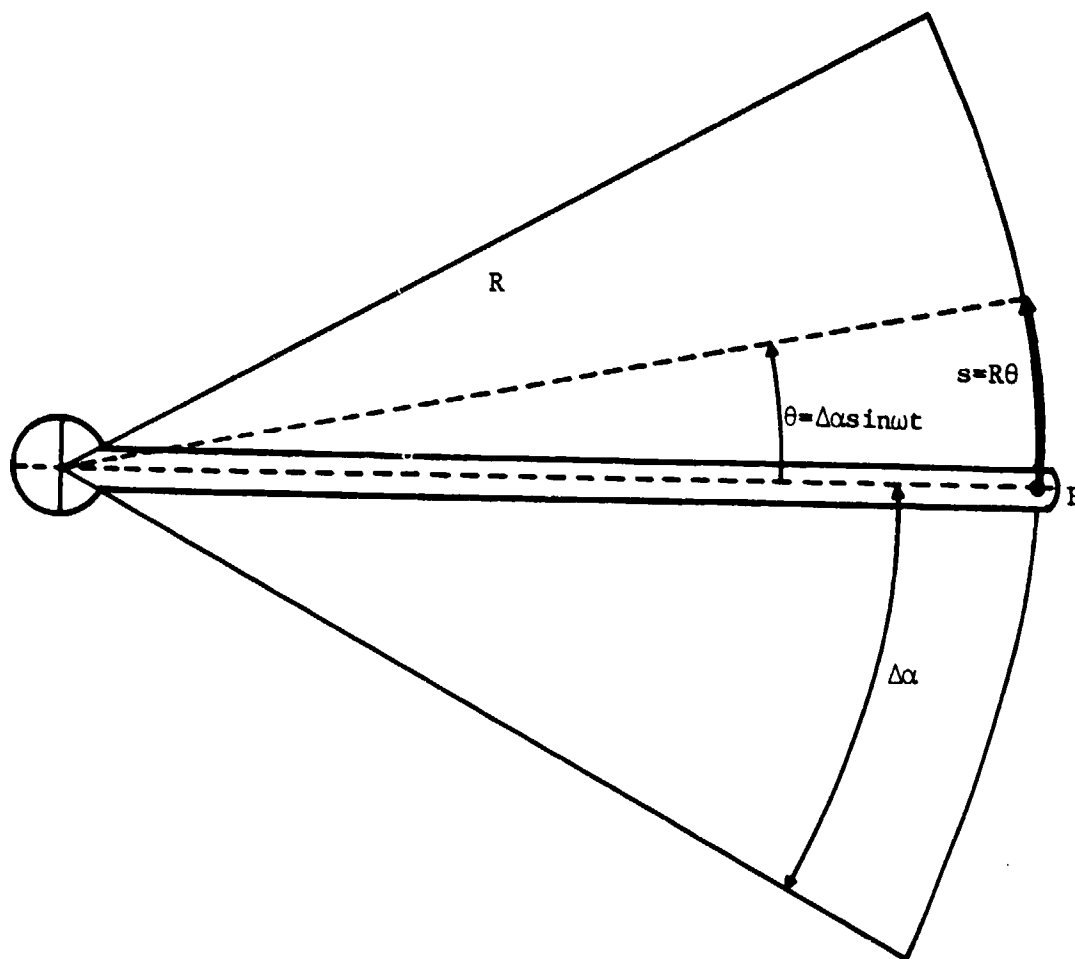FIGURE B-1: Definition of angular acceleration variables.

vibrations, necessary to making this corrrelation. Sixty six data points, which gave accurate and consistent visual amplitude and "electrical" acceleration values (from the accelerometer output), were graphed as in Figure B-2. The vertical axis represents oscillation amplitude and the horizontal axis represents peak-to-peak linear acceleration, expressed in volts, divided by the square of the frequency of oscillation, expressed in cycles per second. These points were curve fitted using a linear least-squares, regression line[*]. Thus, to find oscillation amplitudes for any given data point, the accelerometer amplitude output was divided by the square of its frequency and matched, by the calibration line, to a particular angular amplitude.

Error Estimation

Certain amplitude measurement problems were encountered during data collection. During the course of the experiment, certain test configurations showed highly erratic accelerometer readings. These occured either when the flutter amplitude and frequency were so low that random low frequency noise was of the same order of magnitude as the acceleration or when these dynamic variables were so high that they, along with random noise input, overloaded the amplifier. In cases like these, visual observation was the only possible means of calculating amplitude, and no means of accurately calculating frequency was available. However, these incidents were the exception and not the

----

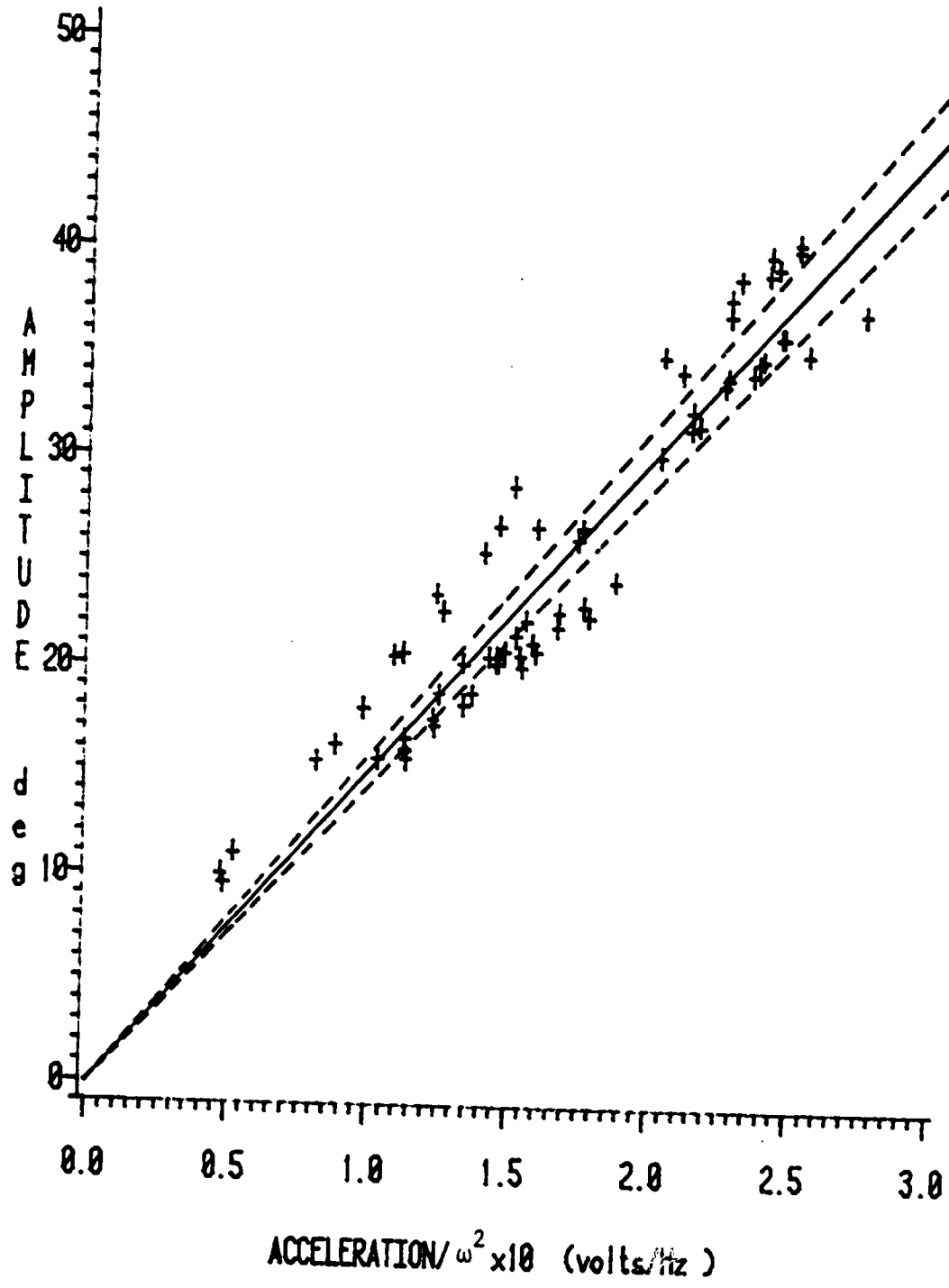[*]The linearity assumption is valid since the frequencies only ranged from zero to six hertz.

FIGURE B-2: Accelerometer calibration curve.

rule. Most of the configuratiions tested yielded fairly good correlation between visual and accelerometer measurements. The calibration curve of Figure B-2 is made up of points for which this correlation was found to be exceptional. The scatter is most likely due to inaccuracies in reading both the amplitudes from the angular markings on the frame and the accelerometer's signals from the oscilloscope.

Statistically, however, this scatter is of little consequence. It has been calculated, using a PSU statistical program, MINITAB (33), that the correlation coefficient between the two graphed variables is 0.981. That is, 98.1% of the variation in $2\Delta\alpha$ about its mean, predicted from values of $2s/\omega^2$, is "explained" by the regression line. A correlation coefficient of 1.0 implies that all the points land right on the regression line. In addition, a 99.9% confidence interval for the line's slope, which equals 15.3 deg-cyc^2/sec^2, as calculated using a t-confidence table, is ± 0.64 deg-cyc^2/sec^2, assuming that the regression line runs through the origin. This means that one can be 99.9% confident that the slope of the line lies between the interval shown in Figure B-2. That translates to an error of only 4.2%.

This relatively small error was not, then, the major source of experimental uncertainty. The largest error contribution came either from the cases, where accelerometer readings were too erratic to record or where visual and accelerometer data did not fall to within 2.0 degrees of eachother (a very rare occurence). This two degree limit was

---

[*]This calculation is valid since the number of data points used, 66, is approximately 13% of the whole and 10.0% is required for validity.

estimated, rather arbitrarly by the author to be the maximum possible error due to inaccurate "eyeballing" of oscillation amplitudes. It is, therefore, believed, in view of the above discussion, that this "visual" error is the limiting factor for experimental accuracy, and, for this reason, a nominal error of ± 2.0 degrees is chosen as an estimate of amplitude measurement scatter.

Since frequency could be read directly off the oscilloscope, with no subsequent calibration required, error is limited to the accuracy and care with which this task was most often carried out. In a typical case, where the sine wave peaks were roughly three divisions apart (on the scope screen) and where each peak could easily be read to within a tenth of a division of its true position, the percent error is calculated to be 6.7 percent. It is felt that this value is probably a slight overestimation of the typical error and that an overall value estimate of approximately 5.0% is acceptable.

REFERENCES CITED

1. Bielawa, R. L., "Synthesized Unsteady Airfoil Data with Applications to Stall Flutter Calculations," Paper presented to the 31st Annual National Forum of The American Helicopter Society, May 1975.

2. Bisplinghoff, R. L., Ashley, H. and Halfman, R. L., Aeroelasticity, Addison-Wesley, 1955.

3. Carlson, R. G. et. al., "Dynamic Stall Modelling and Correlation with Experimental Data on Airfoils and Rotors," NASA SP-352, Rotorcraft Dynamics, Paper no.2, February 1974.

4. Carr, L. W., McAllister, K. W. and McCrosky, W. J., "Analysis of the Development of Dynamic Stall Based on Oscillating Airfoil Experiments," NASA TN D-8382, 1977.

5. Carta, F. O., Commerford, G. L., Carlson, R. G. and Blackwell, R. H., "Investigation of Airfoil Dynamic Stall and its Influence on Helicopter Loads," USAAMRDL TR-72-51, September 1972.

6. Carta, F. O. and Niebanck, C. F., "Prediction of Rotor Instability at High Forward Speeds," Volume III, "Stall Flutter," USAAVLABS, Fort Eustis, VA, TR 68-18C, February 1968.

7. Dowell, E. H., Curtiss, H. C., Jr., Scanlan, R. H. and Sisto, F., A Modern Course in Aeroelasticity, Sijthoff and Noordhoff, Alphen aan den Rijn, The Netherlands, 1978.

8. Dugundji, J., and Chopra, I., "Further Studies of Stall Flutter and Nonlinear Divergence of Two-Dimensional Wings," NASA CR-144924.

9. Ericsson, L. E. and Redding, J. P., "Quasi-Steady and Transient Dynamic Stall Characteristics," AGARD CP-204, Paper no.24, 1976.

10. Ericsson, L. E. and Redding, J. P., "Dynamic Stall Analysis in Light of Recent Numerical and Experimental Results," Journal of Aircraft, vol.13, no.4, April 1975, pp.248-255.

11. Ericsson, L. E. and Redding, J. P., "Dynamic Stall at High Frequency and Large Amplitude," Journal of Aircraft, vol.17, no.3, March 1980, pp.136-142.

12. Ericsson, L. E. and Redding, J. P., "Unsteady Airfoil Stall and Stall Flutter," NASA CR-111906, June 1971.

13. Gormont, R. E., "A Mathematical Model of Unsteady Aerodynamics and Radial Flow for Application to Helicopter Rotors," U.S ARMY AAMRDL TR-72-67, Eustis Directorate, 1973.

14. Halfman, R., Johnson, H. E. and Haley, S. M., "Evaluation of High Angle of Attack Aerodynamic Derivative Data and Stall Flutter Prediction Techniques," NACA TN-2533, 1951.

15. Ham, N. D., Young, M. I., "Torsional Oscillation of Helicopter Blades Due to Stall," Journal of Aircraft, vol.3, no.3, May-June 1966, pp.218-224.

16. Ham, N. D. and Garelick, M. S., "Dynamic Stall Considerations in Helicopter Rotors," Journal of the American Helicopter Society, vol.13, no.2, April 1968, pp.219-255.

17. Harris, F. D., Tarzanin, F. J., Jr. and Fisher, R. K., Jr., "Rotor High Speed Performance; Theory vs Test," Journal of The American Helicopter Society, vol.14, no.3, July 1970, pp.35-44.

18. Hornbeck, R. N., Numerical Methods, Quantum, New York, NY, 1975.

19. Johnson, W. and Ham, N. D., "On the Mechanism of Dynamic Stall," Journal of The American Helicopter Society, vol.17, no.4, October 1972, pp.36-45.

20. Johnson, W., "The Effect of Dynamic Stall on the Response and Airloading of Helicopter Rotor Blades," Journal of The American Helicopter Society, vol.14, no.2, April 1969, pp.68-79.

21. Kinney, R. B., "Two-Dimensional Viscous Flow Past an Airfoil in an Unsteady Airstream," AGARD CP-227, Paper no.26, 1977.

22. Liiva, J. and Davenport, F. J., "Dynamic Stall of Airfoil Sections for High Speed Rotors," Journal of The American Helicopter Society, vol.14, no.2, April 1969, pp.26-33.

23. Martin, J. M., Empey, R. W., McCrosky, W. J. and Cardonna, F. X., "An Experimental Analysis of Dynamic Stall on an Oscillating Airfoil," Journal of The American Helicopter Society, vol.19, no.1, January 1974, pp.26-32.

24. McAllister, K. W., Carr, L. W. and McCroskey, W. J., "Dynamic Stall Experiments on the NACA 0012 Airfoil," NASA TP-1100, 1978.

25. McCormack, R. W., "Status and Future Prospects of Using Numerical Methods to Study Complex Flows ast High Reynolds Numbers," AGARD LS-94, Paper no.13, February 1978.

26. McCormick, B. W., Jr., "Propeller Dynamics and Aeroelastic Effects," NASA CP-2126, 1979.

27. McCroskey, W. J., "Some Unsteady Separation Problems for Slender Bodies," AGARD LS-94, Paper no.8, February 1978.

28. McCroskey, W. J., "Prediction of Unsteady Separated Flows on Oscillating Airfoils," AGARD LS-94, Paper no.12, February 1978.

29. McCroskey, W. J., "Recent Developments in Dynamic Stall," Symposium on Unsteady Aerodynamics, Kinney, R. B., ed., Tuscon, University of Arizona, 1975, pp.1-33.

30. McCroskey, W. J., McAllister, K. W., Carr, L. W., Pucci, S. L., Lambert, O. and Indergand, R. F., "Dynamic Stall on Advanced Airfoil Sections," Presented at the 36th Annual Forum of The American Helicopter Society, May 1980.

31. Parker, A. G., Bucknell, J., "Some Measurements on Dynamic Stall," Journal of Aircraft, vol.11, no.7, July 1974, pp.371-374.

32. Pope, A., Harper, J. J., Low Speed Wind Tunnel Testing, John Wiley and Sons Inc., New York, NY, 1966.

33. Ryan, T. A., Jr., Joiner, B. L. and Ryan, B. F., MINITAB, STUDENT HANDBOOK, Duxbury Press, North Scituate, MA, 1976.

34. Schnittger, J. R., "Single Degree of Freedom Flutter of Compressor Blades in Separated Flow," Journal of the Aeronautical Sciences, vol.27, no.1, January 1954, pp.27-36.